Self-assembly of active particles

by

Phuoc Nguyen Nguyen Huu

A dissertation submitted in partial fulfillment
of the requirements for the degree of
Doctor of Philosophy
(Mechanical Engineering)
in The University of Michigan
2014

Doctoral Committee:

Professor Sharon C. Glotzer, Co-Chair
Professor Donald Siegel, Co-Chair
Professor Ronald Larson
Professor Michael J. Solomon

To my parents, whose endless love and hardwork in providing us with the best possible have always been and will be my biggest motivation.

Acknowledgments

It has been a long, challenging and, yet, rewarding journey. There are many valuable things that I have gained along the way, but one thing for sure is that I would not be able to go this far without the support, guidance and encouragement of many people. I am forever indebted to you but the least thing I can do is expressing my gratitude to my wonderful supporters here.

First of all, to my advisor, Prof. Sharon Glotzer, I thank you very much for your support and guidance. You have not only given me wonderful resources but also the intellectual freedom to pursue what I am truly interested in. Your patience even when things did not go as planned was important to my progress. During my Ph.D, I've learned a great deal from you that I believe will help me to be more successful in whatever I will pursue in the future.

To my committee members, Prof. Ronald Larson, Prof. Donald Siegel and Michael J. Solomon, I thank you for your valuable comments, suggestions and discussions. I would like to thank Prof. Larson, for interviewing and writing my letter of recommendation, as part of his service to the VEF fellowship in Vietnam, to apply for graduate school in the U.S.. It was quite a coincidence that I did not know that he was at Michigan until he became my committee member! I am also thankful to Prof. Siegel for a great deal of knowledge about atomistic simulation that I learned from his interesting class.

I would like to acknowledge the funding from Non-Equilibrium Energy Research Center (NERC), an Energy Frontier Research Center funded by the U.S. Department of Energy, Office of Science, Office of Basic Energy Sciences under Award Number DE-SC0000989. I also thank the Vietnam Education Fellowship for their support during my PhD program.

I have been fortunate to be a member of an amazingly diverse and talented Glotzer group. I would like to especially thank Eric Jankowski, Michael Engel and Daphne Klotsa for being my mentors, who have guided and helped me tremendously. Big thanks to Eric for walking me through the rough beginning and Michael and Daphne for helping me to conquer the finishing line of the PhD race. I am also grateful to Trung Nguyen for introducing me to the group, being a great friend and the constant support. I thank the group members for many interesting interactions, both on self-assembly and soccer, and for their friendship, especially with Trung Nguyen, Eric Jankowski, Pablo Damasceno, Antonio Osorio, Richmond Newman, Daniel Ortiz, Carolyn Phillips, Greg van Anders, Ryan Marson, Ben Schultz, Eric Irgang, Andres Millan, Sam Nola, Wenbo Shen and Matthew Spellings. I also thank the group manager, Karen Coulter, for her excellent service to the group that enables us to solely focus on doing science.

I am also thankful to Prof. Galip Ulsoy and Prof. Dawn Tilbury from the Mechanical Engineering department for a brief but beneficial period of working under them. From them, I learned some valuable lessons of how to conduct research systematically and effectively. I thank Susan Hamlin from Chemical Engineering department for always being helpful with my paper work. I thank Dr. Rick Riolo and the people of the Complex System Advanced Academic Workshop and the Center for Study of Complex Systems at Michigan for the fun and interesting time that we had together.

I would like to thank my friends, who have shared with me so many memory in Ann Arbor in last 6 years and have made Ann Arbor my “second home”. I thank my extended Vietnamese “family” Trung Nguyen, Chieu Vu, Trinh Tran, Hai Dinh, Hai Nguyen, Loc Khieu, Xuan Tran, Lam Huynh, Hoa Trinh, Thanh Do, Thai Dam, Can Le, Ban Dong, Duc Le, Cam Duong, and Nghia Vo. I am also thankful to my (former) housemates at the scientific co-op Gamma Alpha, especially Tara Clancy, Leon Webster, Ya Yang, Chuan Li, Jen Peacock , Katherine Crocker, Jared Kabara , Alexi Ernstoff, Emily Lauderdale, Julia Cohen, and Lorraine Suzuki for our time together.

Finally, to my parents, brothers and my loved ones, my deepest gratitude. Your unconditional love, support and encouragement have been and will be my biggest source of motivation.

Thank you very much!

Table of Contents

Dedication ii

Acknowledgments iii

List of Figures ix

List of Appendices xix

Abstract xx

Chapter 1 Introduction 1
1.1 Motivation 1
1.2 Thesis overview 3

Chapter 2 Background 6
2.1 Self-assembly 6
2.1.1 Definition and importance 6
2.1.2 Self-assembly approaches 9
2.2 Active matter 14
2.2.1 Introduction 14
2.2.2 Summary of the literature 16

Chapter 3 Simulation Models and Methods 24
3.1 Overview 24
3.2 Coarse-grained pair potentials 26
3.2.1 Lennard-Jones potential 26
3.2.2 Weeks-Chandler-Andersen potential 27
3.2.3 Morse potential 28
3.3 Molecular Dynamics methods 28
3.3.1 Overview 28
3.3.2 Modified Langevin Dynamics for active particles 29
3.3.3 Modified Brownian Dynamics for active particles 33
3.4 Software packages 35
3.4.1 HOOMD Blue 35

3.4.2 Other software . . . 37

Chapter 4 Self-assembly of Self-Propelled Particles . . . 40
4.1 Introduction . . . 40
4.2 Model and method . . . 42
4.2.1 Model . . . 42
4.2.2 Method . . . 44
4.3 Results and discussion . . . 46
4.3.1 3D swarms . . . 46
4.3.2 Initial conditions . . . 51
4.3.3 Noise . . . 57
4.4 Driving forces . . . 59
4.5 Conclusions . . . 62

Chapter 5 Self-assembly of Self-Rotated Particles . . . 64
5.1 Introduction . . . 64
5.2 Model and methods . . . 66
5.3 Non-equilibrium phase behavior of spinners . . . 67
5.3.1 Uneven distribution of energy . . . 67
5.3.2 Frozen state . . . 69
5.3.3 Mixed and phase-separated fluids . . . 69
5.3.4 Rotating crystals . . . 70
5.4 Effective interaction between spinners. . . . 72
5.4.1 Spinodal decomposition . . . 72
5.4.2 Density-dependent motility . . . 74
5.4.3 Effective Demixing Potential . . . 75
5.5 Collective dynamics at interfaces and transport . . . 77
5.5.1 Heterogeneous dynamics . . . 77
5.5.2 Interfacial transport . . . 77
5.6 Discussion . . . 80

Chapter 6 Self-Rotated Particles in Confinement . . . 82
6.1 Introduction . . . 82
6.2 Model and method . . . 84
6.3 Systems of fixed boundaries . . . 85
6.3.1 Experimental results . . . 85
6.3.2 Simulational results . . . 86
6.4 Systems of flexible boundaries . . . 90
6.4.1 Non-driven boundaries . . . 91
6.4.2 Driven boundaries . . . 91
6.5 Discussion . . . 96

Chapter 7 Conclusions and Outlook . . . 99
7.1 Conclusions . . . 99
7.2 Outlook . . . 100

7.2.1 Self-assembly of driven shapes 100
7.2.2 Confined systems of active particles 101
7.2.3 Active modifiers 101
7.2.4 3D systems 102

Appendices 103

Bibliography 152

List of Figures

Figure

2.1 Anisotropic building blocks for self-assembly [1] 8

2.2 Self-assembly of shaped particles. (a) cubic colloids self-assemble into cubic crystals [2]. (b) Rhombic dodecahedra self-assemle into triangular and hexagonal platelike morphologies [3]. (c) Corner-truncated octahedra form Octahedral supercrystals. (d) Self-assembly of lock and key colloids under depletion interaction [4]. (e) Self-assembly of octapod (inset) nano particles into super lattice crystals [5]. 10

2.3 Self-assembly of from building blocks with directional interactions. (a) Building blocks with attached tethers [6]. (b) Building blocks with interaction patches [7]. (c) Hexagonally packed columnar phase formed by 120 tethered nanodisks from two views. The disks are similar to particle b in (a) but with six tethers attached to it [6]. (d) Rings formed via self-assembly of patchy sphere h in (b) (left) and patchy particle i in (b) (right) [7]. (e) Self-assembly of polymer-tethered gold nanorods into different structures in selective solvents: a- rings, b-chains, c-bundles of nanorods, d-nanospheres, e-bundles of nano chains [8]. 12

2.4 Examples of (active) biological self-assembly. (a) Vortex of fishes [9]. (b) ant circle of death: Army ants blindly follow circular trails of pheromone excreted by them until they die of exhaustion [10].(c) a swarm of bacteria [11].(d) Microtubule filaments driven by kinesin complexes, or simply motor proteins, transform from randomly oriented to vortices and eventually asters as the density of kinesin increases from left to right [12]. 15

2.5 Models of self-propelled particles. (a) Particles moving in the same direction in the Vicsek model [13]. (b) Self-propelled rods interacting via excuded volume cluster into nematic ordering [14]. (c) Self-propelled hardcore particles phase-separate into dense and gas phases [15] 17

2.6 Experimental examples of active matter: (a) Microtubules in a mixture with kinesin self-assemble into steady-state vortices and asters as the concentration of kinesin increases (from left to right) [12]. (b) Self-propelled colloids form "living" crystals that self-assemble and break dynamically [16]. (c) Vibrated rods exhibit nematic phase with "giant" number fluctuation, with noticeable dilute and dense regions that move on the surface [17]. (d) Millimeter magnetic disks that are driven by rotating external magnetic self-assemble into different patterns on a fluid surface as the rotation changes [18]. (e) Magnetic Janus particles that are driven by a precessing magnetic field synchronize their motion and self-assemble into different configurations [19]. 21

3.1 MSD over time for a system of 16384 gears simulated by the LD code at temperature of 5. Each gear has a mass of 5 and a translational drag coefficient of 100. The theoretical translational diffusion coefficient is, according to equation 3.14, 0.01. The value is exactly equal to $\frac{1}{4}$ of the slope of the MSD versus time, thus satisfying the fluctuation-dissipation theorem. . . . 32

3.2 MSD over time for a system of 10000 gears simulated by the BD code with translational diffusion coefficient of 0.01.The value is exactly equal to $\frac{1}{4}$ of the slope of the MSD versus time, thus satisfying the fluctuation-dissipation theorem. 36

3.3 Performance measured in time steps per second of HOOMD Blue compared with LAMMPS. The benchmark simulation is one thousand tethered nanorods (14000 total particles) and is performed 50 times for each benchmark [20]. 37

4.1 Three-dimensional self-propelled swarms of $N = 600$ Morse particles at $T^* = 0$, $\alpha = 2$, $\gamma = 1$, and $\beta = 0.5$. Steady state swarms are observed in MD simulations after 2×10^6 time steps have evolved for particles within a 20σ simulation box with periodic boundary conditions. Particles are initialized with random velocities and are randomly distributed within a 5σ cubic region inside the simulation box. Blue arrows indicate particle velocities. Orange spheres represent particle positions, but the sphere diameters to not correspond to particle size. Scale bars are shown in the upper right and alignment order A is shown in the lower left of each swarm. Swarm radii range from 0.06σ to 0.3σ (ball). (a) Ball ($C = 1.5$, $l = 0.5$) composed of concentric spherical layers of particles and identical velocities. (b) Stationary hollow shell ($C = 0.5$, $l = 0.5$) composed of particles that travel in circular orbits. (c) Stationary ring ($C = 0.5$, $l = 0.5$) with all particles traveling in the same circular orbit. (d) Stationary spherical swarm ($C = 0.6$, $l = 0.5$) with clumps of particles that travel in circular orbits. (e) Stationary cylindrical swarm ($C = 0.6$, $l = 0.5$) composed of clumps of particles traveling about the same circular orbit. The particles within the clumps move in a cylindrical fashion, but follow a complex path such that the cross-sectional shape of the cylinder appears to be time dependent. (f) Torus ($C = 0.6$, $l = 0.3$) composed of particles that travel in circular orbits of different radii, but share an axis of rotation. Particle paths within the torus span the entire volume: a particle that is near the hole eventually moves to the outer part and back again. See Supplemental Material videos 1-6 for movies of these swarms. 47

4.2 "Phase diagram" for 3D stable structures assembled at values of $0.1 \leq l \leq 2.0$ and $0.1 \leq C \leq 2.0$, $T^* = 0$, $\alpha = 2$, $\gamma = 1$, and $\beta = 0.5$. The ratio of repulsion to attraction strength $C = \frac{C_r}{C_a}$ and the ratio of repulsion to attraction length scales $l = \frac{l_r}{l_a}$ determine the shape of the interaction potential and the swarms observed at steady state. In the upper right quadrant ($l > 1$, $C > 1$) repulsion dominates the potential, preventing organized clusters from assembling. In the lower right quadrant ($l < 1$, $C > 1$) the repulsion is short-ranged and the attraction is long-ranged, resulting in translating spherical balls. In the lower left quadrant ($l < 1$, $C < 1$) attraction dominates the potential and the phase diagram is most complex, with shells, rings, tori, balls, and clumps all stabilized within narrow ranges of l and C. In the top left quadrant ($l > 1$, $C < 1$) particles are attractive, but the repulsive length scale dominates, giving rise to hollow shells.From Ref. [21]. 49

4.3 Four initial conditions and their probabilities of transitioning to a ring. The shell and cylinder initial conditions have radii of 0.062. The ball has a radius of 1.35 and the random configuration is distributed randomly in cubic box with side length of 5. Ring transition probabilities are calculated from 100 independent runs performed for each of the indicated initial condition with $T^* = 0$, $\alpha = 1$, $\gamma = 1$, $\beta = 0.5$, $C_r = 0.5$, $l_r = 0.5$, $C_a = 1$, $l_a = 1$, and $N = 600$ with random initial velocities.From Ref. [21]. 53

4.4 Probability of a random shell transforming into a ring as a function of alignment order A (Eq. 4.7) at $T^* = 0$, $\alpha = 1$, $\gamma = 1$, $\beta = 0.5$, $C_r = 0.5$, $l_r = 0.5$, $C_a = 1$, $l_a = 1$, and $N = 600$. The blue line is drawn as a guide to the eye. Inset are representative alignment order trajectories for swarms that form a shell (red) and ring (blue).From Ref. [21]. 54
4.5 Initial time evolution of the alignment order A averaged over 10 independent runs for six different combinations of initial arrangements and initial velocities. The particles are spatially initialized either randomly within a 5σ cube, within a 2.7σ ball, or on a 0.062σ shell within a 20σ cubic simulation box with periodic boundary conditions. Velocities are initialized from a Gaussian distribution with mean 2 and standard deviation 1 (random $\vec{v}$) or drawn from the ring velocity distribution with mean 2, standard deviation 0.15, and z-component = 0 (parallel $\vec{v}$). The number of observed rings after 1×10^6 time steps are shown in parentheses. Error bars are plotted every 2000 steps and denote one standard deviation. 56
4.6 Probability of shell (red) and ring (blue) formation as a function of T^* at $\alpha = 2$, $\gamma = 1$, $\beta = 0.5$, $C_r = 0.5$, $l_r = 0.5$, $C_a = 1$, $l_a = 1$, and $N = 600$. 100 independent runs are performed at each noise level, with particles initially randomized in a 5σ cube within a 20σ cubic simulation box and are evolved for 1×10^6 time steps. Error bars denote one standard deviation.From Ref. [21]. 58
4.7 Normalized cylinder height Λ as a function of dimensionless temperature T^* and number of particles N. Particles are initialized as a ring with random velocities. $\alpha = 2$, $\gamma = 1$, $\beta = 0.5$, $C_r = 0.5$, $l_r = 0.5$, $C_a = 1$, and $l_a = 1$. Λ are averaged over 10 simulation snapshots and over 10 independent simulation runs, where the snapshots are the last 10 at 1×10^4time step increments. The standard deviations of Λ are less than 3% of the mean values and are not shown.From Ref. [21]. 59
4.8 Mechanisms of structural transitions among shells, rings, and cylinders. Increasing the temperature of a ring causes it to transition into a cylinder of increasing height. At large enough T^*, cylinders transition into hollow shells. The transformation of a hollow shell into a cylinder or ring requires not only that the temperature be decreased below $T^* = 0.007$, but also that an instantaneous fluctuation in alignment order is sufficiently large to initiate the transition. The transition involves the shell polarizing into cylindrical bands, which align eventually turning into a cylinder with noise-dependent height or a ring if the noise is zero.From Ref. [21]. 60

5.1 (a) Clockwise ('A') and counterclockwise ('B') spinners. (b) The ratio of translational to total kinetic energy κ indicates the presence of a phase transition ($\omega_0 = 1$). Error bars are smaller than the symbols. The inset shows the critical density ϕ_c as a function of noise T^*. (c) Non-equilibrium phase diagram based on simulation data [22] at $T^* = 0$. Lines indicate phase boundaries. Insets show representative snapshots as the system approaches steady state. A and B spinners in the fluid (crystal) phase are shown in dark (light) blue and orange (red) colors. 50:50 mixtures are used in (b,c). From Ref. [23]. 65
5.2 The ratio of translational to total kinetic energy κ indicates the presence of a phase transition ($\omega_0 = 1$). Error bars are smaller than the symbols. The inset shows the critical density ϕ_c as a function of noise T^*. The system consists of 16384 spinners driven by 50:50 ratio. From Ref. [23]. 68
5.3 Fractions of rotating crystal domains co-existing with fluid. The crystal (fluid) are colored red (orange) for B spinners and light (dark) blue for A spinners. The crystal spinners arrange in square lattices. From Ref. [23]. . 70
5.4 Crystal fraction $\chi(t)$ for a system of 16384 A spinners at density $\phi = 0.6$ for three levels of activity. χ achieves a steady state value, demonstrating the coexistence of fluid and rotating crystals. The data points are averaged over 10 runs. From Ref. [23]. 71
5.5 Domain size growth for a 50:50 mixture of 16384 spinners at $\phi = 0.5$ and $\omega_0 = 1$ during phase separation ($\phi = 0.5$). Each data point is averaged over 10 runs and has a standard deviation smaller than the markers. From Ref. [23]. 73
5.6 Comparison of (a) translational diffusion coefcient D and (b) mean-squared displacements for an (B) intruder in a matrix of 100 opposite (A) spinners. The spinners are driven by $\omega_0 = 1$. Curves in (b) at different densities are offset for clarity. Each data point in (a) is averaged over 10 runs. From Ref. [23]. 74
5.7 Effective demixing potential obtained for $N_A = 100$ and $N_B = 2$ at $\omega_0 = 1$ and different densities. The data is sampled every 100 time steps over 100 million time steps after the system reaches a steady state. From Ref. [23]. . 75
5.8 Typical interaction of two opposite spinners (a) and two like spinners (b). Like spinners tend to "stick" longer during a collision than opposite spinners, leading to an effective attraction between them. 76
5.9 (a)-(d) Vector plots show the short-time diffusion $\Delta\vec{x}(t)$ in systems of $N = 576$ spinners with different numbers of intruders: (a) one, (b) 2%, (c) 10% and (d) 50%. The snapshots (a)-(c) are zoomed in. We use $\omega_0 = 1$ and densities of 0.5. The observation time windows are $10t_0$. 78
5.10 Vector plots show the short-time diffusion $\Delta\vec{x}(t)$ in systems of $N = 16384$ spinners at density of 0.6 where crystallization occurs. The system is driven by $\omega_0 = 1$ and 50:50 ratio. The observation time windows is $t = 100t_0$. . . 79

5.11 A system of 566 active spinners and 10 inactive spinners at density of 0.5. (a) Trajectories of inactive particles (green) at density of 0.5 and (b) their probability density close to an interface for different densities. The light blue spinners are driven by $\omega_0 = 1$. 80

6.1 (a) An initial condition of 16 spinners of 50:50 mixture driven by $\omega_0 = 1$, in a rigid circular boundary at area density $\phi = 0.43$. (b) and of 142 interior spinners of 50:50 mixture driven by $\omega_0 = 1$, in a flexible boundary at $\phi = 0.5$. The boundary 36 spinners are connected by FENE springs (green) and are driven clockwise (blue). One spinner is colored red to track to motion of the boundary. 83

6.2 The experimental parameters of the spinners (Figure excerpted from a Bishop group's report). 84

6.3 (a)Images of spinner system ($\phi = 0.43$) at regular intervals of 10 min. (b) Association coefficient $c(t)$ for the same system; the solid red line is a 120 s moving average and the dashed red line is the mean. Back points are from randomized disc assigments; as expected the mean of these data (dashed black line) is nearly 1. The insets show (from left to right) minimum association ($c = 1.1$), random association ($c = 1$) and maximum association ($c = 0.6$) (Figure excerpted from a Bishop group's report). 86

6.4 a) Simulation of 16 spinners at area density $\phi = 0.43$ and $\omega_0 t_r = 109$, which corresponds to the experimental system in Fig. 6.3. The plot shows the instantaneous association coefficient c every 1000 time units. The system tends toward demixing as it evolves from a minimally associated state ($c = 1.1$) to a strongly associated state ($c = 0.79$). We also observe random remixing and demixing in the system as indicated by large fluctuations in c as expected for a small, finite system. b) The average association coefficient and its standard deviation calculated over 100 runs of different random initial conditions. Other parameters are the same as in a). The system exhibits large fluctuations as one would expect from this small system size. 87

6.5 Simulation of 100 spinners at $\phi = 0.43$ and $\omega_0 t_r = 109$. The system exhibits a clear trend towards phase-separation. 88

6.6 Simulation of 1000 spinners at $\phi = 0.5$ and $\omega_0 t_r = 109$. The system is initialized in a disordered state but exhibits phase-separation (left) and the formation of rotating crystals over time (right). 89

6.7 Time evolution of 142 spinners from 0 to $10000 t_0$ or 20 minutes with a non-driven boundary initialized as in Fig. 6.1(b). The interior spinners are driven oppositely with CW:CCW ratio of 50:50 and by $\omega_0 = 1$. The interior spinners tend to demix into domains of like particles that seem to influence the system shape. The boundary rotates randomly (as opposed to exhibiting net rotation) 90

6.8 A snapshot of the system after 10000 time units. The boundary spinners are driven clockwise and the interior spinners driven with a 50:50 ratio of oppositely rotating spinners. For both types of spinner, $\omega_0 = 1$. The system phase separates into a core of (yellow) particles rotating counter-clockwise surrounded by spinners rotating oppositely. At the interface, the interior particles collectively translate in a counter-clockwise circular motion. The boundary rotates clockwise. The red arrows show translational motion directions. 92
6.9 A schematic drawing of how a net boundary rotation arises from boundary spinners pushing against the interior particles. The reaction forces on the CW boundary spinners resulting from particle contacts dominantly point in the directions that cause the entire boundary to rotate CW. 93
6.10 A snapshot of the system after 5000 t_0. The boundary and interior spinners each contain a 50:50 ratio of active spinners driven in opposite directions. The interior spinners separate into a dynamical Janus-like particle. Each domain of like particles are in contact with the oppositely-drive boundary. Translational motion of the interior spinners is shown by the red arrows. The spinners form two oppositely vortices, while the boundary does not exhibit any net rotation. The system does not always maintain a perfect Janus-like shape as a few spinners occasionally diffuse into the opposite domain at the boundary and translate along the it. 94
6.11 The interior spinners are driven oppositely by CW:CCW ratio of 67:33 while boundary spinners are driven oppositely by CW:CCW ratio of 33:67. (a) A snapshot of the system after 10000 time units. The interior spinners separate into a dynamic, imbalanced Janus-like particle. Each domain of like particles is in contact with the oppositely-driven boundary. The spinners' translational motion is illustrated by the red arrows. (b) Yellow spinners occasionally diffuse into the blue domain and translate along the boundary. 95
6.12 A snapshot of the system after 10000 time units. The boundary and interior spinners are driven by 67:37 ratio. Instead of phase-separating into a Janus-like particle as one might expect, the interior spinners phase-separate into a moving core surrounded by oppositely particles that form complex vortices. The core seems to keep the same position relative to its boundary while the boundary is rotating clockwise. The spinners' translational motion is illustrated by the red arrows. 96
6.13 Summary of all studied cases with flexible boundaries. A driving torque of $\omega_0 = 1$ was used for all cases. 97

B.1 *Snapshots from Movie 1.* A binary system of $N = 576$ spinners, where half of the spinners rotate clockwise and the other half rotate counter-clockwise. Simulation parameters: $\phi = 0.5$, $\omega_0 = 1$, $T^* = 0$. The movie shows spinners (left column) and vector plots of the short-time diffusion $\Delta x(10t_0)$ (right column) at three different times during spinodal decomposition. The simulation starts from an initially mixed configuration (top row, $t = 0$) and proceeds through phase separation (middle row, $t = 1,000t_0$), until in steady state two vertical stripes are formed (bottom row, $t = 5,000t_0$). From Ref. [23]. . . . 143

B.2 *Snapshots from Movie 2.* A binary system of $N = 16,384$ spinners, where half of the spinners rotate clockwise and the other half rotate counter-clockwise. Simulation parameters: $\phi = 0.5$, $\omega_0 = 1$, $T^* = 0$. The movie shows spinners (left column) and vector plots of the short-time diffusion $\Delta x(100t_0)$ (right column) at three different times during spinodal decomposition. The simulation starts from an initially mixed configuration (top row, $t = 0$) and proceeds through phase separation (middle row, $t = 1,000t_0$). At the end of the simulation, steady state is not yet reached (bottom row, $t = 10,000t_0$). From Ref. [23]. 144

B.3 *Snapshots from Movie 3.* A binary system of $N = 16,384$ spinners, where half of the spinners rotate clockwise and the other half rotate counter-clockwise. Simulation parameters: $\phi = 0.6$, $\omega_0 = 1$, $T^* = 0$. The movie shows spinners (left column) and vector plots of the short-time diffusion $\Delta x(100t_0)$ (right column) at three different times during simultaneous spinodal decomposition and the formation of rotating crystal within single component domains. The simulation starts from an initially mixed configuration (top row, $t = 0$) and proceeds through phase separation (middle row, $t = 1,000t_0$). At the end of the simulation, steady state is not yet reached (bottom row, $t = 10,000t_0$). From Ref. [23]. 145

B.4 *Snapshots from Movie 4.* Ten inactive particles (dark green) immersed into phase separated system of an even mixture of $N = 566$ spinners (light blue and orange). Simulation parameters: $\phi = 0.5$, $\omega_0 = 1$, $T^* = 0$. The inactive particles are observed moving along the interface. Snapshots are shown through time: $t = 0$ (left), $t = 3,000t_0$ (middle), $t = 6,000t_0$ (right). From Ref. [23]. 146

B.5 *Snapshots from Movie 5.* Comparison of Langevin Dynamics (left side) and Brownian Dynamics (right side) in simulations with fine time resolution ($0.1t_0$ between two consecutive snapshots in the videos). Particles' positions fluctuate more in the Brownian Dynamics simulation (because of noise and the absence of inertia), but otherwise the systems behave very similarly with both simulation techniques. A binary system of $N = 576$ spinners, where half of the spinners rotate clockwise and the other half rotate counter-clockwise. Simulation parameters: $\phi = 0.5$, $\omega_0 = 1$, $T^* = 0$. The simulation starts from an initially mixed configuration (top row, $t = 0$) and slowly proceeds towards phase separation (middle row, $t = 50t_0$ and bottom row, $t = 100t_0$). From Ref. [23]. 147

B.6 Phase diagram in the ϕ-ω_0 plane at (or near) steady state for systems of $N = 16,384$ spinners, where half rotate clockwise and half rotate counterclockwise. Four phases are identified: frozen state, mixed fluid, phase separated fluid and rotating crystal phase. Each data point corresponds to one independent simulation, where we identified the prevailing steady state in the final simulation frame. Lines are drawn to separate regions where the same steady state is observed. Rotating crystals typically coexist with phase-separated fluid. The transition from mixed fluid to phase-separated fluid is smeared out, all the other transitions are sharp. From Ref. [23]. . . 148

B.7 Radial distribution function $g(r) \equiv \rho(r)/\rho(L/2)$ at three densities for the following systems (L is the edge length of the square simulation box): (a) $N = 100$ inactive (non-driven) particles, $\omega_0 = 0$, $T^* = 5$; (b-d) a mixture of $N_A = 98$ clockwise spinners (matrix) and $N_B = 2$ counter-clockwise spinners (intruders), $\omega_0 = 1$, $T^* = 0$. We compare correlations for matrix-matrix pairs (b), intruder-matrix pairs (c), and the intruder-intruder pair (d). Each intruder strongly prefers the vicinity of the other. Note that compared to the inactive pairs, the position of the first well of $g(r)$ the active particles shifts to higher r values at low densities. This shift happens because there is still enough space at these densities for the active gears to move apart from each other to minimize collisions. From Ref. [23]. 149

B.8 Heat maps showing the kinetic energy for an even mixture of $16,384$ spinners at $\omega_0 = 1$, $T^* = 0$ and $\phi = 0.5$ (a,b) or $\phi = 0.6$ (c,d). Red and blue colors represent A and B spinners, respectively, with intensities based on the translational (E_{tr}, (a,c)) and rotational (E_{rot}, (b,d)) kinetic particle energy. Choosing the intensities linearly does not work well, because the distribution of energies (E_{rot} or E_{tr}) has a long tail. Instead, we choose intensities by first calculating the cumulative probability distribution of the energy by sorting the energy into bins. As a result, particles with the lowest (highest) kinetic energies are assigned the darkest (brightest) colors. We observe in all cases that the kinetic energy is uniform throughout each phase of the fluid, which means the interface has no significant effect. This demonstrates that the super-diffusive behavior along the interface is not the consequence of an enhanced translational and rotational velocity, but rather caused by collective directed motion. In (c,d), crystals are visible by darker colors, because particles move slower once crystallized. From Ref. [23]. 150

B.9 (a) Radial distribution function $g(r)$ for an even mixture of $16,384$ spinners at $\phi = 0.5$, $\omega_0 = 1$, $T^* = 0$, taken at three different times while the system is phase separating. We analyze the domain size growth over time (Fig. 2a) by following the first zero in $g(r)$. (b) Crystal fraction $\chi(t)$ (ratio between the number of spinners in crystals and the total number of spinners) for the same system at higher density $\phi = 0.6$ for three levels of activity. χ achieves a steady state value, demonstrating the coexistence of fluid and rotating crystals. From Ref. [23]. 151

B.10 The Lifshitz-Slyozov (LS) theorem predicts that in two dimensions the growth exponent of the peak of the structure factor S_{peak} is twice the exponent of growth of the domain size R in real space (see Ref. [35] of the main text). We find the LS theorem holds for our system of actively rotated spinners. (a) The growth exponent for the domain size is consistent with $1/3$. (b) The growth exponent for the peak height of the structure factor is consistent with $2/3$. Simulations are conducted with 16,384 particles at density $\phi = 0.5$. The spinners are driven with $\omega_0 = 1$ at $T^* = 0$. Note that (a) is identical to Fig. 2(a) in the main text. From Ref. [23]. 151

List of Appendices

Appendix

A Supplementary materials for Chapter 4 104
A.1 Codes 104
A.2 Videos 106

B Supplementary materials for Chapter 5 107
B.1 Codes 107
B.2 Movies and Figures 138
B.3 Non-equilibrium phase boundaries 138
B.4 Effective demixing potential 139

Abstract

Self-assembly of active particles is believed to play an important role in enabling tomorrow's generation of smart materials. As a system is driven out of thermodynamic equilibrium, existing thermodynamic theory fails to predict the system behavior; however, it often exhibits rich and novel behaviors that are not found otherwise and could be leveraged for designing smart materials. In this thesis, by using computer simulation, we investigate the self-assembly behaviors of active particles driven via two different mechanisms: self-propulsion and -rotation, and show that the particle activity, in combination with other design parameters, gives rise to a great diversity of novel structures and dynamics.

In particular, we implement the first 3D model of self-propelled particles interacting via a soft Morse potential and demonstrate how the self-propulsion together with the parameters of interaction potential and thermal noise influence the particles to form a variety of 3D swarming structures. We also report novel behaviors that deviate from equilibrium self-assembly, including swarm coexistence, sensitivity to initial conditions and structure switching. The results, in addition to elucidate general swarming behavior, could motivate further studies in self-assembly of self-propelled, interacting colloids in 3D.

We then perform the first study of self-rotated shaped particles that interacting solely via excluded volume. Each particle is driven by a constant torque in either a clockwise or counter-clockwise direction. In spite of the model simplicity, we observe a wealth of interesting behavior that is otherwise not possible with self-propelled particles or in equilibrium self-assembly. We report phase separation, collective and heterogeneous dynamics, rotating crystals and complex phase behavior. The rich behavior resulted from a minimal model

opens up many possibilities for further studies of practical interest.

Lastly, we carry out preliminary, exploratory study of systems of self-rotated particles in confinement. Early experimental results from experimental collaborators confirm some of the findings for bulk systems. In addition, our initial simulations reveal some remarkable, unique dynamics for systems with flexible boundaries and highlights exciting possibilities worth pursuing further.

Chapter 1
Introduction

1.1 Motivation

One day, hopefully not far in the future, your shirts will turn water-resistant under rains, your house paint color could be changed instantly according to the weather (or your!) mood and your tennis rackets could be conveniently compressed to fit to your palm. All of these are examples of tomorrow's generation of smart materials that will fundamentally transform human quality of lives but are, unfortunately, still mostly imaginative. Most of current materials are static, which means once they are formed, their properties remain unchanged during their entire lifecycle. Some primitive smart materials include shape-memory alloys that can reversibly deform themselves under temperature or stress changes and piezoelectric materials that can bend, expand or contract under an applied voltage. But the materials are still far from what we aspire to. However, the quest for designing and realizing such futuristic materials has begun and self-assembly is believed to play an important role in achieving the goal.

Self-assembly is a process where individual, discrete building blocks spontaneously form an ordered arrangement without human intervention. It naturally happens everywhere and is responsible for countless phenomena from formations of galaxy to living cells. In recent years, self-assembly has gained significant attention in the materials science and related communities as a promising bottom-up route for creating materials at the mesoscale. Particles in nano- to micro-meter sizes are imparted with the right attributes that enable

them to self-assemble in a proper environment, e.g. water, into desired structures. Designing building blocks with the right attributes has been an important research endeavor that encompasses anything from sizes, shapes to interactions. Recently, learning design lessons from biological systems has gained significant importance in implanting smart properties to materials. After all, Nature is abundant of adaptive, smart biological systems, including formation of virus capsids, bacteria swarming and bird flocks; and amazingly many of the system-level behaviors come from some simple rules among constituent individuals. For an example, researchers have shown that [24] the beautiful and constant-changing bird flocks that one has seen can be reproduced by computer simulations of self-propelled particles (particles that move by themselves at a constant velocity) interacting via only three simple rules: 1, a particles comes to its neighbors if it is too far away, but 2, does not come too close to a neighbor to avoid potential collisions, and 3, move at the neighbors' speed if it is at a right distance. Examples like this lead to important questions: What can we learn from the natural systems, and how are we going to implement them to realize the desired smart materials?

One inherent property of the aforementioned biological systems, if not of all biological systems, is that they all operate far from equilibrium: There is a constant energy exchange between the systems and their environment, and stopping this energy exchange will cause the system to disintegrate. This energy exchange often enables motion of individual units (e.g. swimming or flying) and is the key to the emergence of interesting collective behavior that leads to novel properties such as self-adaptability and self-reconfigurability. Because of this, self-assembly of far-from-equilibrium systems has recently become a growing and important research direction in understanding the principles behind enabling new generations of smart materials. Recent experimental advancement in not only synthesis of building blocks of various shapes and sizes but also in imparting particles active properties such as the ability to self-propel could not come at better time. The new experimental capabilities allow one to start asking more comprehensive questions of 1) how a system of active building blocks

with these various attributes behaves and 2) what one can learn from there to potentially apply to designing smart materials.

In this thesis, we investigate far-from-equilibirum self-assembly behavior of particles driven by two different mechanisms: self-propulsion and self-rotation. Self-propulsion is a popular moving mechanism in biological systems and has been shown to give rise to interesting collective behavior in 2D systems of interacting point particles. However, equivalent 3D systems, prior to this thesis, had not been comprehensively investigated. Parts of this thesis study in detail how parameters such as interaction potentials, thermal noise and self-propelled speed influence the behavior of 3D systems. In addition to further elucidate general swarming behavior, which has a wide range of applications on its own, the results could motivate future studies for systems of interacting, self-propelled colloids. While self-propulsion as a method of inputing energy to a system has been given major attention, self-rotation has not been systematically studied. However, driving a system through self-rotation is interesting because 1) it does not directly alter translational motion and 2) has a circular symmetry in 2D that potentially allow adoption of more complex local structures. Parts of this thesis investigate how self-rotation influences the behavior of systems of shaped hard particles. In particular, how the energy inputed to the rotational degree of freedom re-distributes and how that affects the dynamics and structures of the system. The results could potentially provide us an alternative mechanism for driving and designing, in the right combination with other design parameters, novel active systems.

1.2 Thesis overview

The thesis is organized as follows. Chapter 1 discusses about the motivation for the work and organization of the thesis. Chapter 2 summarizes the relevant background work for self-assembly and active matter. In Chapter 3, the simulation models and methods and software packages utilized in this thesis are discussed in detail.

In Chapter 4, we investigate the swarming behavior of self-propelled particles. We find a variety of swarms of different overall shape assemble spontaneously and that for certain Morse potential parameters at most two competing structures are observed. We report a rich "phase diagram" of athermal swarm structures observed across a broad range of interaction parameters. Unlike the structures formed in equilibrium self-assembly, we find that the probability of forming a self-propelled swarm can be biased by the choice of initial conditions. We investigate how thermal noise influences swarm formation and demonstrate ways it can be exploited to reconfigure one swarm into another. Our findings validate and extend previous observations of self-propelled Morse swarms and highlight open questions for predictive theories of far-from-equilibirum self-assembly. The results presented in this chapter are published in Ref [21].

In Chapter 5, we study collective phenomena with rotationally driven spinners of concave shape. Each spinner experiences a constant internal torque in either a clockwise or counterclockwise direction. Although the spinners are modeled as hard, otherwise non-interacting rigid bodies, their active motion induces an effective interaction that favors rotation in the same direction.With increasing density and activity, phase separation occurs via spinodal decomposition, as well as self-organization into rotating crystals. We observe the emergence of cooperative, super-diffusive motion along interfaces, which can transport inactive test particles. Our results demonstrate novel phase behavior of actively rotated particles that is not possible with linear propulsion or in non-driven, equilibrium systems of identical hard particles. The results presented in this chapter are being published in Ref [23].

Chapter 6 presents and discusses about our preliminary results of systems of active spinners confined in a boundary. The research have been done in collaboration with the group of Prof. Kyle Bishop at Pennsylvania State University and is divided into two parts: systems with fixed and flexible boundaries. We confirm experimentally the demixing reported in Chapter 5 for small systems with fixed boundaries and report new, richer phenomena for systems with flexible boundaries. In particular, we find that by driving the boundary we can

influence both the interior dynamics and morphology. Chapter 7 summarizes the results and the contributions, and discusses the outlook of the thesis. Appendix A includes/decribes the codes used in, and videos for, Chapter 4. Appendix B includes/describes the codes used in, and supplements videos and figures for, Chapter 5.

Chapter 2
Background

2.1 Self-assembly

2.1.1 Definition and importance

Nature is a giant self-assembling plant. From galaxies to living cells, from molecular crystals to virus capsids, all involve the process of pre-existing components spontaneously self-organizing into ordered arrangements [1, 25]. Self-assembly is so ubiquitous that it is astonishingly hard to come up with an examples of things that are not naturally formed from self-assembling processes. The formations of vapor from boiling water and of glass from rapid melt-quenching are perhaps some such examples. However, given the term self-assembly is used broadly and, sometimes, loosely in a wide range of disciplines, careful distinctions need to be made here. The self-assembly definition that we refer to here involves important key words in "pre-existing components","spontaneous self-organizing" and "ordered". Accordingly, a general self-assembly process involves discrete building blocks and an environment in which the building blocks self-organize autonomously into ordered arrangements without human intervention.

Self-assembly can be broadly classified into two types: static and dynamical self-assembly [25, 26]. These can sometimes be referred to as equilibrium and far-from-equilibirum self-assembly, respectively. Examples of static self-assembly include salt crystals, superlattice nano structures [5], and binary nano crystals [27, 28, 29]. Most of the research so far focuses on static self-assembly. Dynamical self-assembly is not yet com-

mon in technology but is ubiquitous in nature; school of fishes, swarm of bacteria or even biological cells all arise through processes of dynamical self-assembly. The key distinction between the two types is the energy flux through the system. For static self-assembly, there is no energy flux, or no energy exchange between the system and its environment, although there may be energy exchange during the evolution of system to an equilibrium state. The system, governed by the principle of free energy minimization, evolves to and resides in free energy minima in its equilibrium states. These minima can be either local or global but they both fix the system's structure and properties unless some external perturbation, e.g. heating, is applied to drive the system out of the minima. Dynamical self-assembly, on the other hand, requires a constant flux of energy to form and maintain its steady states. A stop of this energy flux would disassemble the self-assembly: cells die if there is no energy passing through. This energy flux also provides means for the system to explore a much broader phase space outside of (free) energy minima that often offers novel structures and properties such as self-adaptability, self-healing and self-replicating. Predicting what the system might evolve into, however, remains a great challenge because the theory of dynamical self-assembly is still relatively unknown. There is not (yet) a variational principle, such as the free energy minimization for static self-assembly, that can be used to explain the system behavior. While the theory is still in the making, computer simulation could be utilized as a powerful tool to guide experiments and design novel systems.

Self-assembly is centrally important to designing materials. Much of traditional materials involve the study of self-assembly of fundamental building blocks such as atoms and molecules into thermodynamic phases. Recent scientific breakthroughs have given an unprecedented access to a plethora of building blocks at larger, mesoscopic length scales (10-1000nm) that vary widely in their anisotropic attributes such as shape, surface patterns [1, 30]. These supra-molecules (Fig. 2.1) can be used for self-assembling into novel structures, giving rise to physical properties that are unattainable with the traditional building blocks. With these new "atoms" and "molecules" in hand, self-assembly plays an even

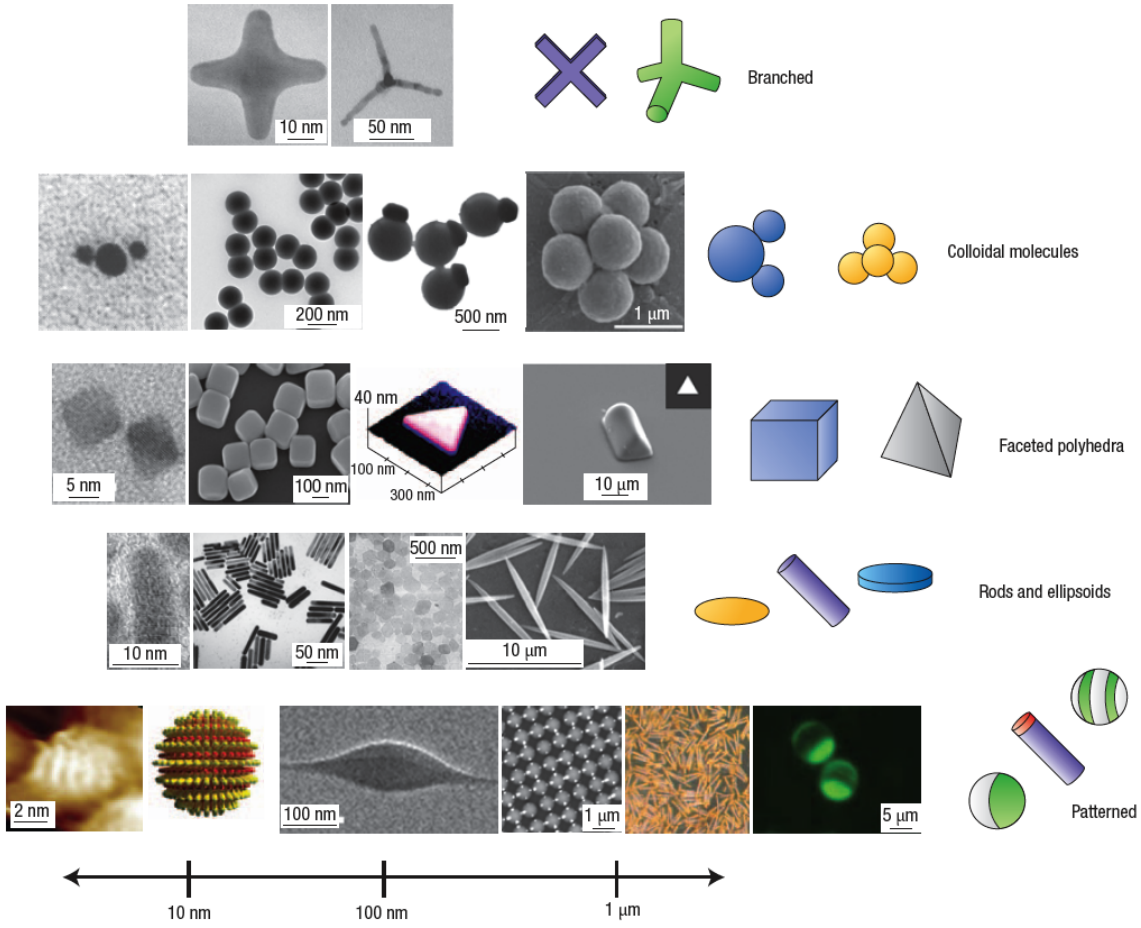

Figure 2.1 Anisotropic building blocks for self-assembly [1]

more important role in designing tomorrow's materials. In addition, self-assembly, as a bottom-up approach, offers potentially a lower-cost route to new materials, compared to other top-down approaches such as lithography, because of its scalability. But to realize the promises of self-assembly, one needs to answer challenging questions such as "What do existing building blocks self-assemble into?" and "How do we design building blocks that self-assemble into a target structure? ". In the following sections, we will discuss the current approaches in addressing these important questions.

2.1.2 Self-assembly approaches

Self-assembly is a science as well as an art. Obviously, it obeys scientific principles such as minimization of free energy (for static self-assembly), the laws of conservation and Newton's laws. For example, a mixture of rods will undergo a transition from liquid to nematic phases to minimize its potential energy while maximizing its orientational entropy, consequently minimizing its free energy. Similarly, cubic colloids are shown to self-assemble into cubic crystals under the effect of entropic depletion interaction [2]. Although the results of these examples may seem obvious, predicting *a priori* what structure a system will self-assemble into in general is not possible. This is especially true when the building blocks are highly complex such as the nano octapod [5]. The situation is further complicated by the fact that, even if we know what the terminal structure should be, there is no guarantee that the system will actually arrive there because of potential kinetic traps. Kinetic traps happen when the system falls into a metastable state that the system, by its own fluctuations, will not be able to escape. These can happen in the forms of jamming, gelation or polymorphism. That is just for self-assembly in an equilibrium system. Once one ventures into the realm of far-from-equilibirum self-assembly, things become even less certain and predictable. Not only because the governing theory for a system in this regime is still unknown but also the sheer size of the phase space poses a great challenge to brute force approaches. These challenges call for holistic approaches that have scientific intuition blended with clever designs of system to navigate a system to more promising lands. Such designs are often inspired by learning from other fields such as biology or sometimes just from one's own intuitive imagination. In the following, we will discuss two common approaches in self-assembly.

The first approach, probably the most common one, is forward engineering. In this approach, the goal is to design building blocks so that they assemble into some novel structure, which may not be known before hand. As pointed out by Glotzer and Solomon [1], the broad anisotropic space of building blocks offer enormous opportunities for imparting the

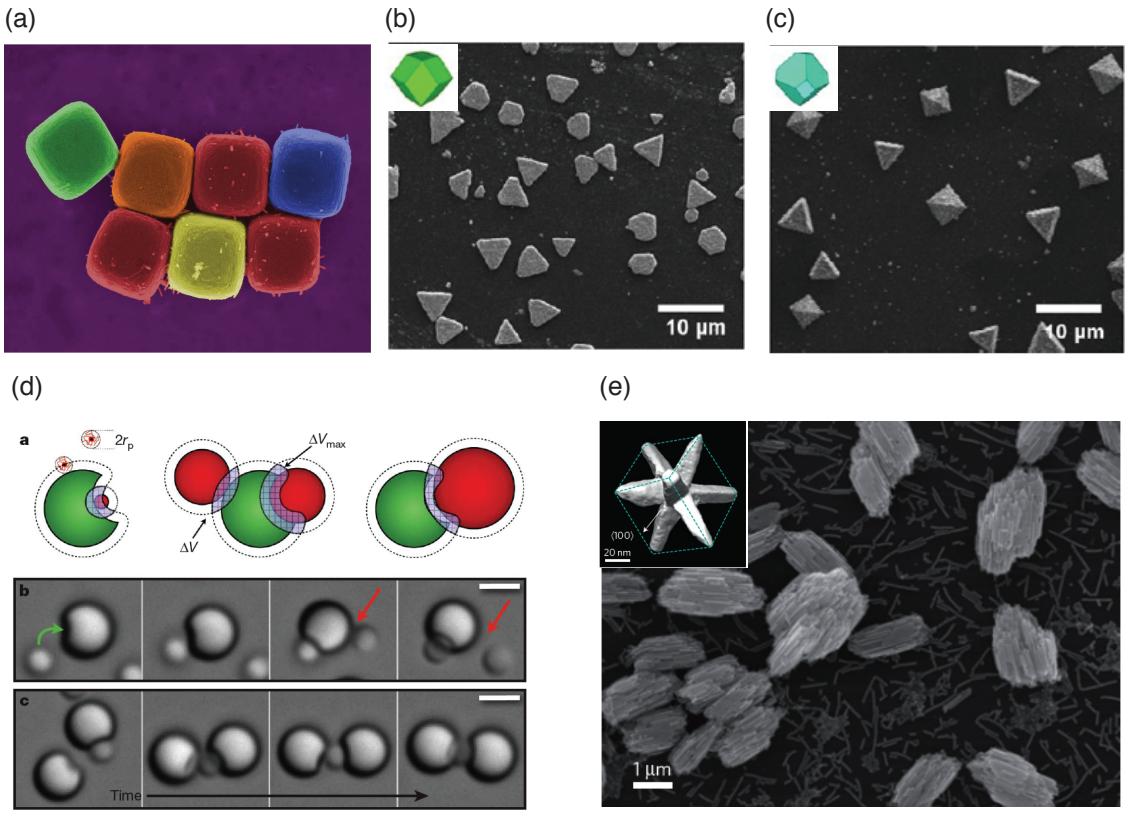

Figure 2.2 Self-assembly of shaped particles. (a) cubic colloids self-assemble into cubic crystals [2]. (b) Rhombic dodecahedra self-assemle into triangular and hexagonal platelike morphologies [3]. (c) Corner-truncated octahedra form Octahedral supercrystals. (d) Self-assembly of lock and key colloids under depletion interaction [4]. (e) Self-assembly of octapod (inset) nano particles into super lattice crystals [5].

right attributes for building blocks to self-assemble into novel structures. However, it also presents huge challenges in selecting the right attributes for the purpose. Here we highlight key design parameters that have achieved considerable success and/or are promising for further advancement.

Shape

Shape is a fundamental attribute of any building block. It is basic, however, it can be a powerful tool in engineering novel self-assembly. The most obvious example is probably how rods behave differently from spheres. In 2D, the elongated shape of rods force the particles to go through a liquid-nematic transition, while spheres will form a hexagonal crystal at

high densities. Recent experiments [3] showed the formation of super-crystals from the self-assembly of nano-crystals of various shapes, including cube, rhombic dodecahedra and octahedra. In addition, not just polyhedra but highly complex shapes such as an octapod [5], a shape that encompasses the center and all the corner points of a cube, can hierarchically self-assemble into super lattice nano-structures that are otherwise impossible. Furthermore, Sacanna *et al.* utilized shape complementariness to demonstrate novel self-assembly of lock and key colloids [4] (Fig. 2.2). In 2012, Damacesno, Engel and Glotzer demonstrated that shapes can give rise to a remarkably rich set of complex packing structures [31]. Although there are differences between self-assembly and packing, which often happens in a theoretical infinite pressure, the finding re-emphasizes the importance of shape in self-assembly and suggests that even more complex structures can be accomplished by tuning shapes.

Interaction specificity

In addition to the usual interaction strength and ranges, interaction specificity has been demonstrated as an important design parameter Fig. 2.3. Interaction specificity, or the directionality of interaction, is common in nature: DNAs bind in complementary pairs and virus capids self-assemble from selective bindings. Inspired by nature, researchers have been successful in using the binding selectivity of DNA strands in guiding the self-assembly to form nano crystals [32, 33] and chains [8]. In another direction, by simply adding immiscible tethers of polymers to specific locations on the particle surfaces, Zhang *et al.* [6] developed a framework that lead to a remarkable set of self-assembled structures. Some of these structures resemble the phases resulting from block copolymer and liquid-crystal phase-ordering. However, when the shapes are tuned in more exotic fashion, the interaction specificity conspires with the shape anisotropy to give rise to new kinds of ordering, including a hexagonally packed columnar phase. Follow up studies in this direction for nanorods [34, 35], cubes [36, 37] and V-shaped particles [38] yields even richer phase behavior that are not otherwise attainable. Finally, interaction specificity can also be achieved by

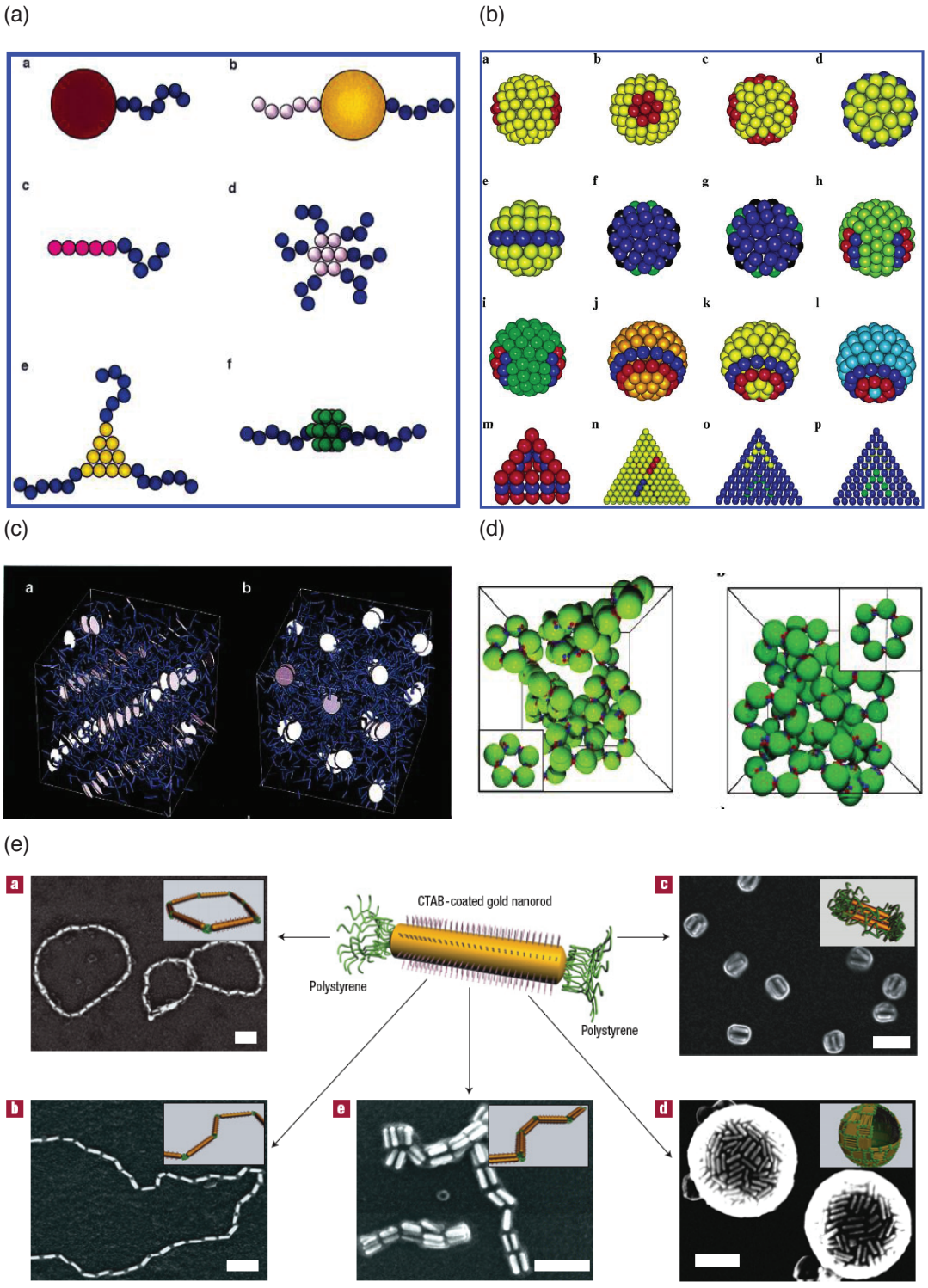

Figure 2.3 Self-assembly of from building blocks with directional interactions. (a) Building blocks with attached tethers [6]. (b) Building blocks with interaction patches [7]. (c) Hexagonally packed columnar phase formed by 120 tethered nanodisks from two views. The disks are similar to particle b in (a) but with six tethers attached to it [6]. (d) Rings formed via self-assembly of patchy sphere h in (b) (left) and patchy particle i in (b) (right) [7]. (e) Self-assembly of polymer-tethered gold nanorods into different structures in selective solvents: a- rings, b-chains, c-bundles of nanorods, d-nanospheres, e-bundles of nano chains [8].

having attractive patches on specific sites of a building block, which is called a patchy particle [7]. Zhang and Glotzer demonstrated that these patchy particles self-assemble into a variety of structures that include rings, chains, sheets, and icosahedra. Interestingly, some of these complex structures such as rings, chains are predictable from the pre-programmed directional interactions. The ability to predict *a priori* the self-assembling structure from the building block attributes demonstrated here suggests that, perhaps with some inverse engineering to inform what kinds of interaction the building block should possess, one could eventually design buildings blocks that self-assemble into a desired structure.

The second approach of self-assembly is inverse engineering. As the name suggests, this approach involves breaking down a given target structure into design rules that are subsequently encoded into its assembling building blocks. The goal is to find the right set of rules that will enable the building blocks to self-assemble into the target structure. For an example, how does one design building blocks that will self-assemble into the ring structure found in [7], which includes six spherical particles connecting to each other Fig. 2.3 b? One way is to stick two patches on each sphere that are 60 degrees apart, as it was done in the paper. In this method, one could also replace the patches by DNA complementary strands for the specific binding. Another alternative is to design the building block as a V-shaped structure that consists of 2 spheres making a 120 degree angle with the central one. The ends of the V-shape can attract each other via attraction patches. All the aforementioned methods involve clever combination of binding sites and particle shape to engineer target structure but do not vary the interaction. One then may want to design interaction potential to achieve the same purpose. Recently, researchers have employed successfully inverse optimization techniques to find the optimal interaction potentials that stabilize target structures [39, 40]. In spite of initial promises, one possible limitation of this approach is that the optimal interaction potentials may not be practical. Rather than optimizing a theoretical potential, Hormoz *et al.* [41] proposed design principles that involve relative interaction strengths of short-range colloidal potentials to maximize yields in self-assembly. The principles

have been demonstrated successfully with systems of small number of colloids. From the above methods, we hypothesize that successful implementation of the inverse engineering approach involves identifying the attributes that are essential to the self-assembly and then imparting those attributes to the building blocks. There will often be more than just one way of inverse engineering but the solution practicality will vary greatly with the design parameters.

2.2 Active matter

2.2.1 Introduction

Most of us might have been in awe by "silky" coordinated movement of thousands of fishes or a dexterous change of formation of a bird flock. Then, how one could not be fascinated by a grand herd of hundreds of thousands of caribous migrating north in a surprisingly ordered fashion? Beyond the natural appreciation, one may inevitably ask "how could such a large number of animals coordinate movement so adeptly with presumably the awareness of only few neighbors?" and "what drives the dynamics of the group and in what ways?". Answering these types of questions serves both as a motivation and a challenge to the field of active matter. It is a field that studies systems of self-driven particles or active particles that convert stored or ambient free energy into their own systematic movement [42]. These particles are not limited to macroscopic units such as birds and fishes but can be on all length scales, from nanometer (active nano particles) to micron (self-propelled colloids, bacteria) to meters (animals). The self-driving force is what adds complex, novel behavior to an active system and distinguishes it from other classes of driven systems such as sheared fluids or directed assembly using external fields. The difference is that, in an active system, energy input needs to be applied directly to the particles, as opposed to via a medium, and the particle directions are not imposed by external fields.

Active matter [43, 44, 45] as a field can be regarded as a branch of condensed matter

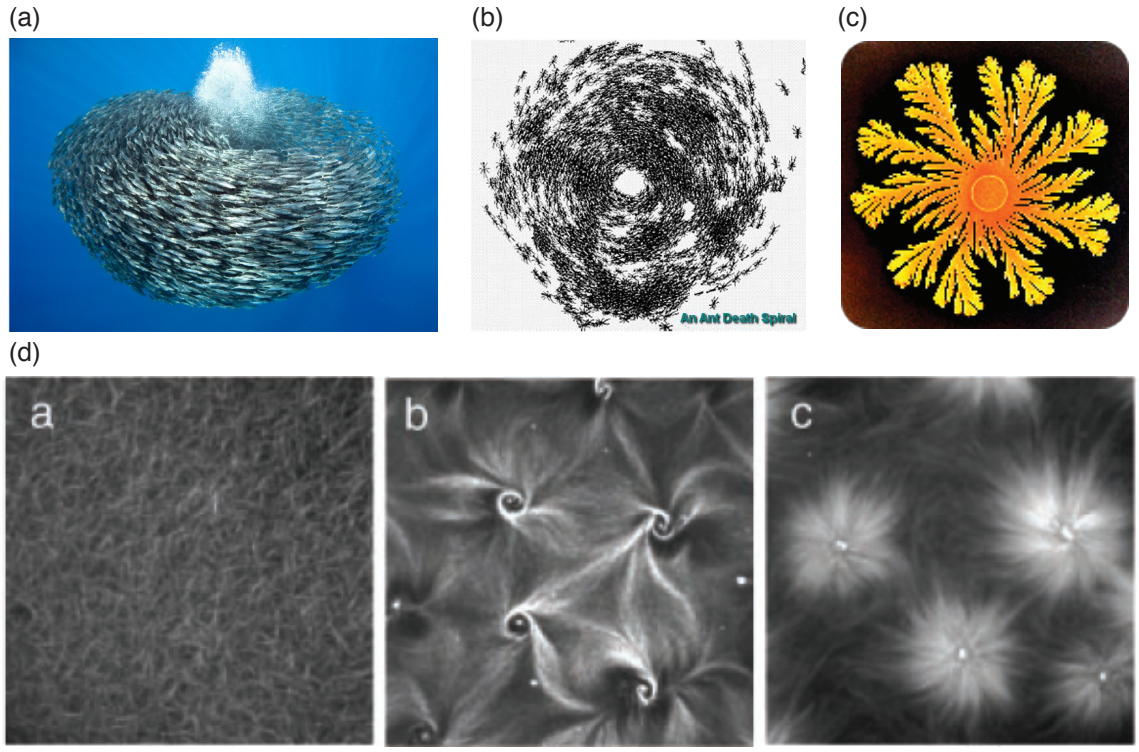

Figure 2.4 Examples of (active) biological self-assembly. (a) Vortex of fishes [9]. (b) ant circle of death: Army ants blindly follow circular trails of pheromone excreted by them until they die of exhaustion [10].(c) a swarm of bacteria [11].(d) Microtubule filaments driven by kinesin complexes, or simply motor proteins, transform from randomly oriented to vortices and eventually asters as the density of kinesin increases from left to right [12].

physics that focuses on far-from-equilibirum regimes. Scientists from diverse disciplines such as physics, biology, engineering approach active matter at different angles and techniques. However, all share some common goals. First, understanding the generic behaviors of active matter across different length scales, living and not, has become an important priority. The achievement of this goal will have far-reaching impacts, not only in explaining the swarming phenomena but also potentially elucidate extraordinary properties inherent to living matter such as adaptation and reproduction. Approaches to this goal have been a combination of statistical mechanics theory, computer modeling and experiments. In spite of encouraging findings so far, this goal still remains distant and particularly challenging because of the problem complexity. Second, the application of what we learn from active matter may ultimately lead to the realization of truly active, smart materials–ones that can,

for example, dynamically change their properties on demand. To this end, extracting and applying a minimal set of rules from biological system to materials can be a fruitful approach. Alternatively, one could employ the self-assembly approaches discussed in the previous section using computer simulation to design and predict behavior of active materials.

In the following section, we will briefly discuss the recent effort and progress of the field of active matter.

2.2.2 Summary of the literature

The last two decades or so have witnessed significant progress toward understanding and realizing active matter. Relying on minimal models and computer simulation, researchers have uncovered a wealth of strange behavior of active systems that are not possible in a typical system, including anomalous statistical fluctuation [46, 17], novel phase transitions [13], emergent collective behavior, and pattern formation [47, 24]. Some of these interesting properties have been recently verified and demonstrated experimentally, taking us one step closer to realizing truly active materials. The field now is entering an exciting era where the experimental techniques are ripe to test and take the vast body of theoretical findings to the next step of practicality. In the following paragraphs, we will discuss briefly the recent advancements in theory, model development and experiments.

Agent-based (microscopic) approach

We will start with a review of the agent-based (microscopic) models (Fig. 2.5) adopted first in the field. In his pioneering work, Vicsek and co-workers [13] modeled the dynamics of point particles, where each moves at a constant velocity and assumes the average direction of its neighbors' with an added angular noise. In spite of the simplicity, the model shows a novel transition from disordered to ordered states, in which the particles move in the same direction, as the noise decreases or number density increases. The long-range order

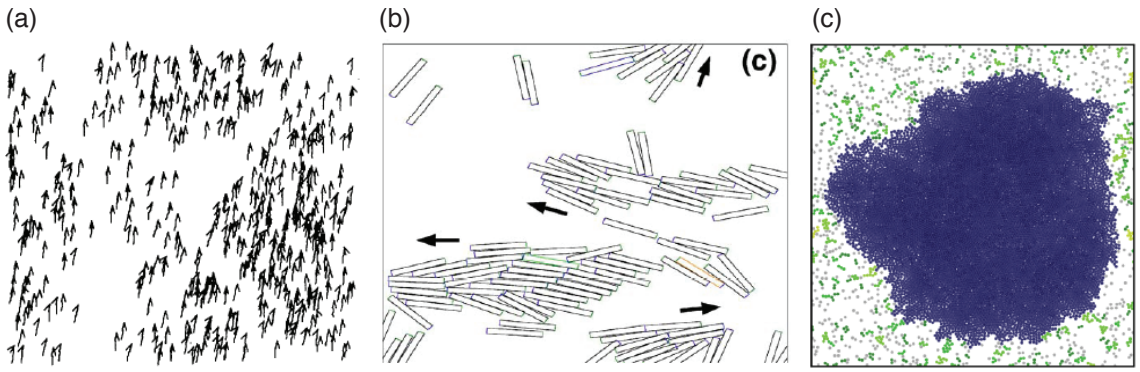

Figure 2.5 Models of self-propelled particles. (a) Particles moving in the same direction in the Vicsek model [13]. (b) Self-propelled rods interacting via excuded volume cluster into nematic ordering [14]. (c) Self-propelled hardcore particles phase-separate into dense and gas phases [15]

is surprising because the 2D XY model [48], which shares many similarities, does not exhibit any long-range order for non-zero noise. Later, Toner and Tu explained how this happens due to the added active term using field theory [49]. The Viscek model lead to a host of follow-up work [50, 51, 52], including the effort in elucidating the elusive nature of the phase transition. In spite of the support for a continuous phase transition [13] and that subtle change in the model, including how noise is introduced, could alter the nature of the transition [53, 54], a currently more-widely-agreed-one theory is of discontinuous transition [55, 56, 57, 58].

In an attempt to model biological swarming such as bird flocking, Couzin *et al.* models particle interaction via three zones: attraction, orientation and repulsion, qualitatively similar to that of real animals. The results show a remarkable resemblance of natural swarming behavior and give first evidence of collective behavior in animal groups. Another alternative in modeling the interaction between active particles is using a pair-wise potential, e.g. Morse potential, as introduced first by Levine in 2000 [47]. Employing this method, researchers have shown a wealth of structures and behavior that further elucidate how self-propelled particles self-organize [47, 59, 60, 61, 62, 21]. Recently, by adding a hard core to the self-propelled particles, mimicking colloidal particles, researchers discovered interesting phenomena, including phase separation into dense-gas phases and crystalizing at critical

density lower than that in corresponding non-active system [15, 63, 64]. In addition to self-propelled point particles, a considerable effort has focused on modeling active rods [14, 65, 66, 67]. In 2006, motivated by aggregation phenomena in gliding bacteria, Peruani *et al.* studied the collective behavior of 2D self-propelled rods interacting via excluded volume [14]. They showed that the rods undergo clustering that are facilitated by high packing fraction and length-to-width ratio. This behavior is also observed in a minimal model developed later for polar point particles that exhibits other interesting phenomena [66].

Continuum (macroscopic) approach

Another useful approach in describing macroscopic behaviors of an active system is by coarse-graining the system using a number of continuum fields. The evolution of the fields are obtained by solving a set of hydrodynamic equations that are modified from the established liquid crystal hydrodynamics to include new active parameters [68]. This can be done through three approaches [45]. The first involves simplifying a microscopic model and then applying statistical mechanics tools to coarse-grain the model to obtain long-time scale solutions [69, 70]. While this approach can provide direct connections between parameters of the macroscopic equation with specific microscopic mechanisms, it is usually difficult to be carried out without approximations. In the second approach, the hydrodynamics equations are phenomenologically obtained by treating the active system as a result of applying a small perturbation to a well-defined equilibrium state. The perturbation is assumed to be small so that the system is still in a linear non-equilibirum regime and its hydrodynamic equations can be systematically derived using Onsager procedure. An obvious drawback of this approach is that most active states are not in a linear regime and therefore can not be described by the method. Lastly, the more popular and practical approach is to write directly hydrodynamics equations for macroscopic fields [49, 71, 72, 46] with the proper addition of active terms. In the following paragraph, we will discuss in detail notable works using

these approaches.

In their pioneering work, Toner and Tu proposed a continuum model that explains the physics found in the Vicsek model. The system is characterized by two continuum fields, number density and velocity, which can be expressed by the position vector and unit vector of instantaneous particle orientation. The active term, which is the driving velocity in this case, comes into dynamical equations for both the fields. As a result, the mean-field analysis gives two solutions that correspond to disordered and ordered states in the Vicsek model. Using a similar approach, Ramaswamy *et al.* [46] discovered a "giant" fluctuation in number density of vibrated rods on a solid surface, which was later confirmed by experiment [17]. At first, the anomalous fluctuation was explained as a result of spontaneously breaking orientational symmetry of the rods. However, later observation of clustering of self-propelled hard disks without any alignment rule [15] suggests a more generic origin for this ubiquitous phenomenon. On a slightly different apporach, Baskaran and Marchetti, by employing Smoluchowski equation, derived a hydrodynamic theory for self-propelled hard rods on a substrate [73, 74] from the microscopic model in [14]. The model provides a first theoretical analysis of roles of size and shape in active matter. In addition, a continuum model was developed by the same authors to describe bacterial suspensions that interact via hydrodynamics interactions [75]. The authors start with a microscopic model for different types of bacteria and derive coarse-grained hydrodynamics for the system.

Experimental progress

In the last decade or so, significant experimental progress has been achieved in both fabricating individual active particles and designing experiments to demonstrate their novel collective properties. In the following paragraphs, we will discuss the progress of each area in detail (Fig. 2.6).

Since the development of the first self-propelled (nano) rods by Paxton *et al.* in 2004 [76], a wide range of self-propelled particles has been fabricated in different shapes and by

using different self-propulsion techniques. The driving mechanisms can be classified into two categories: internally and externally powered. In the internally powered mechanism, the power source to drive the particle is carried on the particle itself. This can currently be achieved through three mechanisms: self-diffusiophoresis, self-electrophores and bubble release. The directional motion is often obtained by breaking symmetry of the forces by coating different substances, e.g. reactive and inert, on particle surface.

In self-diffusiophoresis, the particle generates a local gradient of concentration or fields around its otherwise homogenous medium through, e.g., chemical reaction between the particle surface and its medium. For an example, a polystyrene Janus particles, coated by platinum on one side, is able to diffuse at an effective rate that is a factor of thirty larger than typical Brownian motion in a hydrogen peroxide solution [77] . The self-propulsion happens due to the decomposition of hydrogen peroxide into hydrogen and water under catalytical reaction with platinum. This generates an asymmetric chemical gradient around the particle surface and, hence, self-propulsion.

The self-electrophores mechanism, which was used to realize the first reported autonomous nano-scale swimmers [76], involves redox reaction between two metallic ends of a bi-metallic swimmer. For example, the nano-rod in [76] is made of platinum and gold ends, which behave as anode and cathode, respectively, in a hydrogen peroxide solution. As the redox reaction happens, a proton flux is generated and moves from the platinum to the gold ends along the rod interface, causing the fluid to move in the same direction. This fluid motion results in a net propulsion of the rod in the opposite way.

In the bubble release mechanism, the self-propulsion comes from the release of bubbles on one side of a Janus particle. For example, a micron silica sphere is coated with platinum on one hemisphere that, again, interacts with a hydrogen peroxide solution to generate bubbles on the surface [78]. As the bubbles grow to a large enough size they will detach from the surface, imparting momentum to the particle that drives it forward.

The external driving mechanism employs an external power source such as magnetic

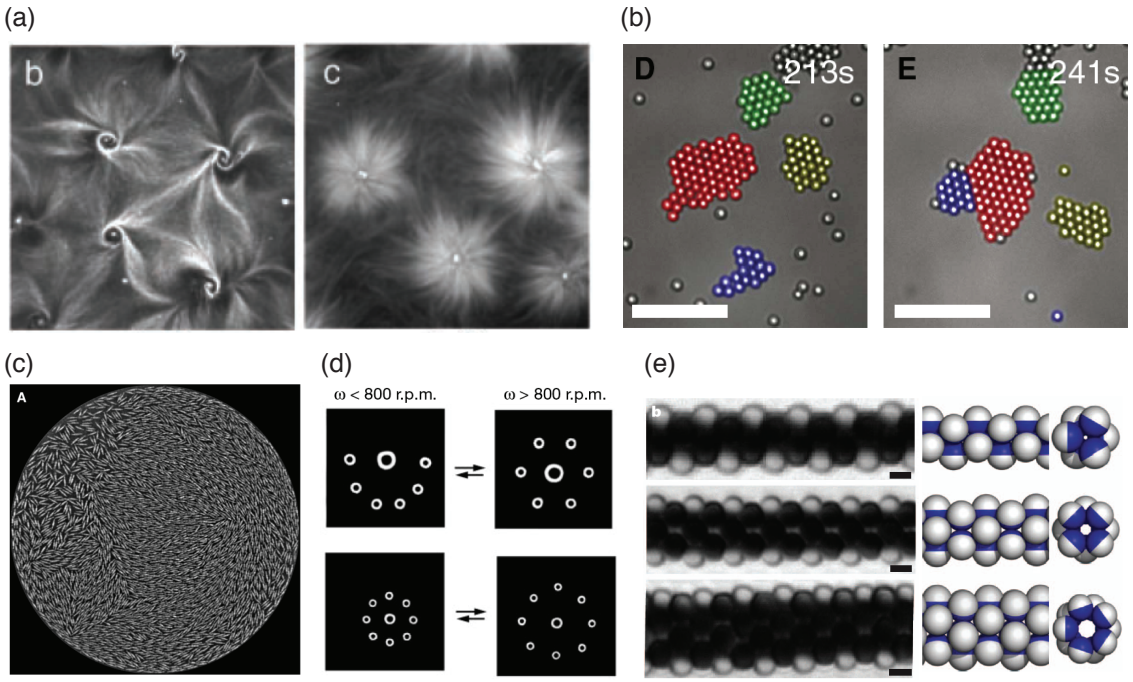

Figure 2.6 Experimental examples of active matter: (a) Microtubules in a mixture with kinesin self-assemble into steady-state vortices and asters as the concentration of kinesin increases (from left to right) [12]. (b) Self-propelled colloids form "living" crystals that self-assemble and break dynamically [16]. (c) Vibrated rods exhibit nematic phase with "giant" number fluctuation, with noticeable dilute and dense regions that move on the surface [17]. (d) Millimeter magnetic disks that are driven by rotating external magnetic self-assemble into different patterns on a fluid surface as the rotation changes [18]. (e) Magnetic Janus particles that are driven by a precessing magnetic field synchronize their motion and self-assemble into different configurations [19].

fields to drive particles [79, 80, 81, 82, 83] . A well-known example of this mechanism is the microscopic, bio-inspired swimmers that mimic motion of bacteria that move around by flagella [79]. Each swimmer is a linear chain of colloidal magnetic particles that are linked by DNA strands and is attached to a red-blood cell at one end. This flexible flagellum-like structure actuates under an external oscillating magnetic fields. As a result, the chain moves in a beating pattern similar to that of bacteria, propelling it in a controllable manner. The speed and direction of a swimmer can be adjusted by changing the external field. Similarly, researchers designed a rigid flagellum-like swimmer that moves by rotating about its body axis under an external magnetic field [83] with great controllability. The swimmer can be controlled to navigate a pre-defined trajectory and even carry a load from one location to another with millimeter-level precision. The ability to transport loads in a controllable

manner of micro swimmers has also been demonstrated previously [81, 82].

The progress in fabricating mesoscopic swimmers has paid the way for experiments on the collective behavior of many swimmers. Recently, experiments [84, 16] demonstrated dynamic clustering of self-propelled colloids as theoretically predicted in [15]. The colloids, propelled by self-phoretic effect (a combination of diffusiophoresis and self-electrophoresis) by catalytic reaction [84] or light-activation [16], cluster into crystals that break and re-form dynamically at low densities and that grow in size with self-propulsion speed at high density. Self-propelled colloids have also been used to explore the "thermodynamic properties" of far-from-equilibrium systems [85]. The authors showed that a suspension of active colloids can be described within the framework of the fluctuation-dissipation theorem with an effective temperature that increases with activity level. Although the concept of effective temperature and its applicability is still an active topic of debate [15], this sort of experiment provides a promising test-bed for a theory of far-from-equilibirum thermodynamics.

Prior to [85, 84, 16], some interesting experiments of active system have been realized with particles on larger scales and driven by external fields. In 2007, using vibrated centimeter rods, the researchers demonstrated a signature of many active systems: long-lived and giant fluctuations. The rods lying on a vibrating flat surface exhibit number fluctuation that does not obey the central limit theorem. In fact, the fluctuations scale with N, the number of particle, as opposed to $\sqrt{N}$ as dictated by the theory for equilibrium systems. Furthermore, the fluctuation decays only as a logarithmic function of time. Another interesting experiment is that comprise of millimeter magnetic disks rotating on a fluid surface by an rotating external magnetic fields [18]. Depending on the rotation speed of the driving field and the number of disks, the system self-assembles into different regular patterns that are controlled by competing forces: the magnetic attraction and hydrodynamic repulsion. Recently, using externally driven Janus particles, researchers demonstrated a linkage between synchronization and self-assembly through activity that gives rise to interesting behavior [19]. The micron silica particles are coated by a thin nickel film on one hemisphere that both rotates

and oscillates in precessing magnetic fields. As a result, the particles synchronize their rotation and self-assemble into microtubes, zigzag chains and planar sheets depending on the external field frequency and precessing angle. Another realization of active matter is *in vitro* experiments with suspension of protein filaments, e.g. microtubules, and motors, e.g. kinesin. The microtubules, driven by kinesin, self-assemble into different steady-state structures, including vortices and asters, depending on the relative concentration of kinesin [86, 12].

Chapter 3
Simulation Models and Methods

3.1 Overview

Since the first simulation of liquids for non-military purposes in 1953 by Metropolis *et al.* [87], computer simulation has become a popular and important front of research investigation. It has been used, for example, to simulate galaxies' collisions, trajectories of space shuttles, and self-assembly of nano-particles. The power of computer simulation, hence its importance, lies in its ability to provide essentially exact results for a model system that are often analytically insolvable and experimentally impractical. For example, even the relatively simple Newton laws become unsolvable for a system of more than two interacting bodies. Further, computer simulation is a wise, sometimes the only viable, choice when the system at hand is too large (galaxy), too small (electrons), too dangerous (atomic explosion), or too expensive (test of space shuttle).

However, computer simulation is not used in lieu of theory and experiment, but rather as a bridge between the two. For a given model, one often has to rely on approximations to describe it because deriving an exact solution may not be possible. This comes with the uncertainty of whether the approximate theory is accurate enough. In this case, computer simulation can be used to test the theory as well as potentially provide insights for further developments. This point is illustrated vividly by the early history of the theory of dense liquids. Before computer simulation came to the scene, the only way to model liquid was using macroscopic spheres such as ball bearings in a very tedious way [88]. Although

the model provides some realistic results, it is just too prohibitively time-consuming and practically difficult to pursue. Therefore, it is not surprising when computer simulation became available to scientific community, first simulations were about models of liquids. First Monte Carlo (MC) simulation was carried out by Metropolis *et al.* [87] to investigate equation of state for interacting molecules. Similarly, Alder and Wainwright utilized computer simulation in the first Molecular Dynamics (MD) simulation [89] to study phase transition in hard sphere. Simulation in these examples serves as a confirmation of theory (former example) and a prediction for experiment (later one).

Although Alder and Wainwright's results [89] are a classic example of how simulation can make correct prediction that are sometimes well ahead of theory and experiment, simulation results should always be validated by experiments whenever possible. The fidelity of simulation results can always be questioned if they do not come from a theoretical background or are not confirmed by an experiment. On the other hand, simulation provides physical insights and promising "shortcuts" that are otherwise not possible to experiments. For an example, the simulation of tetrahedral patchy spheres in [90] can be a great starting place if one tries to self-assemble the diamond structure experimentally. Without the simulation prediction, the experimentalist would have to resort to trial-and-error methods to explore larger phase space that are probably much more time- and cost-consuming. To this end, computer simulation is playing an increasingly important role because of two reasons. First, recent advancement in computing technology enables much longer, larger and cheaper simulations that make modeling virtually any system a relatively simple task. Second, new advancements in theory and experiment nowadays increasingly depends on simulation as researchers venture into less-known and more complex scientific territories. The work in this thesis is an example of how computer simulation is used to predict behaviors of complex systems that can later be verified by experiments.

Simulation of a typical system of, say, liquid usually involves two elements. First, the system at hand needs to be coarse-grained properly into a tractable and reasonable model.

This involves using phenomenological pair potentials (e.g. Lennard-Jones) or empirical ones (e.g. DLVO) to model interatomic interactions. These coarse-grained potentials enable reasonably accurate approximation of the real system without having to deal directly with the complexity, e.g. quantum mechanics, of the actual interactions in ideal cases. The coarse-graining step also involves representing the particle shape and size. This can often be achieved by representing a spherical particle by a "hard" potential such as Lennard-Jones (LJ) ("hard" is used because LJ allows some overlapping, although small) and a non-spherical shape as a composite body of small spheres. Second, once the coarse-graining for the system is accomplished, a proper simulation method needs to be selected for the model. Depending on the nature of the system, such as at a constant temperature or energy, in a solution or not, NVT or Brownian Dynamics simulation methods, for examples, could be employed. In the following sections, we will discuss in more details about the coarse-grained pair potentials and simulation methods used in this thesis.

3.2 Coarse-grained pair potentials

3.2.1 Lennard-Jones potential

Lennard-Jones potential, originally developed to model interaction between Argon atoms, has become one of the most used pair potentials in Molecular Dynamics. It represents a short-range repulsive core and a long-range attractive tail by the following form

$$U_{LJ}(r_{ij}) = 4\varepsilon[(\frac{\sigma}{r})^{12} - (\frac{\sigma}{r})^{6}] \tag{3.1}$$

where $r = r_{ij}$ is the distance between two particles i,j. The potential has a negative well depth of ε and is zero at $r = \sigma$. For $r \leq \sigma$ the potential becomes increasingly steep or strongly repulsive, thus giving the particle an effective hard core of diameter σ. The term $(\frac{\sigma}{r})^6$ makes the first derivative of the potential negative and enables the long range attraction

for $r > 2^{\frac{1}{6}}$. The long range attraction is often truncated at a cutoff radius, e.g. $r_c = 2.5\sigma$, for 1, reducing the computational expense in a distance range that the potential has negligible effect 2, modeling electrostatic screening of a solution on a long range interaction. In this case, the potential should be shifted to zero to avoid potential discontinuity at the cutoff radius. The truncated and shifted LJ potential has the following form

$$U_{LJ}(r) = \begin{cases} 4\varepsilon[(\frac{\sigma}{r})^{12} - (\frac{\sigma}{r})^{6}] + 4\varepsilon[(\frac{\sigma}{r_c})^{12} - (\frac{\sigma}{r_c})^{6}] & r < r_c = 2.5\sigma \\ 0, & r \geq r_c = 2.5\sigma \end{cases} \tag{3.2}$$

Note that the equations 3.1 and 3.3 are for a pair of particles of the same diameter σ. For a pair of different diameters, the LJ potential is shifted to the surface of the particles to achieve the desired diameters. The shifted potential has the following form

$$U_{LJ-shifted}(r) = \begin{cases} 4\varepsilon[(\frac{\sigma}{r-\delta})^{12} - (\frac{\sigma}{r-\delta})^{6}], & r < r_c + \delta \\ 0, & r \geq r_c + \delta \end{cases} \tag{3.3}$$

where $\delta = d_1 + d_2$, d_1 and d_2 are the diameters of particle 1,2 respectively.

3.2.2 Weeks-Chandler-Andersen potential

Weeks-Chandler-Andersen (WCA) potential is a special case of LJ potential in which the long range attraction is eliminated. Mathematically, WCA is a LJ being truncated and shifted at $2^{\frac{1}{6}}$. The potential has the following form

$$U_{LJ}(r) = \begin{cases} 4\varepsilon[(\frac{\sigma}{r})^{12} - (\frac{\sigma}{r})^{6}] + \varepsilon, & r < r_c = 2^{\frac{1}{6}}\sigma \\ 0, & r \geq r_c = 2^{\frac{1}{6}}\sigma \end{cases} \tag{3.4}$$

WCA potential represents only excluded volume of a spherical particles and is often used to model hard particles. For example, a hard triangle can be modeled as a rigid body composing of many smaller WCA spheres.

3.2.3 Morse potential

Morse potential is a soft potential that allows a varying degree of overlapping between two particles and has the following form

$$\vec{U}_{Morse}(\vec{r}) = C_r \exp\left(\frac{-\vec{r}}{l_r}\right) - C_a \exp\left(\frac{-\vec{r}}{l_a}\right) \tag{3.5}$$

where $r = r_{ij}$ is the distance between two particles i,j. The potential shape can be adjusted flexibly to various forms by tuning the four parameters C_r, repulsion strength, C_a, attraction strength, l_r repulsion length and l_a attraction length. Unlike LJ potential, Morse potential does not really give a particle an effective diameter because of its soft core. However, Morse potential can be very useful in studying the effect of potential energy because of its tunability. In this thesis, the Morse potential is employed to investigate how interaction pair potentials influence swarming behavior of self-propelled particles by tuning it to various profiles ranging from purely attractive to pure repulsive. For more details of how the Morse potential is implemented, the reader can refer to Chapter 4.

3.3 Molecular Dynamics methods

3.3.1 Overview

Molecular Dynamics (MD), as the name suggests, describes the dynamics of a system that typically comprises a large number (hundreds to millions) of small particles with length scale ranging from 10 to 1000 nm. Examples of real systems that can be modeled using MD include a suspension of colloids, a solution of nano particles, or a mixture of folding proteins. Because of the large system size, it is impossible to solve for the system dynamics analytically. Instead, the system dynamics is obtained by numerically integrating the classical Newton's equations over time. In an equilibrium system, MD gives the macroscopic thermodynamics properties of the system under the assumption of ergodicity, which states

that ensemble average equals time average in equilibria. Molecular Dynamics simulations are usually preferred over other simulation types such as Monte Carlo (MC) when the system dynamics are of the interest, in addition to the system final equilibrium properties (MC). For this reason, Molecular Dynamics methods are employed in this thesis. In particular, Brownian Dynamics (BD) and Langevin Dynamics (LD) are employed with proper modifications to model active systems. In following sections of this chapter, the implementation of BD and LD will be discussed in details along with the software packages utilized in the thesis.

3.3.2 Modified Langevin Dynamics for active particles

Langevin Dynamics

Langevin Dynamics, named after a French physicist – Paul Langevin, is a simplified mathematical approach that accurately describes the dynamics of a particle of a system of particles in a viscous fluid. As a particle moves through a fluid, it is subject to a friction force from the fluid, forces from random collisions with surrounding fluid particles and interaction with other neighboring particles. Langevin Dynamics models the forces through the following equation.

$$m_i \frac{\partial \vec{v}_i(t)}{\partial t} = \vec{F}_i^C(\vec{r}_{ij}(t)) + \vec{F}_i^R(t) + \vec{F}_i^D(\vec{v}_i(t)) \tag{3.6}$$

$$I_i \frac{\partial \vec{\omega}_i(t)}{\partial t} = \vec{\tau}_i^C(\vec{r}_{ij}(t)) + \vec{\tau}_i^R(t) + \vec{\tau}_i^D(\vec{v}_i(t)) \tag{3.7}$$

where m_i and I_i are the mass and moment of inertia of the particle. Because the terms for translational and rotational motion are similar, we only describe in details the terms for translational motion. $\vec{F}_i^C$ is the sum of conservative forces, or the pair-wise interaction forces, between the particle i with all of its neighbors.

$$\vec{F}_i^C(\vec{r}_i(t)) = \sum_{i \neq j} -\nabla U(\vec{r}_{ij}(t)). \tag{3.8}$$

where $\vec{r}_{ij} = \vec{r}_i - \vec{r}_j$ and $U(\vec{r}_{ij})$ is the interaction potential. $\vec{F}_i^D$ is the friction force acting on the particle by the fluid and is modeled by:

$$\vec{F}_i^D = -\gamma m_i \vec{v}_i(t) \tag{3.9}$$

The random force and drag force are related through the fluctuation-dissipation theorem,

$$\langle \vec{F}_i^R \rangle = 0 \tag{3.10}$$

$$\langle \vec{F}_i^R(t) \vec{F}_j^R(t') \rangle = 2\gamma k_B T \delta_{ij} \delta(t - t') \tag{3.11}$$

where γ is the Stoke's drag, which is proportional to fluid viscosity, T is the temperature and k_B is the Boltzmann constant. δ_{ij} is the Kronecker delta function and $\delta(t)$ is the Dirac delta function.

The Dirac delta function $\delta(t)$ is approximated as $\frac{3{R_i}^2}{\Delta t}$, where R_i is a random number uniformly distributed in [-1,1]. The factor 3 is to ensure the distribution of $\delta(t)$ approaches normal distribution in the limit of large number particle. Plugging in the new formula of $\delta(t)$ into equation 3.11 gives us

$$\langle \vec{F}_i^R(t) \vec{F}_j^R(t') \rangle = 6\gamma k_B T \delta_{ij} \frac{R_i^2}{\Delta t} \tag{3.12}$$

Modified Langevin Dynamics

The activity of a particle is modeled by simply adding a force or torque to the equations of motion 3.6 and 3.7. In this thesis, a constant force and constant torque are added to model self-propulsion and self-rotation respectively. The reader can refer to Chapter 4 for self-propelled particles and Chapter 5 for self-rotated particles for more details.

Code Implementation

The Langevin Dynamics is implemented by modifying the Brownian Dynamics integrator of HOOMD Blue [91, 92]. (Note that in spite of the name, the the current Brownian Dynamics integrator of HOOMD Blue (2013) actually models Langevin Dynamics.) However, instead of applying the Brownian forces to the constituent particles of a body and calculating Brownian torques from the forces as currently implemented in HOOMD Blue, Brownian forces and torques are applied separately to the body. The Brownian forces and torques can be assigned by specifying the translational, γ_t, and rotational, γ_r, drag coefficients and the temperature. The coupling between translational and rotational diffusions can be realized by relating the drag coefficients in a right ratio that depends on the body geometry. For an example, $\gamma_r = \frac{4}{3}\sigma^2\gamma_t$ for a spherical disk of diameter σ. The modification speeds up the code because the number of iteration loops in calculating Brownian force and torque decreases from the number of constituent particles to the number of bodies. Furthermore, the modified version should model the Brownian Motion more realistically because the Brownian forces should be distributed on the bodies, not the constituent particles. As the matter of fact, sums of the normally distributed forces on the constituent particles do not equate to the normal distribution of force with the same mean and variances. Instead, the mean and variance are the sums of the constituent means and variances, respectively.

The active torque and force are added to a body by two separate plugins – a plugin is a piece of software developed by an user to add a feature to HOOMD without having to modify its source code. The force plugin adds a constant force to a group of particles in their velocity directions. The torque plugin adds a constant torque, specified either in clockwise or counter-clockwise directions by the user, on particles of a same type.

Code Verification

The LD code was verified correct by reproducing the fluctuation-dissipation theorem, which determines that in time large time scale ($t \gg \tau_r = \frac{1}{\gamma}$, where τ_r is the characteristic relaxation

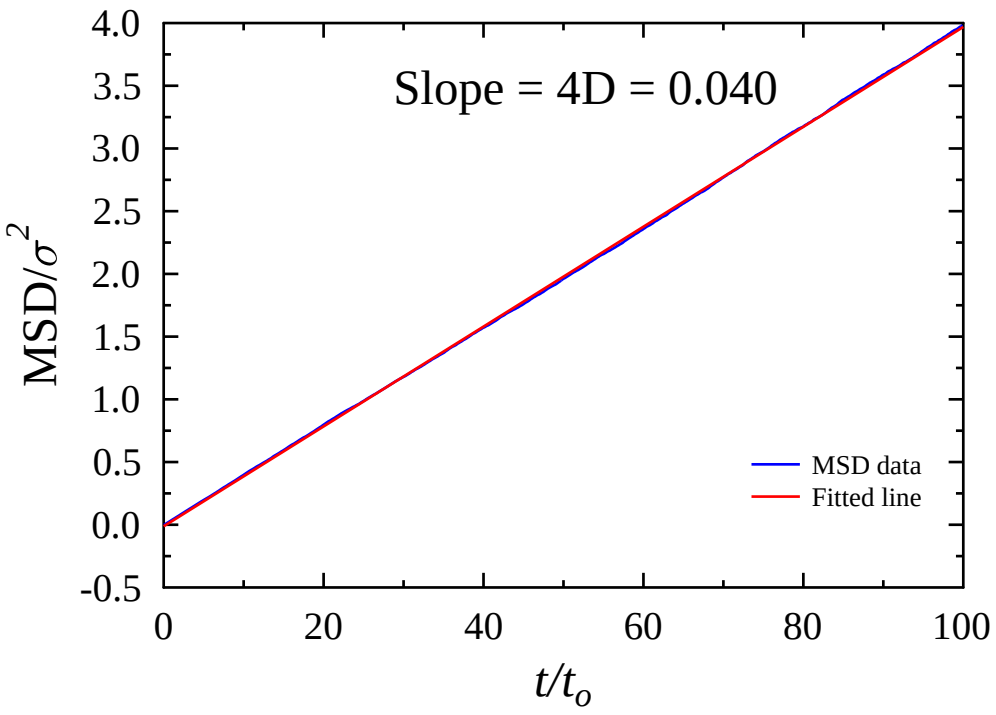

Figure 3.1 MSD over time for a system of 16384 gears simulated by the LD code at temperature of 5. Each gear has a mass of 5 and a translational drag coefficient of 100. The theoretical translational diffusion coefficient is, according to equation 3.14, 0.01. The value is exactly equal to $\frac{1}{4}$ of the slope of the MSD versus time, thus satisfying the fluctuation-dissipation theorem.

time) the mean squared displacement (MSD) of a particle in a 2D system relate to its diffusion coefficient by [93]

$$< {r_i}^2 >= 4Dt \tag{3.13}$$

t is time and D is the diffusion coefficient and is determined by

$$D = \frac{k_B T}{\gamma m} \tag{3.14}$$

The relations 3.13 and 3.14 are confirmed in the Fig. 3.1. The code is further verified by reproducing the results in [59] as discussed in Chapter 4. The plugins are verified by comparing the steady state velocities and the time constants (to reach the values) of non-interacting particles in a zero-temperature system with easily-obtained theoretical values.

3.3.3 Modified Brownian Dynamics for active particles

Brownian Dynamics

In the limit that the viscous drag γ goes to infinity, LD becomes BD. In this regime, viscosity is dominant while inertia is neglected. There is no acceleration associated with the motion but random, abrupt changes in velocity and position are expected. The equations of motion for BD are as following

$$\vec{v}_i(t) = \frac{\vec{F}_i^C D}{k_B T} + \sqrt{2D}\vec{F}^R(t) \tag{3.15}$$

$$\vec{\omega}_i(t) = \frac{\vec{\tau}_i^C D_r}{k_B T} + \sqrt{2D_r}\vec{F}^R(t) \tag{3.16}$$

D_r is rotational diffusion coefficient; other terms are explained in the previous sub-section. $\vec{F}^R(t)$ is a delta-correlated stationary Gaussian process with zero-mean in all the dimensions, satisfying

$$< {F_u}^R(t) >= 0 \tag{3.17}$$

$$< {F_u}^R(t){F_u}^R(t') >= \delta(t-t') \tag{3.18}$$

where u is either x,y,z. In the limit of high viscosity but where inertia still plays a role, i.e. in a valid domain of LD, the diffusion coefficients are related to the viscosity as following [94]

$$D = \frac{k_B T}{\gamma m} \tag{3.19}$$

$$D_r = \frac{k_B T}{\gamma_r} \tag{3.20}$$

where the Stokes drag coefficients γ and γ_r are determined by viscosity and the particle geometry. For a sphere of radius R, the drag coefficients are

$$\gamma = 6\pi\eta R \tag{3.21}$$

$$\gamma_r = 8\pi\eta R^3 \tag{3.22}$$

where η is viscosity coefficient.

Modified Brownian Dynamics

Similar as in LD, driven force and torque are added to particles through two plugins. In this thesis, modified LD is used mostly because of two reasons. Firstly, as a mesoscale particle is driven, its inertia is likely to play an role in its dynamics. Secondly, with LD we can flexibly turn off the noise ("temperature") term to study a wider range of dynamics. The BD code is used to reproduce some literature results such as [63] and compare its with results with using LD. We also compare our results using LD with BD in Chapter 5. In general, both BD and LD (with relatively high drag coefficients) give similar results.

Code Implementation

The BD is implemented in both Central Processing Unit (CPU) and Graphical Processing Unit (GPU) using second order stochastic Runge-Kutta algorithms [95]. The algorithm is chosen because it gives relatively better accuracy while still being computationally efficient [95]. The algorithm consists of two steps: Predictor and Corrector. In the Predictor step, the positions of a body are calculated by a conventional BD algorithm. The positions are updated with corrected terms calculated from the old and newly-obtained positions. In the following, the detailed algorithm is presented for translation; a similar procedure applies for rotation.

1. Predictor step (at time t)

(a) Calculate forces, including Brownian forces, acting on the bodies from $\vec{r}_i$ and T and record it as F_i^a
(b) Update velocities $t + \Delta T$ by equations 3.15
(c) Update positions by using a conventional BD algorithm $\vec{r}_i(t + \Delta t) = \vec{r}_i(t) + \Delta t \vec{v}_i(t)$

2. Corrector step (at time $t + \Delta t$)
   (a) Calculate forces, excluding Brownian forces, acting on the bodies from the new $\vec{r}_i(t + \Delta t)$, record it as F_i^b
   (b) Add a corrected term to the position $\vec{r}_i(t + \Delta t) = \vec{r}_i(t + \Delta t) + \frac{(F_i^b - F_i^a)D}{2k_BT}\Delta t$

The code is implemented by modifying the current Brownian Dynamics integrator of HOOMD Blue.

Code Verification

The code was verified correct by different ways. First of all, the fluctuation-dissipation theorem was confirmed by reproducing the relation between MSD and time. As shown in the Fig. 3.2, the MSD scales with $4Dt$ as expected for a 2D system. Secondly, the code was further verified by reproducing the results reported in [63]. Lastly, the code was independently verified by Daniel Beltran from Prof. Ron Larson's group and Ben Schultz from Prof. Sharon Glotzer's group, from the Chemical Engineering Department, University of Michigan at Ann Arbor, in their researchs using the BD code.

3.4 Software packages

The research has been conducted using various software, which are duly acknowledged and described in the following sections.

3.4.1 HOOMD Blue

The simulations in this thesis have been carried out using HOOMD Blue [91, 92]. HOOMD, standing for Highly Optimized Object-oriented Many-particle Dynamics, is a highly-accelerated Molecular Dynamics Software package that employs paralleling computing and

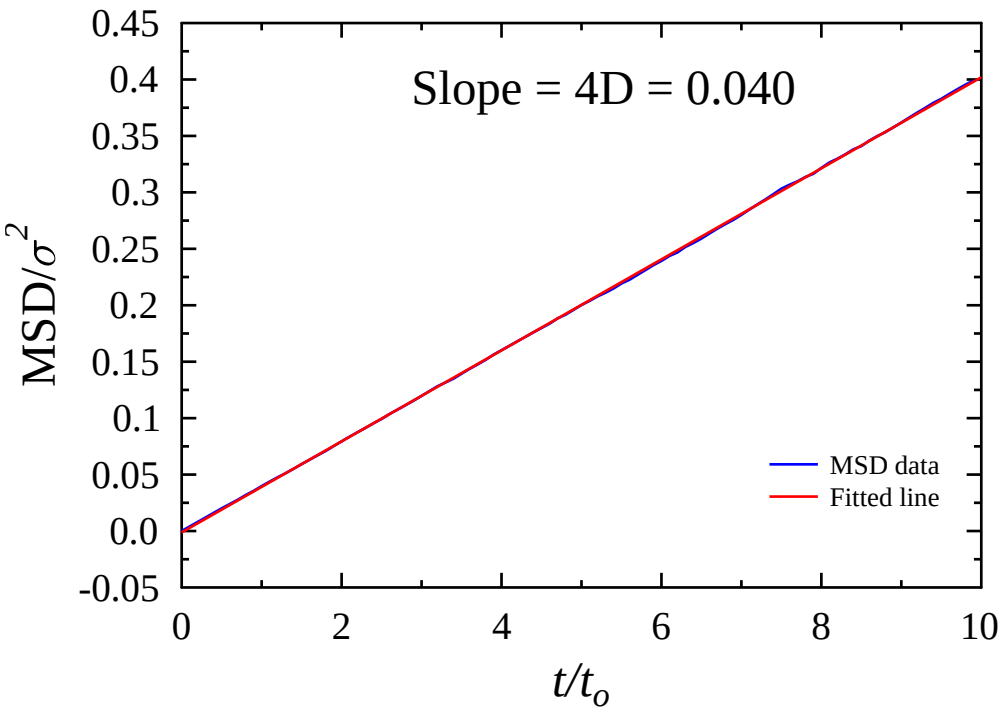

Figure 3.2 MSD over time for a system of 10000 gears simulated by the BD code with translational diffusion coefficient of 0.01.The value is exactly equal to $\frac{1}{4}$ of the slope of the MSD versus time, thus satisfying the fluctuation-dissipation theorem.

runs on both CPU and GPU. HOOMD was originally developed by Dr. Joshua Anderson at the Iowa State University [91] and is now being primarily developed and maintained by the Glotzer group at the University of Michigan at Ann Arbor. It is available to the public under an open source license [92] and it allows users to flexibly add functionalities by using software plugins. In a benchmark, HOOMD run on a GPU is shown to achieve a speed equivalent to LAMMPS [96] parallelized over 50-90 GPU cores [20]. Important reasons for the speed-up include 1) avoid serial code the bottlenecks and 2) slow memory transfers between host and device. HOOMD performs all steps of a computation on the GPU and, thus, avoids all memory transfers between host and device, unless it is needed for disk I/O [20]. HOOMD also utilizes neighbor and cell lists to further speed up its simulations. In each MD time step, particles are binned into cell lists. From these cell lists, each particle is

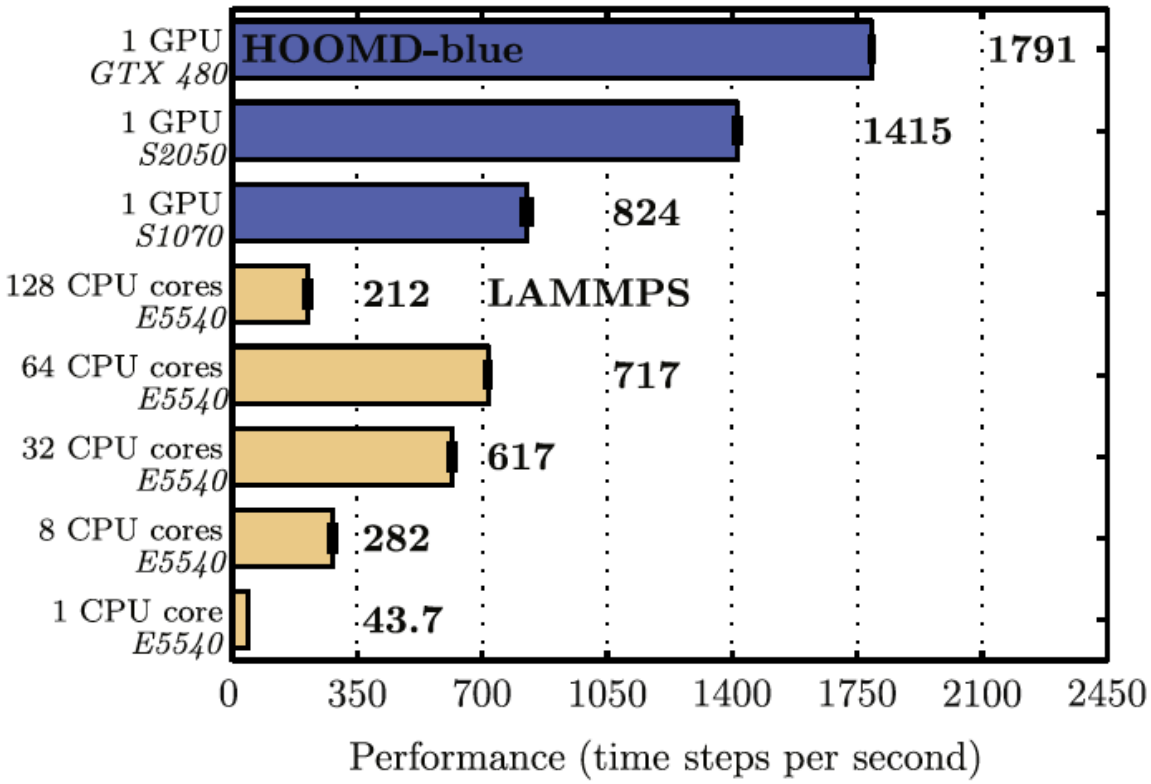

Figure 3.3 Performance measured in time steps per second of HOOMD Blue compared with LAMMPS. The benchmark simulation is one thousand tethered nanorods (14000 total particles) and is performed 50 times for each benchmark [20].

assigned a neighbor list that includes indices of particles within a specified interaction range. The neighbor lists are referred to when pair forces are calculated for each particle, reducing computational costs because only interacting pairs are considered in calculation.

3.4.2 Other software

Visual Molecular Dynamics

VMD is a free software designed for displaying, animating and analyzing large bio-molecular systems using 3-D graphics and built-in scripting. VMD is primarily designed for biological system but may be used for general systems. The visualization software is developed and maintained by the Theoritical and Computational Biophysics Group at the University of Illinois at Urbana-Champaign. In this thesis, VMD were used to visualize snapshots and

dynamics of the system. Customized scripts were also developed to produce videos of swarms in Chapter 4.

Interactive Java Visualization

Injavis, developed and maintained by Dr. Michael Engel, a research scientist in the Glotzer group, is for rendering and analysis of complex atomistic or nanoparticle configurations. It currently includes analysis tools such as the radial distribution function (RDF), diffraction pattern (FFT) and bond order diagram (BOD). Injavis allows the user to flexibly render configurational and dynamical information a molecular system of particles with different shapes into high quality graphics. In this thesis, Injavis was used in combination with other software to render the snapshots and videos in Chapter 5.

VisualizeX

VisualizeX is a visualization software package developed by Dr. Trung Nguyen, a former PhD student of the Glotzer group. The software allow users to visualize and render a molecular system. Particle shapes and other visualization settings such as particle size, ambient lighting can be flexibly set by the user. VisualizeX was primarily used in rendering the images of swarming patterns in Chapter 4.

Packmol

Packmol is a free software package that allows users to generate an initial condition for an MD simulation by satisfying simultaneously constraints such as density and particle shapes. The software is developed by Leandro Martnez, State University of Campinas, Brazil. It was used to generate initial conditions for some simulations in the thesis.

Personal codes

A significant number of code programs have been developed for generating initial conditions, running jobs, analyzing data, and visualizing data. In particular, all the analysis in this thesis were conducted using personally developed codes.

Chapter 4
Self-assembly of Self-Propelled Particles

4.1 Introduction

The emergence of ordered swarms from a collection of autonomous self-propelled agents is a ubiquitous natural phenomenon. In biology, swarming is a common feature of social organisms, and flocks of birds, schools of fish, and herds of buffalo have been described by simple models [24, 44, 71, 97, 98]. Non-biological systems of self-propelled particles, including rotating magnetic disks[18] and microdiodes [99], also exhibit of steady-state swarms [97, 74, 73, 100, 75], and recent work has elucidated many ways the interactions between particles can influence swarm structure [13, 51, 47, 24, 55, 59, 50, 52, 101, 60, 102, 103, 61, 104], primarily in two dimensions.

Understanding how the interactions between agents result in swarms of a particular shape has a wide range of applications, including the distributed control of unmanned vehicles [104], assembly of mobile sensor networks [105], and microscale mixing [99]. Interaction potentials that are qualitatively similar to the potentials that describe nanoparticle interactions but scaled to larger lengths have been utilized to control and reconfigure mobile vehicles flocks that would otherwise require complex and costly centralized control systems to achieve the same task[104, 105]. Self-propelled microsensors powered by alternating electric fields have demonstrated mixing within microchannels [99]. Creating a swarm that performs a preprogrammed task, whether within a microchip or between cities, depends on our ability to robustly control the structure of a swarm through the manipulation of the

interactions between agents.

One inter-particle interaction that has received considerable attention is the generalized Morse potential, first introduced for modeling swarms by Levine *et al.* [47]. In two dimensions, D'Orsogna *et al.* [59] discovered rings, vortex-like swarms, and circular clumps in systems of self-propelled particles interacting via a Morse potential and showed how the swarm stability varies with swarm size. The Morse potential has been used to demonstrate the control of swarming vehicles [104], and in three dimensions was used to model systems of toroidal swarms whose translational motion was tuned with thermal noise [62]. The structural diversity observed for 2D Morse swarms is impressive and it is natural to ask what other sorts of 3D swarms might be stable and how robust their stability is to thermal fluctuations. Unfortunately, no predictive theory for swarm stability currently exists and the parameter space from which 3D Morse swarms can be chosen is enormous. With four Morse parameters and three independent thermodynamic parameters (volume, particle number, and temperature), we rely on computer simulations as the primary tool for predicting the conditions under which swarms are stable, and the structural and dynamical character of potentially achievable swarms.

Here we perform computer simulations of self-propelled Morse particles using graphics processing unit (GPU) optimized software [92] to explore the formation of 3D stable swarms in both thermal and athermal environments and gain insights on their dynamics and stability. Our simulation code allows for sampling of vast regions of parameter space where we observe swarms including tori, hollow shells, and two-dimensional rings. The "phase diagram" we report as a function of Morse potential parameters is richly diverse, with large regions where one swarm is stable over all others, but other regions where swarms are observed over only narrow parameter ranges. We observe notable deviations from equilibrium pattern formation in this far-from-equilibrium system, including assembly of competing swarms at a given state point, and we demonstrate that initial conditions can be chosen to bias the formation of one structure over another. We observe that thermal noise

can influence the stability of one structure over another and we demonstrate how noise can be used to reproducibly and repeatedly switch between different swarms. Beyond these new findings, our work highlights the need for efficient computational tools and predictive analytical techniques for the study of swarm formation, and demonstrates the precise control over swarm morphology that can be accomplished with a model system.

This Chapter is organized following Ref. [21], in which the contents of this Chapter are published. In Section 4.2 we describe the pairwise interaction parameters and "active" particles that define our model, the methods we employ to perform simulations on graphics processing units (GPUs), and the quantities we calculate to characterize swarms and their structure. In Section 4.3 we present the results of our extensive simulations. These results include a "phase diagram" that summarizes the swarms we find in the absence of thermal noise, two case studies for structural transitions induced by thermal noise, and an evaluation of swarm structure sensitivity to initial conditions. In Section 4.4 we discuss similarities and differences of the swarm self-assembly as compared to equilibrium self-assembly. In Section4.5 we conclude with a summary of our work and highlight future possible extensions.

4.2 Model and method

4.2.1 Model

We consider particles interacting via the generalized two-body Morse potential [47]

$$U(r_{ij}) = C_r \exp\left(\frac{-r_{ij}}{l_r}\right) - C_a \exp\left(\frac{-r_{ij}}{l_a}\right) \tag{4.1}$$

where r_{ij} is the distance between two particles i and j, C_a is the attraction strength, C_r is the repulsion strength, l_a is the attraction length scale, and l_r is the repulsion length scale. These parameters can be chosen to model a wide range of interaction types, from purely

repulsive and/or long-range attractive, to particles that can overlap but have an energetic barrier to doing so. To model the motion of self-propelled Morse particles in a thermal bath, we update particle positions using the Langevin equation of motion [106]

$$m_i \frac{\partial \vec{v}_i}{\partial t} = \vec{F_i^C} + \vec{F_i^R} + \vec{F_i^D}. \tag{4.2}$$

Here, m_i and v_i are the mass and velocity of particle i, t is time, and $\vec{F_i^C}$, $\vec{F_i^R}$, and $\vec{F_i^D}$ represent the conservative, random, and drag forces, respectively. The conservative force between two particles is the usual negative gradient of the potential summed over all neighbors

$$\vec{F_i^C} = \sum_{i \neq j} -\nabla U(r_{ij}). \tag{4.3}$$

The random force and drag force are related through the fluctuation-dissipation theorem,

$$\langle \vec{F_i^R} \rangle = 0 \tag{4.4}$$

$$\langle \vec{F_i^R}(t) \vec{F_i^R}(t') \rangle = 6\gamma T^* \delta_{ij} \delta(t - t') \tag{4.5}$$

where γ is proportional to fluid viscosity, T^* is the reduced temperature that is related to real temperature by $T^* = k_B T_{real}$ and δ_{ij} is the Kronecker delta function and $\delta(t)$ is the Dirac delta function. We model particle self-propulsion as in Refs. [59, 62] with a modified drag force

$$\vec{F_i^D} = (\alpha - \gamma - \beta |\vec{v}_i|^2) \vec{v}_i \tag{4.6}$$

where $\alpha - \gamma$ determines the net propulsion strength and β determines the amplitude of the non-linear drag force. The propulsion and drag forces act parallel to a particle's velocity vector and define an optimal velocity $v^* = \sqrt{\frac{\alpha - \gamma}{\beta}}$ towards which particles are driven.

4.2.2 Method

We implement the above model in HOOMD-blue, an open-source GPU-based Molecular Dynamics package developed by our group, which we have extended with packages for calculating and applying self-propulsion forces and the Morse potential via CUDA kernels executed on NVIDIA Tesla S1070 graphics cards[92]. The Morse potential (Eq. 4.1) is truncated and shifted to zero at $r_{ij} = 5\sigma$, which avoids the potential energy drift that can occur with an un-shifted potential. We employ generic units of distance σ, particle mass m and energy ε. The Morse potential energy at $r_{ij} = 0$ is equal to 1ε for $C_r = 2$, $C_a = 1$, $l_r = 1$, $l_a = 1$. The "temperature" of the system is a thermal energy related to real temperature by $T^* = k_B T_{\text{real}}$ in units of ε. The value of k_B is uniquely determined by the choice of real units for energy, distance and mass. The time unit τ is derived from $\tau = \sqrt{\frac{m\sigma^2}{\varepsilon}}$. We update particle velocities and positions using the two-step velocity Verlet integration scheme [107] with $dt = 0.001$ or $dt = 0.005$. Generally we find $dt = 0.005$ to be sufficiently small for reliable integration of the Langevin equation, except for very low values of C and large values of l, where swarm artifacts can appear for $dt > 0.002$. For $N = 600$ point particles in a 20σ cubic simulation box with periodic boundary conditions, a simulation of 2×10^6 time steps with $dt = 0.005$ requires about an hour on a single GPU. The 4000 simulations required to create Fig. 4.2 were completed in three days, and would have required two to three months if performed with LAMMPS [108, 109] on a parallel CPU cluster.

A typical trial run begins with $N = 600$ particles initialized randomly within a 5σ cubic region (cell) centered within the larger 20σ cubic simulation box. Initializing particles within the 5σ cell ensures one swarm is formed from all particles and avoids finite-size effects that could be imposed by having a simulation volume commensurate with the interaction potential length scale. Each component of the particle velocities are initialized randomly from a Gaussian distribution with mean $T^* = 1.0$ and standard deviation $\delta T^* = 1.0$. Henceforth, when we refer to "random initial velocities" we mean they are drawn from this distribution. We typically set $\alpha = 2.0$, $\gamma = 1.0$, and $\beta = 0.5$, and perform 2×10^6 time steps with a step

size of $dt = 0.005$. Simulation runs that differ from these initial conditions are noted and explained. Different system densities result in the same overall swarm morphologies at a given state point, but where the number of swarms observed per simulation and the size of a given swarm can vary from run to run.

The simulation times of 2×10^6 time steps are chosen to allow for sufficient sampling of steady state structures after transient swarms die out. Generally, we find that transients have disappeared after 1×10^6 time steps. We define a steady state swarm for a simulation run if there exists a structure or collection of structures that persist over the final 1×10^6 time steps with a well-defined average and standard deviation for their total energy. We distinguish among different swarms by calculating relative eigenvalues of their moment of inertia tensors and comparing them with the corresponding values that are characteristic to symmetric, circular structures such as spherical shells and rings. If the values match within an allowable tolerance of 10%, the structure is identified as a swarm.

To distinguish between swarms where particles travel about a fixed central point (e.g. a shell - Fig. 4.1b) and swarms where particles travel about a fixed central axis (e.g. a ring - Fig. 4.1c) we define the alignment order relative to particle i

$$A_i = 2\left(\frac{\sum_{j=1}^{N}|\vec{M}_i \cdot \vec{M}_j|}{\sum_{j=1}^{N}|\vec{M}_i||\vec{M}_j|} - 0.5\right) \tag{4.7}$$

where

$$\vec{M}_i = \vec{r}_i \times \vec{v}_i \tag{4.8}$$

is the angular momentum for particle i traveling at a velocity v_i located at position r_i relative to its swarm center of mass. In practice we select A to be the maximum value of A_i from the N measurements for a swarm, indicating the correlations in angular momentum about the axis where they are most correlated. When $A = 0$ particles move in circles whose axes have no average correlation, as is the case for the shell (Fig. 4.1b). When $A = 1.0$ the circular paths traveled by all particles share the same axis, as is the case for the ring

(Fig. 4.1c). In addition to distinguishing between shells and rings, we show that A is useful in characterizing the velocity correlations for the other swarms studied in this work. A metric similar to Eq. 4.7 is used to distinguish 2D vortexes and flocks in Ref. [61].

4.3 Results and discussion

We perform 4000 MD simulations using HOOMD-Blue to determine the athermal steady-state swarms that emerge for Morse particles in 3D in Section 4.3.1. We validate our approach by confirming previously reported swarm behavior from Refs. [59] and [62] and report new swarms and new behaviors including swarm coexistence. In Section 4.3.2 we perform 1760 MD simulations of different initial conditions and find that correlations in angular momentum largely determine the trajectory of a swarm and can influence the steady state swarm observed in coexistence regions. We perform 950 MD simulations of thermal systems and find random thermal fluctuations can influence structural stability and provide a means to switch between different swarms.

4.3.1 3D swarms

We observe the morphology of 3D Morse swarms depends upon the shape of the interaction potential, as has been demonstrated in detail for 2D systems [47, 59, 103, 61]. We perform 10 independent simulations at each of 400 different combinations of two reduced interacting potential parameters $l = \frac{l_r}{l_a}$ and $C = \frac{C_r}{C_a}$, with $l_r = 1$, $C_r = 1$, and $T^* = 0$. Henceforth when we specify values of C or l without specifying C_a or l_a, we take $C_a = 1$ and $l_a = 1$. Simulations are initialized with $N = 600$ particles randomly distributed in a 5σ cubic region with random velocities, within a 20σ simulation box with periodic boundary conditions. For most values of l and C in the range $0.1 \leq l \leq 2.0$ and $0.1 \leq C \leq 2.0$ we observe one of six distinguishable swarms: balls, shells, rings, spherical clumps, cylindrical clumps, and tori (Fig. 4.1). We summarize the relationship between observed swarm morphologies

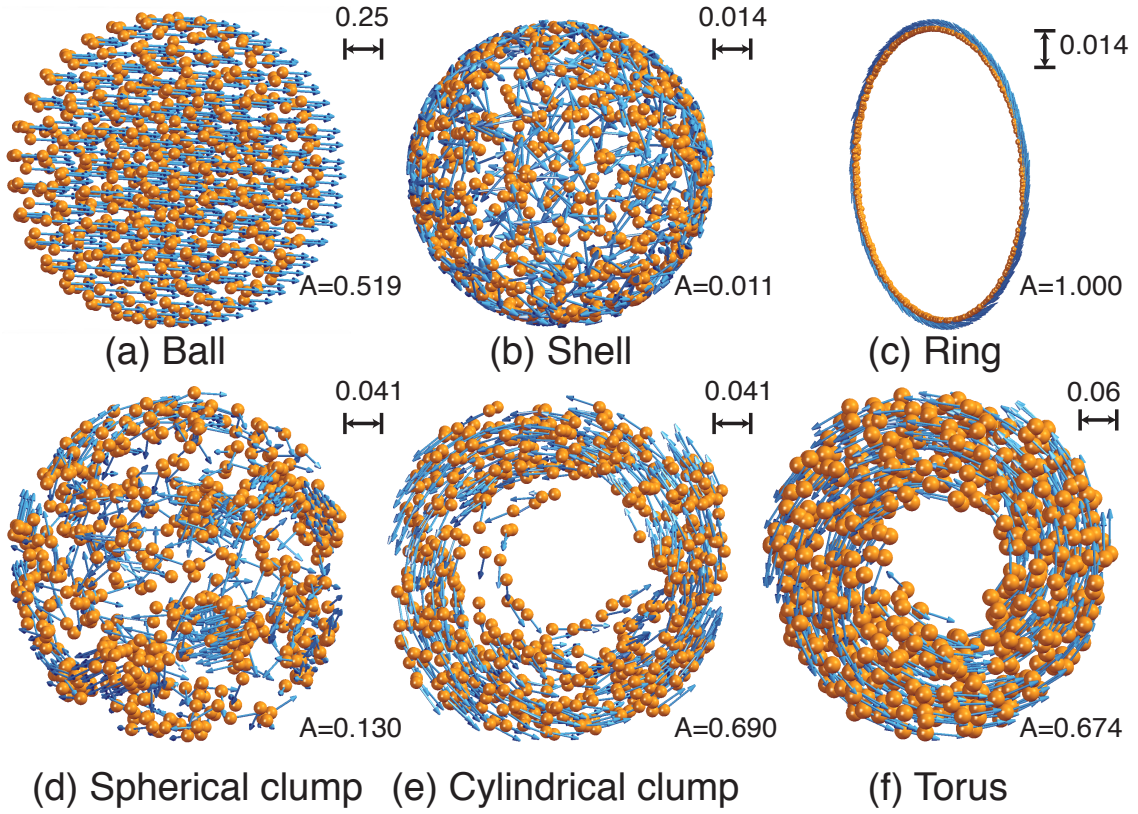

Figure 4.1 Three-dimensional self-propelled swarms of $N = 600$ Morse particles at $T^* = 0$, $\alpha = 2$, $\gamma = 1$, and $\beta = 0.5$. Steady state swarms are observed in MD simulations after 2×10^6 time steps have evolved for particles within a 20σ simulation box with periodic boundary conditions. Particles are initialized with random velocities and are randomly distributed within a 5σ cubic region inside the simulation box. Blue arrows indicate particle velocities. Orange spheres represent particle positions, but the sphere diameters to not correspond to particle size. Scale bars are shown in the upper right and alignment order A is shown in the lower left of each swarm. Swarm radii range from 0.06σ to 0.3σ (ball). (a) Ball ($C = 1.5$, $l = 0.5$) composed of concentric spherical layers of particles and identical velocities. (b) Stationary hollow shell ($C = 0.5$, $l = 0.5$) composed of particles that travel in circular orbits. (c) Stationary ring ($C = 0.5$, $l = 0.5$) with all particles traveling in the same circular orbit. (d) Stationary spherical swarm ($C = 0.6$, $l = 0.5$) with clumps of particles that travel in circular orbits. (e) Stationary cylindrical swarm ($C = 0.6$, $l = 0.5$) composed of clumps of particles traveling about the same circular orbit. The particles within the clumps move in a cylindrical fashion, but follow a complex path such that the cross-sectional shape of the cylinder appears to be time dependent. (f) Torus ($C = 0.6$, $l = 0.3$) composed of particles that travel in circular orbits of different radii, but share an axis of rotation. Particle paths within the torus span the entire volume: a particle that is near the hole eventually moves to the outer part and back again. See Supplemental Material videos 1-6 for movies of these swarms.

and Morse potential parameters in Fig. 4.2. There are three primary types of observations summarized in the phase diagram; regions where one swarm always self-assembles, regions where two swarms coexist (*e.g.*, "Torus-Ball" and "Shell-Ring"), and regions where no coherent swarms emerge ("Mixture" and "Random" in Fig. 4.2). In the Random region the repulsion portion of the Morse potential dominates, precluding swarm coalescence. In the Mixture region there is an energy barrier to particle agglomeration, but occasionally small ($N = 2$ to $N = 10$) translating clusters appear. From Ref. [21].

A large portion of Fig. 4.2 is represented by the ball structure (Fig. 4.1a). The ball structure is only found for potentials that are repulsive when particle separation is small and attractive when separation is large, similar to the Lennard-Jones potential. All particles in a steady-state ball travel with an identical linear trajectory with speed $\bar{v}_B = 2.0 \pm 0.0$. The structure of the particles within the ball, concentric spherical shells, is a minimum for the potential energy function 4.1. Another significant portion of Fig. 4.2 is represented by the shell swarm (Fig. 4.1b). The shell swarm is hollow, with individual particles traveling in circular paths on the surface of a sphere and with no correlation between particle orbits. Shells are formed when the attraction between particles is large, and have average velocity $\bar{v}_S = 1.993 \pm 0.003$. Between the shell and ball regions of Fig. 4.2 we finds regions where rings (Fig. 4.1c), clumps (Fig. 4.1d,e), and tori (Fig. 4.1f) are observed. Rings have average velocity $\bar{v}_R = 1.994 \pm 0.003$, and differ from shells in that all of the particles share an axis of rotation. Tori ($\bar{v}_T = 1.89 \pm 0.410$) differ from rings in that not all particles travel in a circular orbit of the same radius. Cylindrical clumps ($\bar{v}_{CC} = 1.96 \pm 0.28$) are similar to tori, but particles are clumped and not uniformly distributed as they are in the torus. Spherical clumps ($\bar{v}_{SC} = 1.93 \pm 0.36$) are similar to shells in that all particles travel in circular orbits of the same radius, but the particles are not uniformly distributed. The average velocities we report above correspond to the state points indicated in Fig. 4.1 and, except for the ball swarms, can differ slightly for different state points.

The 3D phase diagram we report in Fig. 4.2 is qualitatively similar to the 2D phase

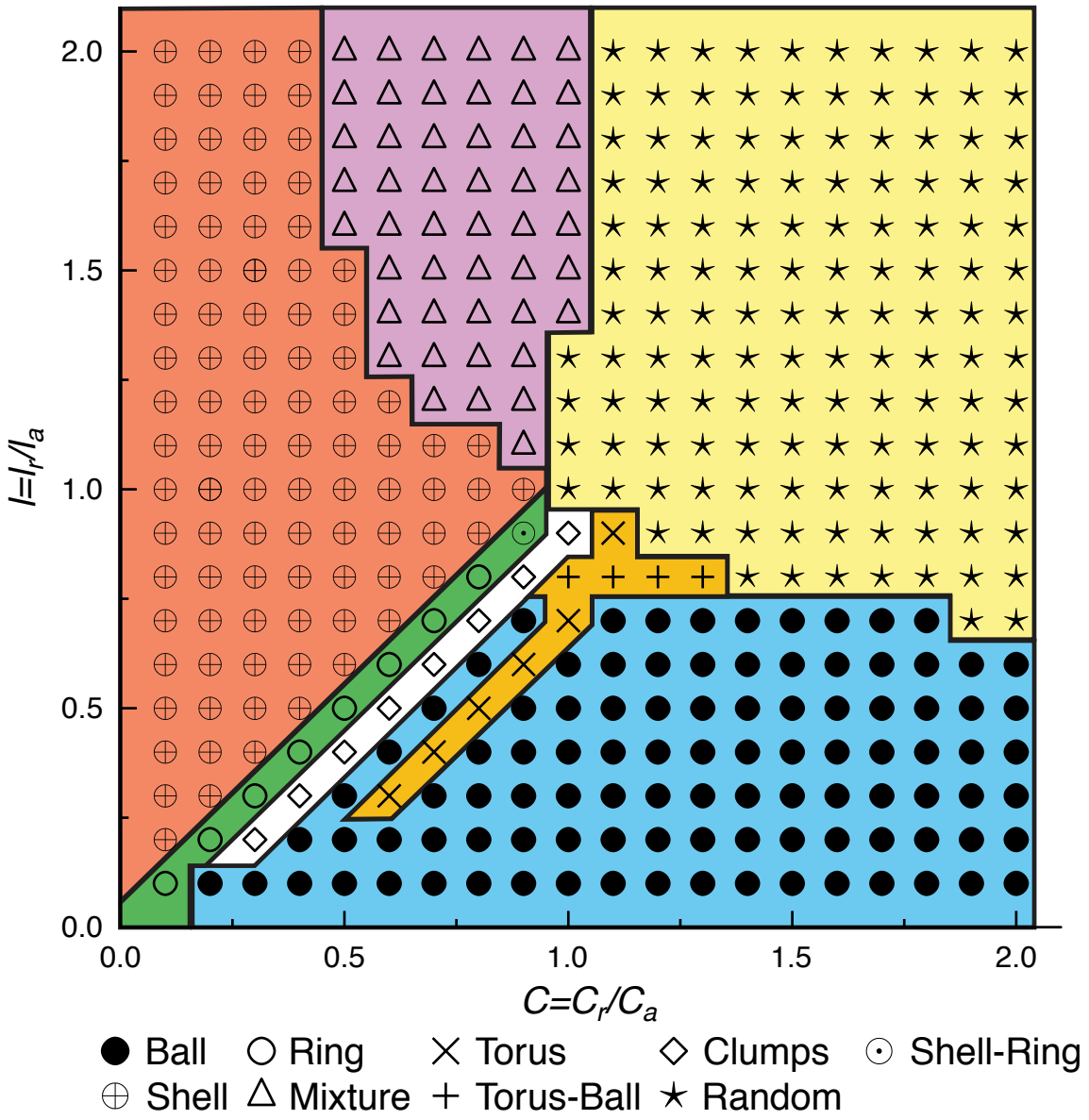

Figure 4.2 "Phase diagram" for 3D stable structures assembled at values of $0.1 \leq l \leq 2.0$ and $0.1 \leq C \leq 2.0$, $T^* = 0$, $\alpha = 2$, $\gamma = 1$, and $\beta = 0.5$. The ratio of repulsion to attraction strength $C = \frac{C_r}{C_a}$ and the ratio of repulsion to attraction length scales $l = \frac{l_r}{l_a}$ determine the shape of the interaction potential and the swarms observed at steady state. In the upper right quadrant ($l > 1, C > 1$) repulsion dominates the potential, preventing organized clusters from assembling. In the lower right quadrant ($l < 1, C > 1$) the repulsion is short-ranged and the attraction is long-ranged, resulting in translating spherical balls. In the lower left quadrant ($l < 1, C < 1$) attraction dominates the potential and the phase diagram is most complex, with shells, rings, tori, balls, and clumps all stabilized within narrow ranges of l and C. In the top left quadrant ($l > 1, C < 1$) particles are attractive, but the repulsive length scale dominates, giving rise to hollow shells.From Ref. [21].

diagram calculated analytically in D'Orsogna *et al.*[59]. Both phase diagrams have regions of instability in the upper right quadrant and show the richest swarm diversity along the $l/C = 1$ line. We check our implementation reproduces 2D results from Ref. [59] and find the expected swarms at corresponding state points: Clumps ($N = 100$, $\alpha = 1.0$, $\beta = 0.5$, $l_r = 0.5$, $l_a = 1$, $C_r = 0.6$, $C_a = 1$), ring clumping ($N = 100$, $\alpha = 1.0$, $\beta = 0.5$, $l_r = 0.5$, $l_a = 1.2$, $C_r = 0.6$, $C_a = 1$), rings ($N = 100$, $\alpha = 1.0$, $\beta = 0.5$, $l_r = 0.5$, $l_a = 1$, $C_r = 0.5$, $C_a = 1$), and vortexes ($N = 300$, $\alpha = 1.0$, $\beta = 0.5$, $l_r = 0.5$, $l_a = 2$, $C_r = 1.0$, $C_a = 0.5$). Some of the structures we report here are analogues of the two-dimensional swarms predicted in Ref. [47, 59, 103, 61]. The 3D ball is similar to the 2D coherent flock state reported in Ref. [61], in which particles travel at identical velocities and reside in their potential minima. The 3D hollow spherical shell corresponds to the 2D ring [47, 59, 103, 61], and the 3D spherical clumps are analogous to the circular swarm of clumps in 2D [59, 61].

We also observe some differences between our 3D swarms and Morse swarms reported in other work. At $C = 1$ and $l = 0.2$, conditions where a vortex is formed in 2D, we expect to observe its 3D analogue, the torus. In our MD simulations we observe the torus as an initial transient, but find that it eventually transforms into a ball. When not confined to a 2D plane, particles are able to reconfigure into a potential energy minimizing sphere and achieve v^* simultaneously at this state point. These findings are consistent with Strefler *et al.*[62], where transitions between torus and ball swarms are reported when the Morse potential is tuned to have a repulsion at small r_{ij}.

It is not obvious that we should observe 2D rings in our 3D simulations and that they should be stable across many (l,C) values, as seen in Fig. 4.2. We observe coexistence of shells and rings at $l = 0.9$ and $C = 0.9$, which is interesting because swarm coexistence is not reported in previous Morse swarm work. In a departure from equilibrium statistical mechanics, we find that in the regions of swarm coexistence the probability of forming one swarm can be biased by choice of initial conditions, which we discuss in detail in the following section.

4.3.2 Initial conditions

Here we consider three points on the phase diagram and investigate ways in which initial conditions can be chosen to bias swarm formation. First we show that although swarms may not assemble spontaneously in the Random region of Fig. 4.2, a pre-assembled swarm can be maintained there. Second we show in a region of torus-ball coexistence that swarm formation is not sensitive to initial conditions. Third, we show that while either initial velocity correlations or initial spatial arrangement can bias swarm formation at the shell-ring coexistence point ($l = 0.5, C = 0.5$), a metric that combines these measurements (alignment order A, Eq. 4.7) is a good predictor for the final steady state.

At $l = 1.7$ and $C = 1.2$ we observe no ordered structure assembling from particles initialized randomly within a 5σ cubic region centered within a 20σ simulation box with periodic boundary conditions. If we instead initialize particles as a small shell that fits within the attraction region of the potential, we observe that the shell shrinks or expands, depending on its initial size, to another shell that becomes stable for the remainder of 1×10^6 time step simulations. The necessary condition for shell formation is that particles are initialized within the attraction region and have sufficiently low kinetic energy that they will not escape to the repulsive regime of the Morse potential. Indeed, we also find shells stabilized in the Random region by initializing particles on a single point with random initial velocities. By initializing the system as a shell, we find shells are stable within the region ($l = 1.7$, $C \leq 1.5$), which spans the Mixture region as well as the Random region.

Next we consider $l = 0.8$ and $C = 1.0$, where the ball and torus coexist in our simulations. We perform simulations initialized as a ball, as a cylinder, and randomly distributed within a 5σ cube, with 100 independent runs with different random initial velocities. At these parameters, we find the probability of observing a toroidal swarm to be 6% for all three initial conditions. In all cases that the torus does not form, a spherical ball forms instead and translates through the simulation box.

Finally, we consider ring and shell coexistence at $l = 0.5$ and $C = 0.5$. We note that

whenever we observe a ring, we also observe that it is preceded by a hollow shell which then transforms into a ring. The shell-to-ring transition occurs over 4×10^4 time steps, and can occur as many as 4×10^4 time steps after the shell has self-assembled. We perform simulations in which particle positions are initialized as a shell, sphere, cylinder, and randomly distributed within a 5σ cube to investigate sensitivity to initial conditions at this state point. For each initial condition we perform 100 runs with random initial velocities and record the structure observed after 1×10^6 time steps (Fig. 4.3). When initialized as a shell, only 2% of swarms transition into rings, a substantially lower percentage than the 98% of swarms that form rings from spatially randomized initial conditions, all of which pass through a hollow shell transition state. For each of the 100 runs initialized as a cylinder, all transition into rings. For the runs initialized as balls, 12% transition into rings.

The sensitivity of swarm morphology to initial conditions we report is similar to that reported in Ref. [18], in which magnetic, millimeter-sized disks are driven by an external rotating permanent magnet to self-assemble ordered patterns on a liquid-air interface. A variety of ordered patterns are formed as a result of competing magnetic attraction and hydrodynamics repulsion as the disks spin in the fluid. The authors demonstrate that, depending on initial conditions, a system of one large and nine small disks self-assembles into two different stable configurations. Another similarity between our ring-shell coexistence and the swarm coexistence in Ref. [18] is that swarm size can be increased as self-propulsion is increased. In the system of 10 equally-sized disks from Ref. [18], two different ordered patterns can self-assemble and interconvert. While we observe transitions from shells to rings, we never observe the reverse transition. The one-way conversion we observe is interesting because the ring has neither a lower potential energy nor higher entropy than the shell, though the particles are traveling at slightly more constant velocities. The smaller energy dissipation in the ring associated with more constant velocities is consistent with the hypothesis of Grzybowski *et al.* [18] where lower dissipation enhances swarm stability.

We find as a shell transforms into a ring the axes of rotation for the individual particles

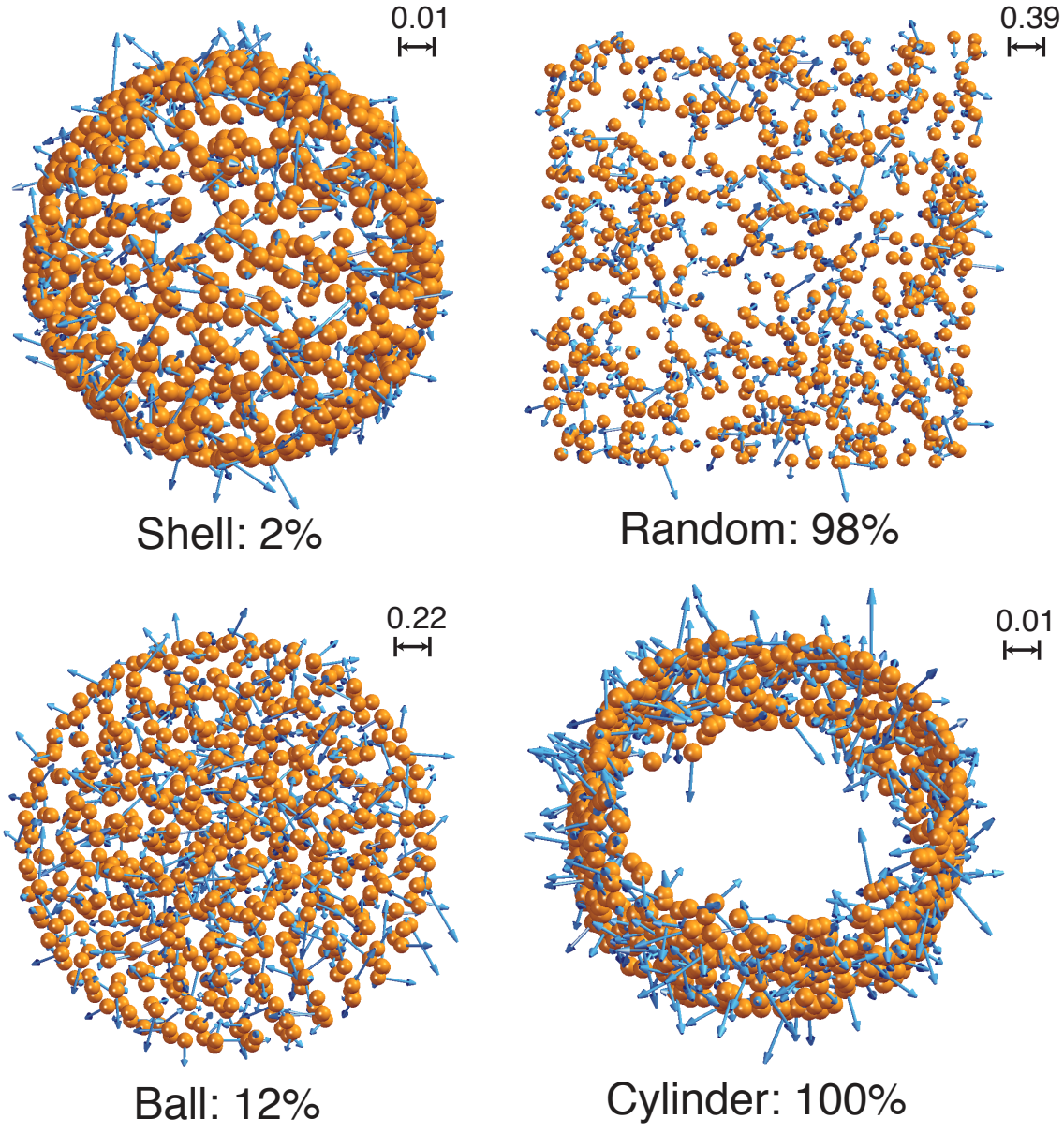

Figure 4.3 Four initial conditions and their probabilities of transitioning to a ring. The shell and cylinder initial conditions have radii of 0.062. The ball has a radius of 1.35 and the random configuration is distributed randomly in cubic box with side length of 5. Ring transition probabilities are calculated from 100 independent runs performed for each of the indicated initial condition with $T^* = 0$, $\alpha = 1$, $\gamma = 1$, $\beta = 0.5$, $C_r = 0.5$, $l_r = 0.5$, $C_a = 1$, $l_a = 1$, and $N = 600$ with random initial velocities.From Ref. [21].

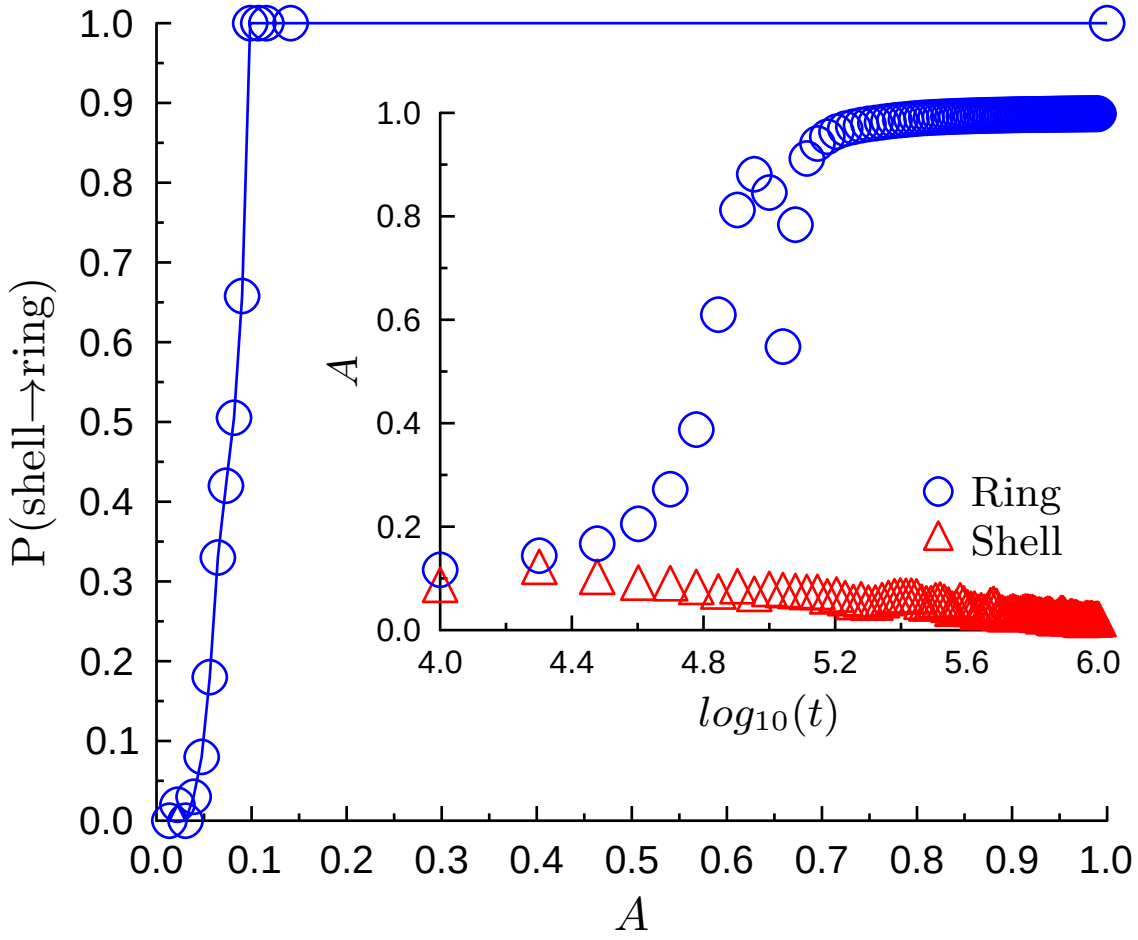

Figure 4.4 Probability of a random shell transforming into a ring as a function of alignment order A (Eq. 4.7) at $T^* = 0$, $\alpha = 1$, $\gamma = 1$, $\beta = 0.5$, $C_r = 0.5$, $l_r = 0.5$, $C_a = 1$, $l_a = 1$, and $N = 600$. The blue line is drawn as a guide to the eye. Inset are representative alignment order trajectories for swarms that form a shell (red) and ring (blue).From Ref. [21].

gradually align, resulting in cylindrical bands, the subsequent alignment of which results in a ring. See Supplemental Material video 3 to view this transition. To investigate the alignment of angular momenta further, we initialize 1000 random shells with random initial velocities and run for 1×10^6 time steps. We record the initial alignment order A and the final steady state swarm, and summarize the correlation between the two in Fig. 4.4. The more the particle angular momenta are initially aligned, the higher the probability that the shell would transform to a ring. In particular, Fig. 4.4 shows that if a shell experiences an instantaneous A greater than 0.15 we would expect it to transition into a ring.

We perform additional simulations with three different spatial initializations and two

velocity distributions and observe the initial A trajectories in detail. Simulations are initialized as the random, ball, or shell arrangements from Fig. 4.3 with either a random Gaussian velocities of mean 2 and standard deviation 1, or velocities drawn from a ring swarm (velocities parallel with mean 1.994 and standard deviation 0.003). We then run 10 independent 0.5-million-step simulations for each of the six cases and record the number of rings formed. The average A over initial 1×10^4 step trajectories for these six cases are shown in Fig. 4.5. We see here that the combined choice of spatial arrangement and velocity distribution determine the initial A trajectory, which can predispose a swarm to give rise to a ring vs. a shell. In all cases where the A trajectory has a positive slope after 2000 steps, A increases past 0.15 and rings result. If the initial A trajectory is sufficiently low, as was the case for one random initial condition initialized with velocities from a ring, the A trajectory can begin above 0.15, but dip below and stay below, resulting in a shell. The three instances of Ball initial conditions with random velocities resulting in a ring have slightly positive A slopes that eventually cross $A = 0.15$ after a few hundred-thousand steps.

In summary, the sensitivity of steady state swarm morphology to initial conditions is not uniform across the state space sampled in Fig. 4.2. In some regions we find swarm formation to be robust to initial conditions, while in others we find both spatial correlations and velocity correlations can have an impact on the rates of swarm formation. For the case of the shell-ring coexistence in particular we find that alignment order A, a metric that combines velocity and spatial correlations in its measurement of angular momentum correlations, provides predictive capabilities between the two competing swarms. The combined choice of initial positions and velocities determine whether A shall increase or decrease initially, and whether this trajectory stabilizes above or below 0.15 determines the proportion of rings observed. In regions where we observe sensitivity to initial conditions, we also expect to observe sensitivity to random noise, which we explore in the next section.

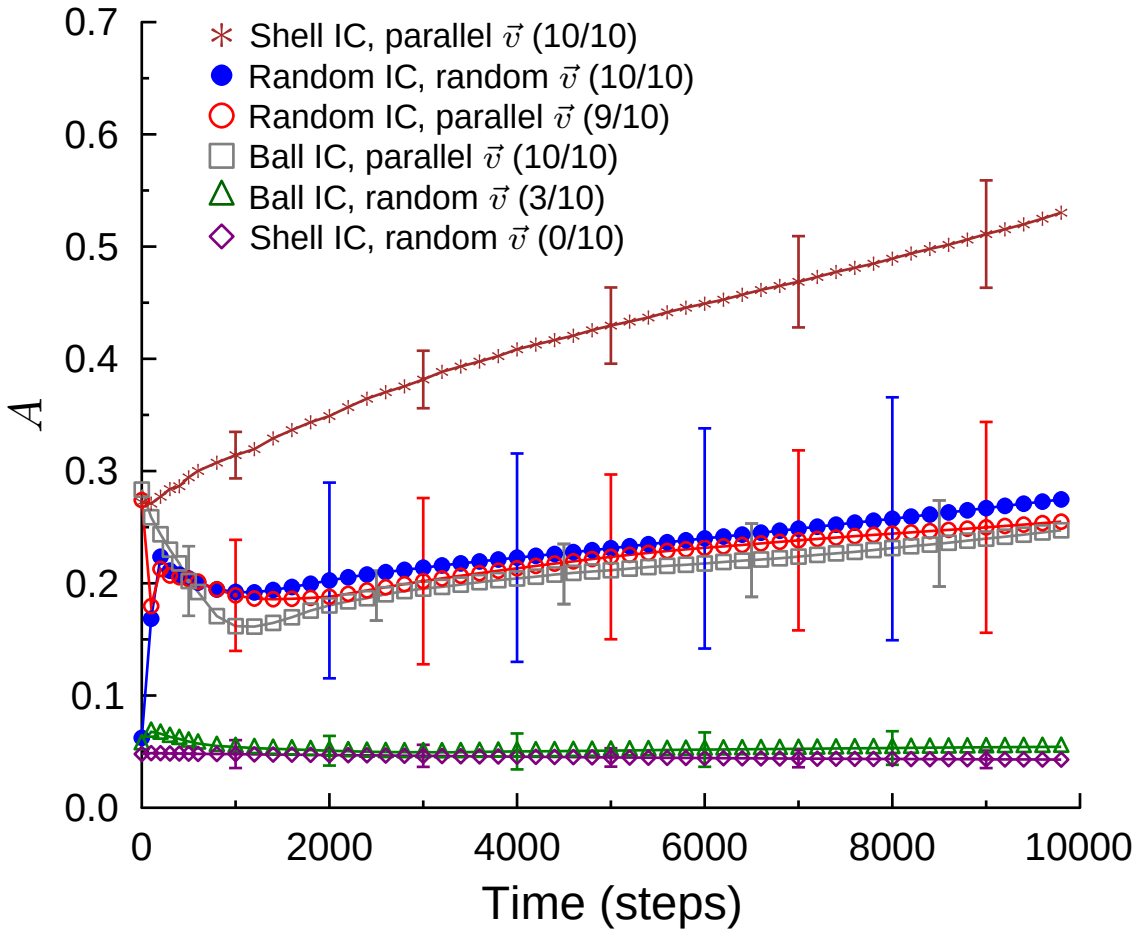

Figure 4.5 Initial time evolution of the alignment order A averaged over 10 independent runs for six different combinations of initial arrangements and initial velocities. The particles are spatially initialized either randomly within a 5σ cube, within a 2.7σ ball, or on a 0.062σ shell within a 20σ cubic simulation box with periodic boundary conditions. Velocities are initialized from a Gaussian distribution with mean 2 and standard deviation 1 (random $\vec{v}$) or drawn from the ring velocity distribution with mean 2, standard deviation 0.15, and z-component = 0 (parallel $\vec{v}$). The number of observed rings after 1×10^6 time steps are shown in parentheses. Error bars are plotted every 2000 steps and denote one standard deviation.

4.3.3 Noise

In this subsection we perform simulations at $T^* > 0$ to investigate how thermal fluctuations can influence the formation of swarms. We find in general that for $T^* > 0.20$ the attractive forces between particles are not large enough to stabilize ordered swarms anywhere in the (l, C) range reported in Fig. 4.2. The highest temperature at which a swarm can be assembled at a particular state point (the order-disorder transition temperature) depends upon the shape of the interaction potential and the initial conditions for self-propelled particles, and is an interesting area of future study. Here we focus on the torus/ball and ring/shell coexistence regions and find that increasing temperature stabilizes one swarm over the other, as long as T^* is below the order-disorder transition temperature.

At $C_r = 0.9$, $l_r = 0.6$, $C_a = 1$, and $l_a = 1$, a parameter combination at which tori are found, increasing temperature can transform a torus swarm into a swarm shaped like a bumpy sphere. We begin with a pre-assembled $N = 600$ torus and gradually increase the noise intensity from 0 to 0.08 and then reduce the intensity back to zero with a change of $\delta T^* = 0.01$ every 1 million time steps. We find that when $T^* > 0.03$ the torus transforms into a bumpy sphere, which translates randomly throughout the simulation box. As the noise intensity is reduced to zero, the bumpy sphere transitions back to a torus. This noise-induced transition from stationary swarm to mobile swarm and back again is qualitatively similar to the transition reported in Strefler *et al.* [62]. As in Ref. [62] we find the velocity of the translating bumpy sphere scales with T^*. Our observations of torus stability differ slightly from those of Strefler *et al.*, where stable tori are found at $C_r = C_a = l_r = 0.5$, $l_a = 2$, and $T^* = 0$. At that state point we find the torus always transitions into a ball after 4×10^5 steps.

To investigate the sensitivity of ring/shell formation to thermal fluctuations we perform 100 independent MD simulations at each temperature from $T^* = 0$ to $T^* = 0.008$ at increments of $\delta T^* = 0.001$. Here, $\alpha = 2$, $\gamma = 1$, $\beta = 0.5$, $l = 0.5$, and $C = 0.5$. Particles are initialized randomly within a 5σ cubic region within the 20σ simulation box with periodic

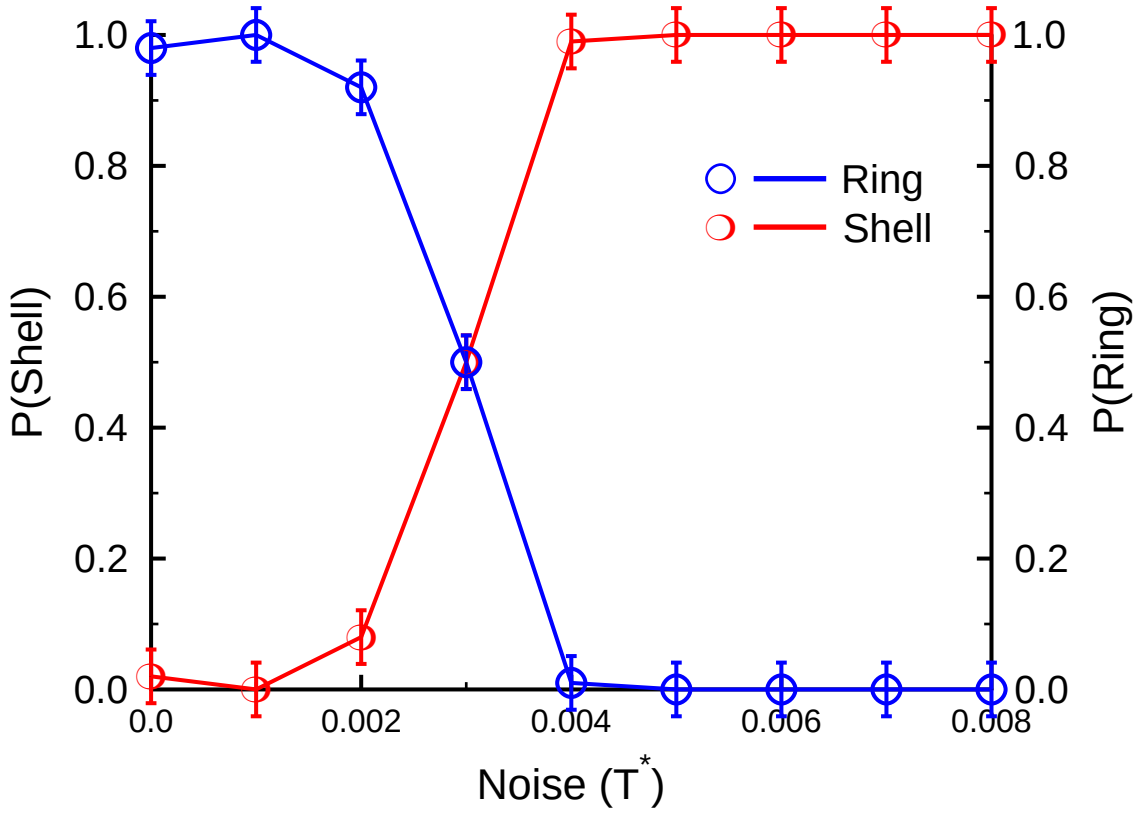

Figure 4.6 Probability of shell (red) and ring (blue) formation as a function of T^* at $\alpha = 2$, $\gamma = 1$, $\beta = 0.5$, $C_r = 0.5$, $l_r = 0.5$, $C_a = 1$, $l_a = 1$, and $N = 600$. 100 independent runs are performed at each noise level, with particles initially randomized in a 5σ cube within a 20σ cubic simulation box and are evolved for 1×10^6 time steps. Error bars denote one standard deviation.From Ref. [21].

boundary conditions and simulated for 1×10^6 time steps. We find that the probability of assembling a ring decreases as T^* increases (Fig. 4.6), undergoing a sharp transition at $T^* = 0.003$, above which shell self-assembly is enhanced.

We also observe the rings formed at $T^* > 0$ are no longer flat, but cylindrical. We perform additional simulations initialized from a ring configuration and ramp temperature from $T^* = 0$ to $T^* = 0.008$ by a step increase in temperature of $\delta T^* = 0.001$ every 1×10^6 time steps, followed by a reverse ramping back to $T^* = 0$, for a total of 16×10^6 time steps. We perform these simulations for swarms of size $N = 100$, $N = 200$, $N = 400$, and $N = 600$ and find that cylinder height increases linearly with T^* from $T^* = 0.001$ to $T^* = 0.007$ (Fig. 4.7). Furthermore, we find that by normalizing the cylinder height by the cylinder diameter, this trend is independent of swarm size (Fig. 4.7). When $T^* > 0.007$, cylinders

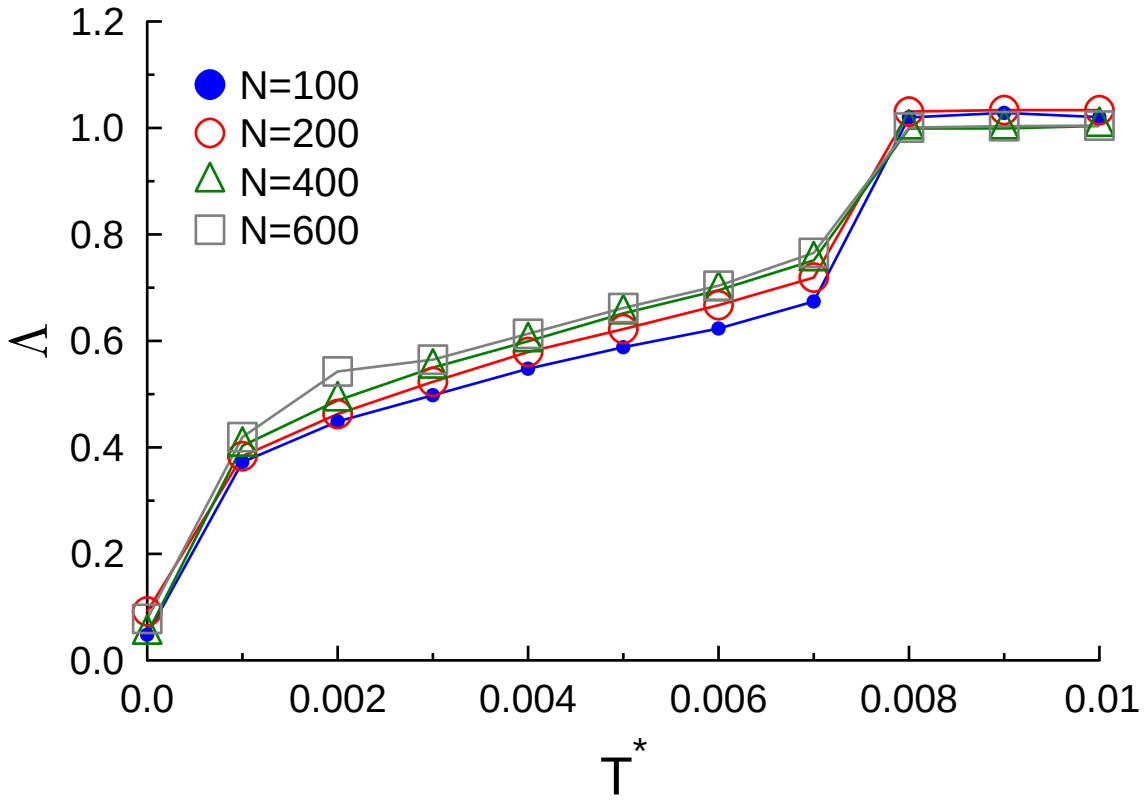

Figure 4.7 Normalized cylinder height Λ as a function of dimensionless temperature T^* and number of particles N. Particles are initialized as a ring with random velocities. $\alpha = 2$, $\gamma = 1$, $\beta = 0.5$, $C_r = 0.5$, $l_r = 0.5$, $C_a = 1$, and $l_a = 1$. Λ are averaged over 10 simulation snapshots and over 10 independent simulation runs, where the snapshots are the last 10 at 1×10^4time step increments. The standard deviations of Λ are less than 3% of the mean values and are not shown.From Ref. [21].

transition into hollow shells. This transition can be used as part of a reversible sequence of steps to convert rings into cylinders into shells and back into rings (Fig. 4.8). We find that by dropping the temperature from $T^* = 0.008$ to $T^* < 0.007$, a shell will transform into a ring or cylinder (depending on the temperature) if its instantaneous alignment order A is sufficiently large (Fig. 4.4).

4.4 Driving forces

Swarm formation in self-propelled particles can be considered as a perturbation to equilibrium self-assembly. In the limit that $\alpha \to 0$ and $\beta \to 0$, Eq. 4.2 becomes the traditional

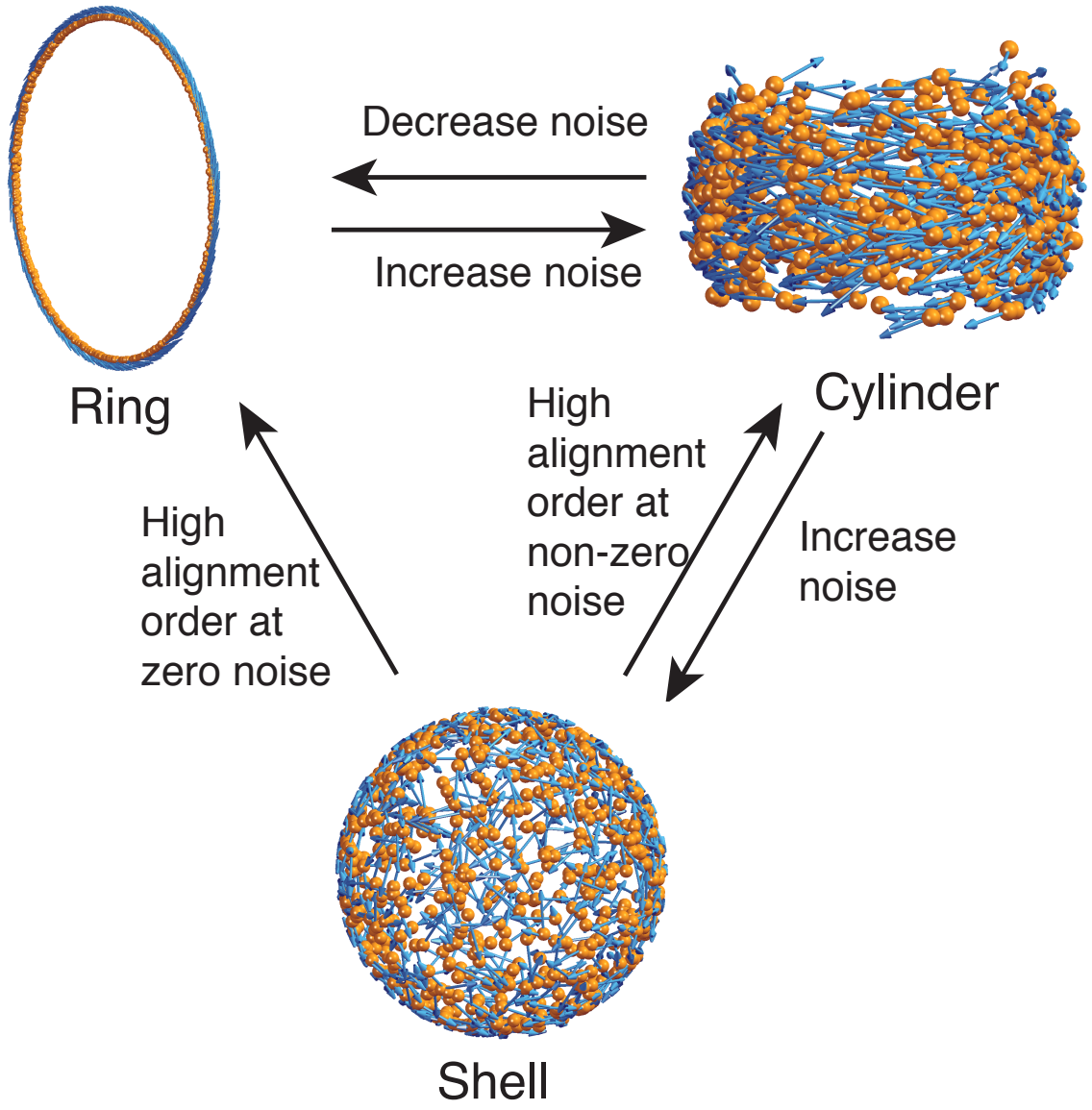

Figure 4.8 Mechanisms of structural transitions among shells, rings, and cylinders. Increasing the temperature of a ring causes it to transition into a cylinder of increasing height. At large enough T^*, cylinders transition into hollow shells. The transformation of a hollow shell into a cylinder or ring requires not only that the temperature be decreased below $T^* = 0.007$, but also that an instantaneous fluctuation in alignment order is sufficiently large to initiate the transition. The transition involves the shell polarizing into cylindrical bands, which align eventually turning into a cylinder with noise-dependent height or a ring if the noise is zero.From Ref. [21].

Langevin equation modeling Brownian motion, from which equilibrium distributions of configurations can easily be sampled. From the systems studied here with nonzero α and β, we observe the formation of swarms over a wide range of Morse potential shapes, but for which the variational principle controlling structure formation is not simply minimization of a traditional (e.g. Helmholtz) free energy. In fact, the question of what general variational principles governing the behaviors of driven systems is a challenging and unanswered one [26]. Here we discuss how the swarms studied in this work are both similar to and different from structures formed via equilibrium self-assembly as a possible step towards answering this question.

The two most relevant driving forces for steady-state swarm formation are the balance of conservative forces between neighboring particles and the simultaneous achievement of the optimal velocity. All of the swarms we observe are comprised of particles traveling at, or nearly at, v^*. In the case of ball swarms, these driving forces are relatively decoupled, with a potential energy minimizing structure that is stationary in reference frame moving at v^*. In the case of ring, shell, clumps, and tori the two driving forces are not so cleanly decoupled, and particles in these swarms have velocities that vary over time with averages near v^*. For these swarms with stationary centers of mass, the centripetal forces from particle rotation are balanced by the conservative forces between particles. It is straightforward to predict the size of the shell and ring swarms by equating these forces.

If these structures were emerging in non-dissipative equilibrium systems we would expect structures with lower free energy (lower potential energy and higher entropy) to be more stable. Energetically, the ring and shell have nearly identical potential energy ($U_{ring} = -88010.46$, $U_{shell} = -88012.56$). Entropically, there are more ways to arrange particles on a shell than there are ways to arrange particles around a ring of the same diameter. Considering only the free energy of a swarm we would expect shells to be more stable than rings, which is inconsistent with our observation that rings never transform into shells. Perhaps there exists an "extended" free energy that can be written for self-propelled swarms

that provides predictive capabilities. Previous work by Schweitzer *et al.*[102] provides a promising direction for such a development. The free energy would be extended in the sense that it adds additional non-equilibrium driving forces to a well-known equilibrium ensemble free energy. For the systems we study here, it seems natural that this extended free energy should include α, β, and γ, as these parameters provide the deviation from a standard equilibrium simulation. Because these terms describe the work put into the swarms and the dissipation of energy to the surrounding bath it follows that the free energy extension should incorporate dissipation.

Derivations for the functional form and demonstration of such an extended free energy are beyond the scope of the current work, but are an exciting challenge with important implications for theories of non-equilibrium self-assembly. Regions of parameter space in which structures coexist provide test-cases for points at which extended free energies should equate, therefore models such as the propelled Morse particles studied here are ideal candidates for theory development. The co-existing states in experimental systems such as in Ref. [18] can be used to compare and validate the theory.

4.5 Conclusions

We have performed extensive GPU-enabled simulations of self-propelled swarming particles, characterizing the structures that can be assembled over a wide range of parameters that tune the Morse interaction potential in three spatial dimensions. The diversity of the swarms stabilized in this system, their coexistence regions, and their sensitivity to thermal fluctuations (noise) highlights the need for efficient computer simulations with which parameter space can be explored and detailed experiments performed. We observe behaviors that are marked deviations from equilibrium self-assembly, including swarm coexistence and sensitivity to initial conditions, but our results suggest that modifications to equilibrium statistical mechanics approaches may have predictive capabilities. We propose a way forward, combining the

swarms found in regions of coexistence as test cases for extended free energy development. Finally, the diversity of structures we observe here and the demonstrated control over their morphology may have immediate implications in the exploitation of swarms of practical interest.

Chapter 5
Self-assembly of Self-Rotated Particles

5.1 Introduction

Active matter is a rapidly growing branch of non-equilibrium soft matter physics with relevance to fields such as biology, energy, and complex systems [45]. In active matter, dissipative, steady-state structures far-from-equilibrium can emerge in systems of particles by converting energy to particle motility [44, 45]. Recent works reported novel collective behavior, not possible with passive matter, such as giant number fluctuations [46], clustering [14], swarming [59, 21], fluid-solid phase separation of repulsive disks [110, 63, 15], and collective rotors [111]. Effective interactions emerging between hard, self-propelled particles were shown to cause phase separation and coexistence [112, 113, 63, 114, 115]. Experimentally, some of these phenomena were demonstrated by driving the system via vibration [17, 116, 117], chemical reaction [85, 84], diffusiophoresis [115], and light activated propulsion [16]. To date, most studies have focused on self-propulsion where the constant input of energy to each particle goes directly into translational motion and hence active forces couple to particle velocities. Converting the input of energy into *rotational* motion, however, does not directly influence translational motility, and couples only to the particles' angular momentum. We denote such a coupling of active driving forces to angular velocity as *active rotation*.

Active rotation may be achieved by various methods, *e.g.* external magnetic fields [18, 118, 19] and optical tweezers [119, 120, 121]. Biological organisms, such as dancing

algae [122] and clusters of sperm cells [123], can spin naturally. Certain self-propelled anisotropic shapes exhibit circular motion [111, 124]. Rotating particles submersed in a fluid experience hydrodynamic interactions that can be attractive or repulsive through the formation of vortices [18, 118, 125]. Collective phenomena involve synchronisaton and

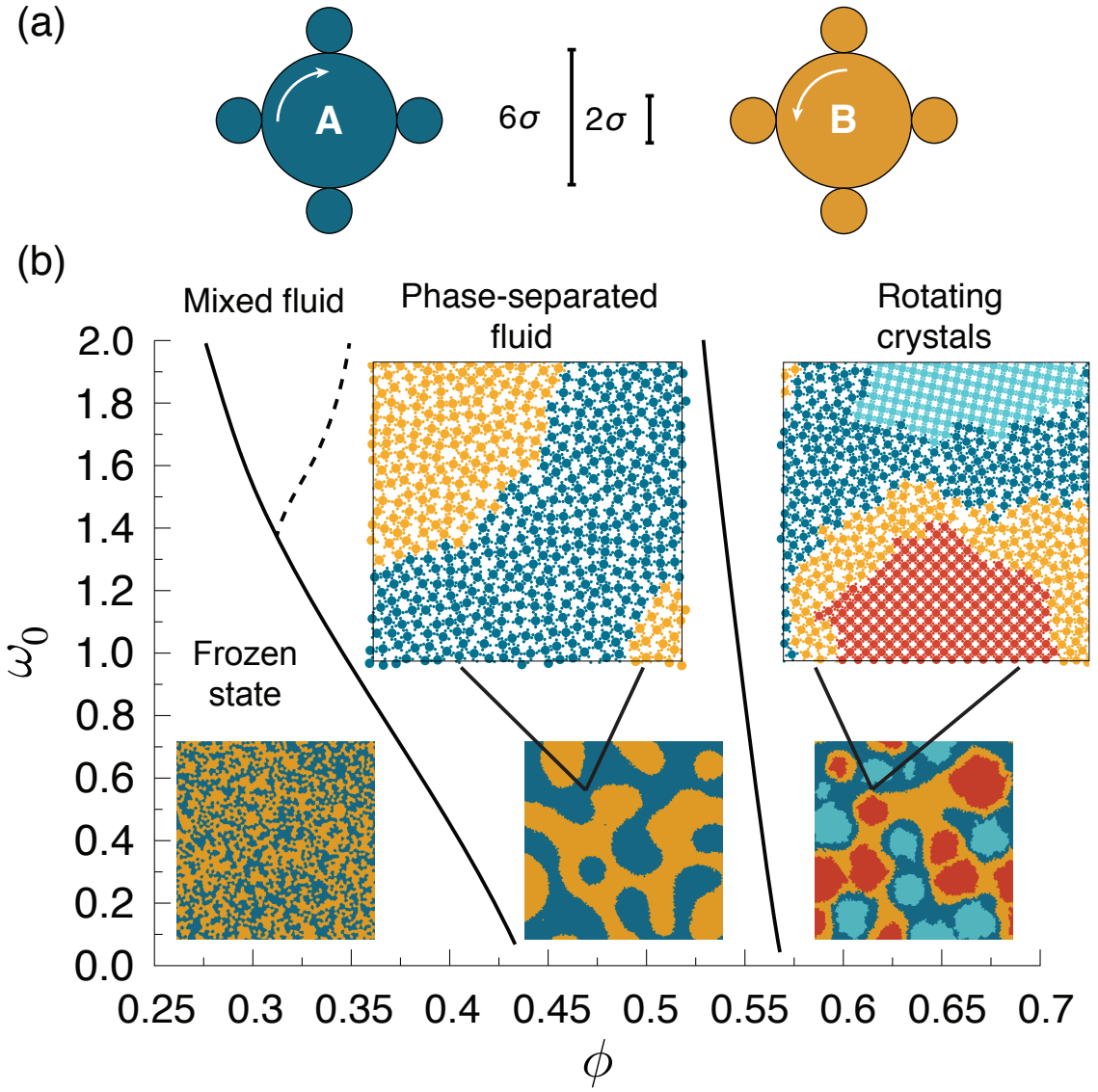

Figure 5.1 (a) Clockwise ('*A*') and counterclockwise ('*B*') spinners. (b) The ratio of translational to total kinetic energy κ indicates the presence of a phase transition ($\omega_0 = 1$). Error bars are smaller than the symbols. The inset shows the critical density ϕ_c as a function of noise T^*. (c) Non-equilibrium phase diagram based on simulation data [22] at $T^* = 0$. Lines indicate phase boundaries. Insets show representative snapshots as the system approaches steady state. A and B spinners in the fluid (crystal) phase are shown in dark (light) blue and orange (red) colors. 50:50 mixtures are used in (b,c). From Ref. [23].

self-proliferating waves [126], and vortex arrays [127]. Beyond these examples, however, the potential use of active rotation for pattern formation and self-organization in driven systems is only starting to be investigated systematically. In this Letter, we show with computer simulations that effective interactions emerge between spinners rotating in the same direction, and between oppositely rotating spinners, due to the active motion itself. The result is phase separation, rotating crystals, cooperative and heterogeneous dynamics leading to superdiffusive motion, and complex phase behavior. The contents of this Chapter are being published and on the arXiv [23].

5.2 Model and methods

Our spinner particle is modeled by four peripheral disks of radius σ rigidly attached to a central disk of radius 3σ at each of the compass points, Fig. **??**(a). The system is governed by a set of coupled Langevin equations for translation and rotation,

$$M\frac{\partial \vec{v}_i}{\partial t} = \vec{F}_i - \gamma_t \vec{v}_i + \vec{F}_i^R, \tag{5.1}$$

$$I\frac{\partial \omega_i}{\partial t} = \tau_i^D + \tau_i - \gamma_r \omega_i + \tau_i^R, \tag{5.2}$$

where M, I, $\vec{v}_i$, and ω_i have the usual meanings of mass, moment of inertia, and translational and angular velocity. Each spinner is driven by an external torque $\tau_i^D = \pm\tau^D$ of constant magnitude, but with positive sign for clockwise spinners ('A') and negative sign for counterclockwise spinners ('B'). Spinners are hard particles that interact via a purely repulsive contact potential, resulting in internal forces $\vec{F}_i$ and torques τ_i. Energy is dissipated through translational and rotational drag coefficients γ_t and γ_r. Noise is included via random forces $\vec{F}_i^R = \sqrt{2\gamma_t kT_0}R(t)$ and torques $\tau_i^R = \sqrt{2\gamma_r kT_0}R(t)$ that model a heat bath at temperature T_0. Random forces are applied directly to the centroid of each spinner. $R(t)$ are normalized zero-mean white-noise Gaussian processes, which assure thermodynamic equilibrium in the

absence of the externally applied torques.

Langevin Dynamics simulations are performed on graphic processing units (GPUs) with our HOOMD-blue software package [91, 92] using up to 16,384 spinners (81,920 disks), half of which are driven to always spin clockwise, and the rest driven to spin counterclockwise. Each disk is treated as a point mass m located at the center, which means $M = 5m$ and $I = 64m\sigma^2$. The hard contact is modeled via a Weeks-Chandler-Andersen potential with parameter ε [128] shifted to the surface of the spinner such that its range is a small fraction of the particle diameter, thereby approximating "perfectly" hard shapes. In the low Reynolds number limit, the translational and rotational drag coefficients are related through the Stokes-Einstein and Stokes-Einstein-Debye relations. If we approximate the spinner as a disk of effective radius $\tilde{\sigma}$, the relations for disks give $\gamma_r = \frac{4}{3}\tilde{\sigma}^2\gamma_t = 100\sigma^2\gamma_t$. We choose σ and ε as the basic units of length and energy, respectively. The unit of time is $t_0 = \sqrt{m\sigma^2/\varepsilon}$. Thermal noise is specified by $T^* = kT_0/\varepsilon$. Throughout the paper, we report results only for $\tau^D/\varepsilon = 1$ and $\gamma_t/(t_0^{-1}m) = 1$ unless stated otherwise.

5.3 Non-equilibrium phase behavior of spinners

5.3.1 Uneven distribution of energy

Following the random initialization of particle positions and orientations, and equilibration with active rotation turned off, the time evolution of the active system is characterized by an approach towards steady state.

Energy input to rotational motion by the applied torque is transferred to the translational degrees of freedom through collisions and dissipated by drag forces and torques. In steady state, we observe that the energy balance $\kappa = E_{\text{trans}}/E_{\text{total}}$ between translational and total kinetic energy converges. While the non-driven 2D system has $\kappa = 2/3$ as dictated by the equipartition theorem, a value $\kappa < 2/3$ quantifies the non-equilibrium character of the system. We analyze the behavior of κ as a function of density ϕ and noise T^*. As shown

in Fig. 5.2, at low density the driven rotational motion dominates translational motion and $\kappa \to 0$. With increasing density, the number of collisions increases and κ approaches the equipartition value. Interestingly, we find a phase transition for densities in the range $0.25 < \phi_c < 0.48$.

For zero noise, the increase in κ is sharp, and possibly discontinuous, but becomes less sharp as the noise increases. Based on the observation of a rapidly increasing length scale in the pair distribution function $g_{\mathrm{AB}}(r)$ of opposite spinners, we identify this transition as the phase separation of the system into A-rich and B-rich domains. As shown in the inset of Fig. 5.2, increasing the noise from zero at fixed values of applied torque initially lowers the critical density ϕ_c, because particle collisions that facilitate the onset of phase separation are more frequent. If the system is too noisy, phase separation is hindered and the trend is

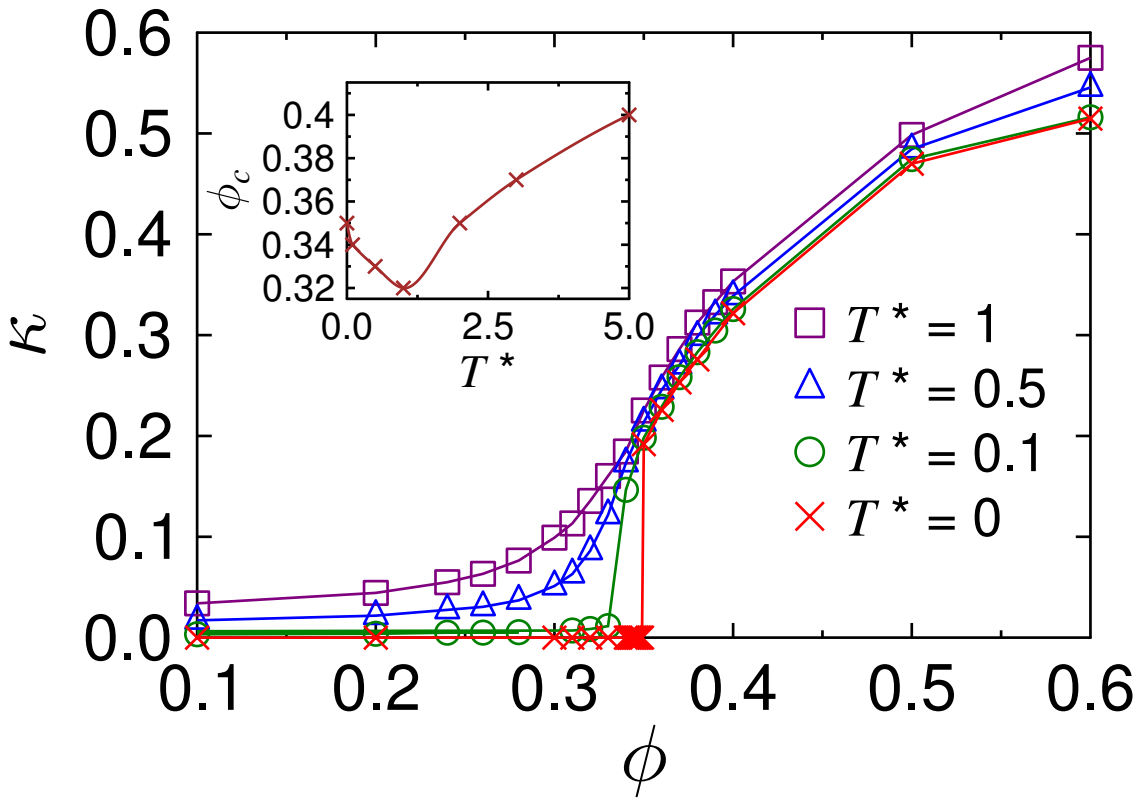

Figure 5.2 The ratio of translational to total kinetic energy κ indicates the presence of a phase transition ($\omega_0 = 1$). Error bars are smaller than the symbols. The inset shows the critical density ϕ_c as a function of noise T^*. The system consists of 16384 spinners driven by 50:50 ratio. From Ref. [23].

reversed: the system phase-separates at a higher density as the noise increases.

For the remainder of the chapter, we follow Refs. [129, 111, 127] and neglect the role of noise by setting $T^* = 0$. In this limit, the dynamics of the system is fully characterized by two parameters, the density ϕ and the low-density dimensionless steady-state angular velocity $\omega_0 = \tau^D t_0/\gamma_r$, which is a measure of activity. Fig. 5.1(b) shows the ϕ-ω_0 non-equilibrium phase diagram at (or near) steady state. Movies of the spinner dynamics can be found in the Appendix B.

5.3.2 Frozen state

At low densities, we find a frozen (absorbing [130] or dilute [127]) state, where the spinners are fixed in place and rotate at angular velocity ω_0. Translational motion does not couple to rotation, the system is non-ergodic, and drag forces dominate. The few collisions that occur from the initial kinetic energy die out quickly due to dissipation. The frozen states are reproducible for different initial conditions, including ones with high potential energy such as when the spinners are compressed into a central core of a high local density (0.7). Note that our frozen state is different from those observed under oscillatory shear [131] or with self-propulsion [132], where particles (translationally) retrace their trajectories.

5.3.3 Mixed and phase-separated fluids

At higher density, the frequency of collisions increases. When the time interval between collisions is sufficiently short, *i.e.* comparable to the characteristic time m/γ_t for energy dissipation, non-stop chained collisions can sustain the transfer from rotational to translational energy. Depending on ω_0, we observe a transition to either a mixed fluid or a phase separated fluid. While spinners with high activity, $\omega_0 \geq 1.2$, display two transitions (first to the mixed fluid, then phase separation), these transitions merge for lower ω_0. The spinners of a mixed fluid can have similar κ to that of a separated fluid but without exhibiting any

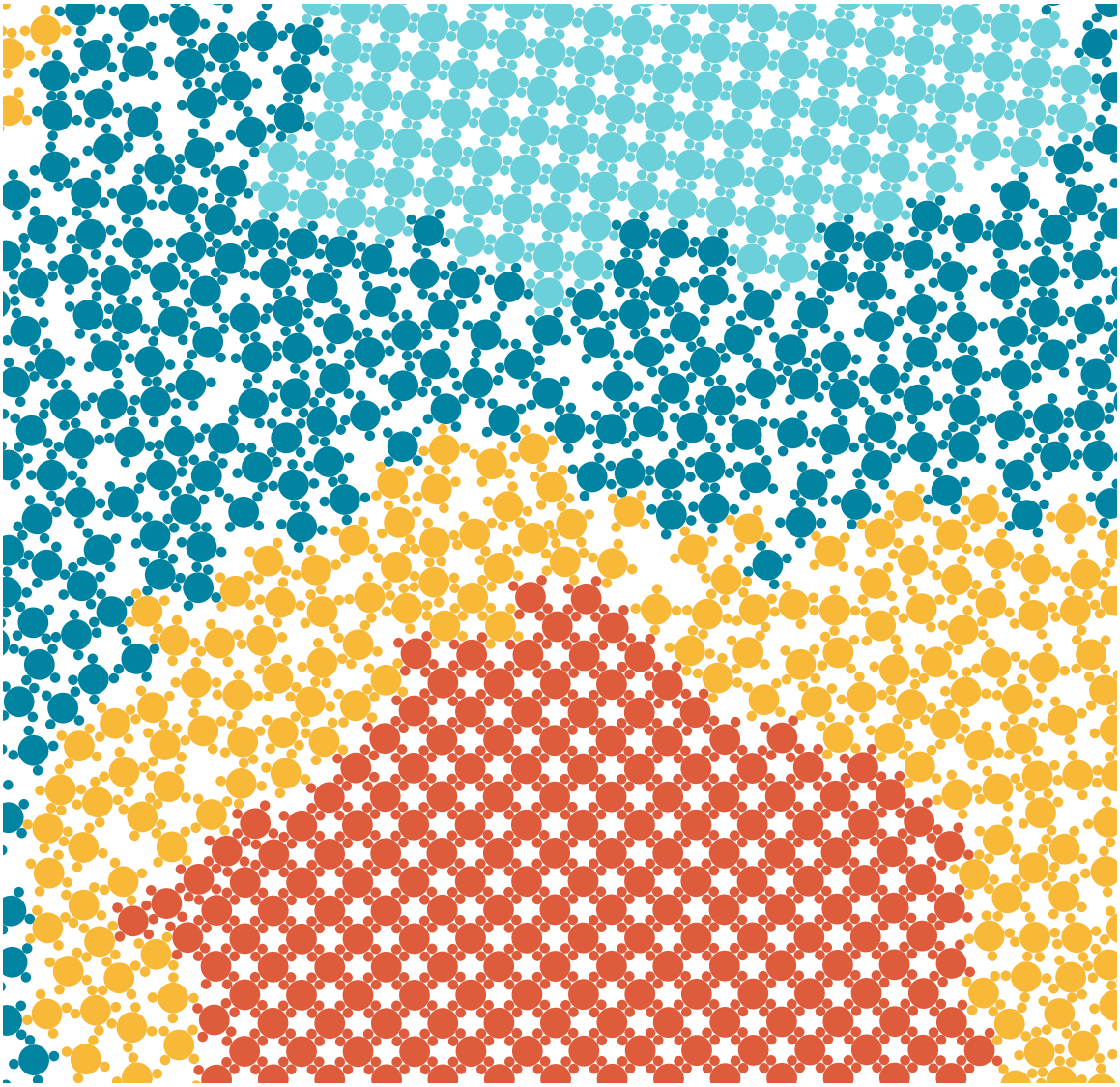

Figure 5.3 Fractions of rotating crystal domains co-existing with fluid. The crystal (fluid) are colored red (orange) for B spinners and light (dark) blue for A spinners. The crystal spinners arrange in square lattices. From Ref. [23].

ordered pattern or collective motion. In contrast, spinners in a phase-separated fluid de-mix and move collectively as discussed in details in Chapter 5.4.

5.3.4 Rotating crystals

As the density increases further, the spinners organize into crystals that rotate collectively about their centers of mass;particles no longer rotate about their individual centers. The

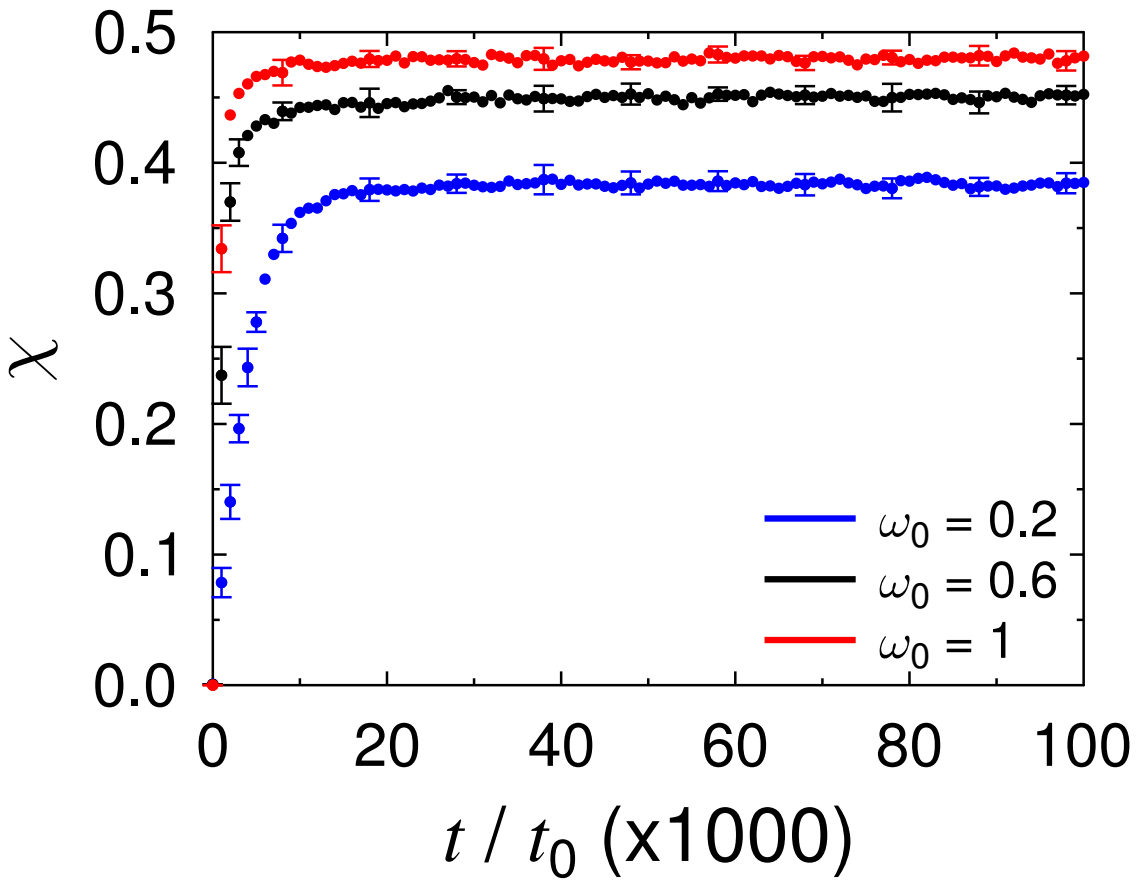

Figure 5.4 Crystal fraction $\chi(t)$ for a system of 16384 A spinners at density $\phi = 0.6$ for three levels of activity. χ achieves a steady state value, demonstrating the coexistence of fluid and rotating crystals. The data points are averaged over 10 runs. From Ref. [23].

critical density decreases as the activity increases in agreement with [110, 63], but not with [15]. If crystallization occurs before phase separation is completed, the crystal size is limited by the phase separating domains. The angular velocity of a crystal decreases with radius, similar to rotors assembled from polymers by self-propelled bacteria [133]. Dynamically, this phase represents a new kind of active crystal, a *rotating crystal* distinct from the two previously reported types, traveling and resting crystals [134].

The crystal is detected and characterized by a simple order parameter that captures its square-lattice structure Fig. 5.3. The order parameter is the averaged cosine of the four times

of the angle of a gear with a neighbor and has the following form

$$X_o = \frac{1}{n}\sum_{j=1}^{n}\cos(4\theta_{ij}) \tag{5.3}$$

where θ_{ij} is the angle between the body vector, connecting between the central disk and the peripheral disk 1, of the spinner i and a neighbor j. n is the number of neighbors of spinner i. Neighbors of a spinner are within a distance of 8σ. The formula 5.3 can be expressed in term of θ as following

$$X_o = \frac{1}{n}\sum_{j=1}^{n}(1+8\cos^4(\theta_{ij})-8\cos^2(\theta_{ij})) \tag{5.4}$$

In order to characterize the crystal growth, we define a parameter, χ, that measures the fraction of spinners in crystals in the total number of spinners. Plot of χ over time for a system of a single component,e.g. A, shows that the crystal grows rapidly to a fluid-crystal co-existing steady state Fig. 5.4. At steady state, the crystal exists in many rotating domains of different sizes, which are never observed to merge into one single domain after $10^5 t_o$. Interestingly, crystal growth rates and steady-state crystal fractions depend on the magnitude of the driving torque: the larger the torque, the faster and larger crystals grow. Practical applications of the rotating crystal are largely imaginative at this point but one could potentially utilize crystals rotating at controllable speeds to scatter lights at different frequency to create interesting photonic properties.

5.4 Effective interaction between spinners.

5.4.1 Spinodal decomposition

We measure the time evolution of the characteristic domain size. Domains coarsen over time with $t^{1/3}$ as shown in Fig. 5.5 by determining the first zero of $g_{\mathrm{AB}}(r)$ (Appendix B). The peak height of the structure factor scales as $t^{2/3}$(Appendix B). Together, these behaviors are

typical for spinodal decomposition of a binary mixture in two dimensions in the absence of hydrodynamics [135, 136, 137, 138]. The domain size growth exponent is similar to that measured in a biological system of self-organizing mussels [139], but different from that found in other systems of self-propelled colloids [63, 114]. The fact that a system of driven particles interacting solely via excluded volume follows spinodal decomposition is interesting and raises a question about the origin of the phenomenon, which is investigated in details in the following sub-sections

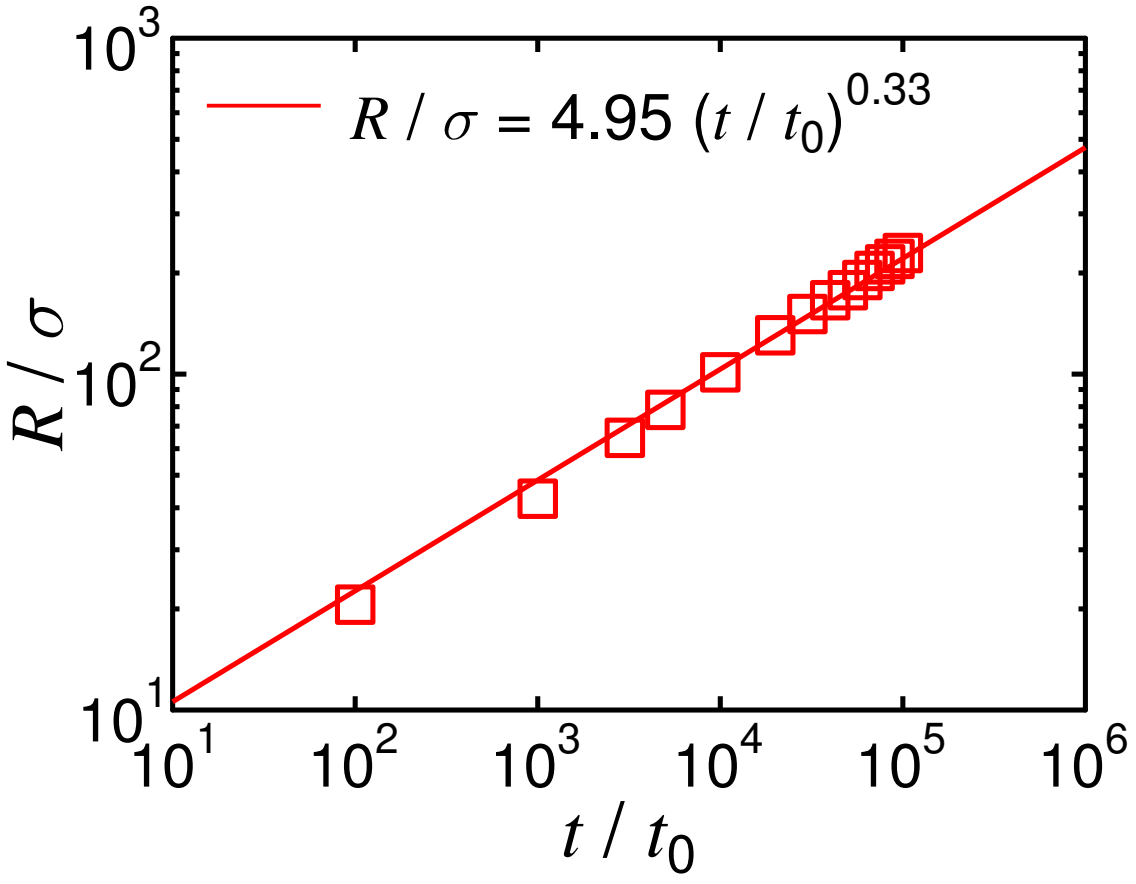

Figure 5.5 Domain size growth for a 50:50 mixture of 16384 spinners at $\phi = 0.5$ and $\omega_0 = 1$ during phase separation ($\phi = 0.5$). Each data point is averaged over 10 runs and has a standard deviation smaller than the markers. From Ref. [23].

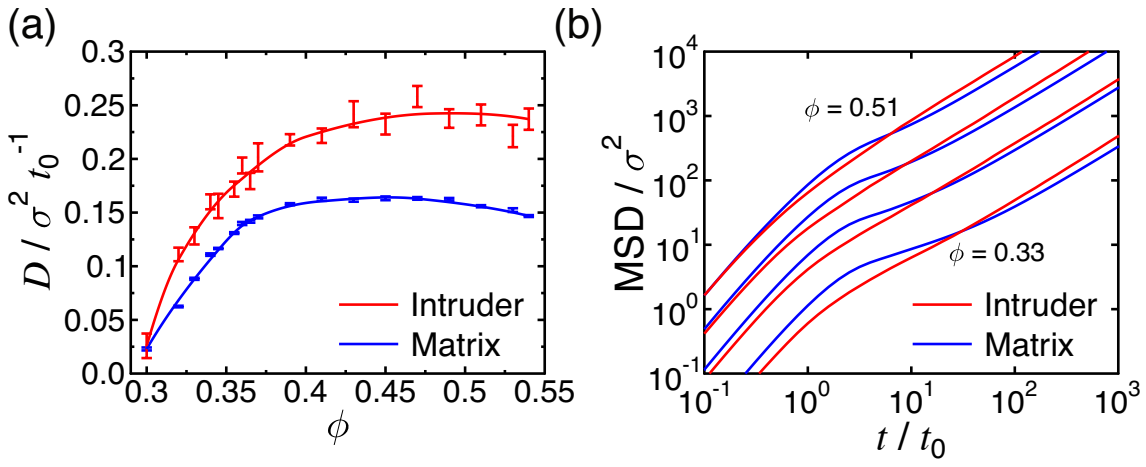

Figure 5.6 Comparison of (a) translational diffusion coefcient D and (b) mean-squared displacements for an (B) intruder in a matrix of 100 opposite (A) spinners. The spinners are driven by $\omega_0 = 1$. Curves in (b) at different densities are offset for clarity. Each data point in (a) is averaged over 10 runs. From Ref. [23].

5.4.2 Density-dependent motility

The origin of the phase separation is investigated with a system of one *B* spinner (the intruder) in a dense matrix of *A* spinners. We compare their mean-squared displacements $\text{MSD} = \langle |\vec{x}_i(t) - \vec{x}_i(0)|^2 \rangle$ in Fig. 5.6. While matrix particles have higher translational kinetic energy as seen in the ballistic regime $t < t_0$, the curves cross and diffusion of the intruder is faster for $t \gg t_0$.

The MSD of the matrix has a plateau indicative of caging. We extract the translational diffusion coefficient D and plot it as a function of density in Fig. 5.6(a). With increasing density, diffusion speeds up and the gap between intruder and matrix spinners widens. This differs from a common finding for self-propelled particles that the diffusion coefficient of particles in the dense phase of the phase-separated states decreases to zero as the density increases [15, 113, 114]. Thus, the theory developed for self-propelled particles such as in [112, 113, 114] may not be applicable to actively rotated particles and highlights the need for a more comprehensive theory.

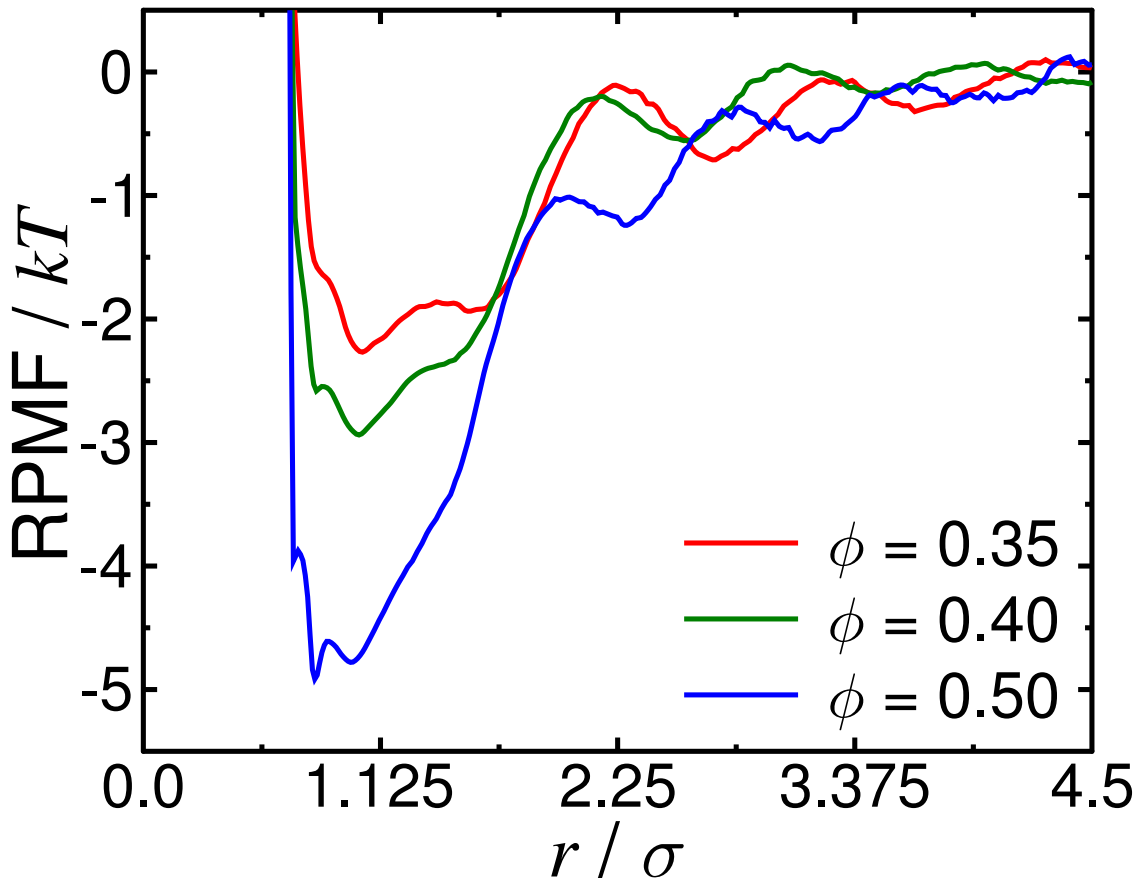

Figure 5.7 Effective demixing potential obtained for $N_A = 100$ and $N_B = 2$ at $\omega_0 = 1$ and different densities. The data is sampled every 100 time steps over 100 million time steps after the system reaches a steady state. From Ref. [23].

5.4.3 Effective Demixing Potential

We investigate the effective interaction between N_B intruders among N_A matrix spinners by mapping our non-equilibrium system to an equilibrium system of isotropic particles interacting with pair potentials. The mapping is achieved via the effective demixing (ED) potential, which describes the preference for demixing [22]. The ED potential quantifies the difference in kinetic behavior between like spinners and unlike spinners in the limit of a vanishing density of intruders, $n_B = N_B/(N_A + N_B)$. It is defined as

$$U_{\mathrm{ED}}(r) = -kT \lim_{n_B \to 0} \log\left(\frac{g_{\mathrm{BB}}(r)}{g_{\mathrm{BA}}(r)}\right). \tag{5.5}$$

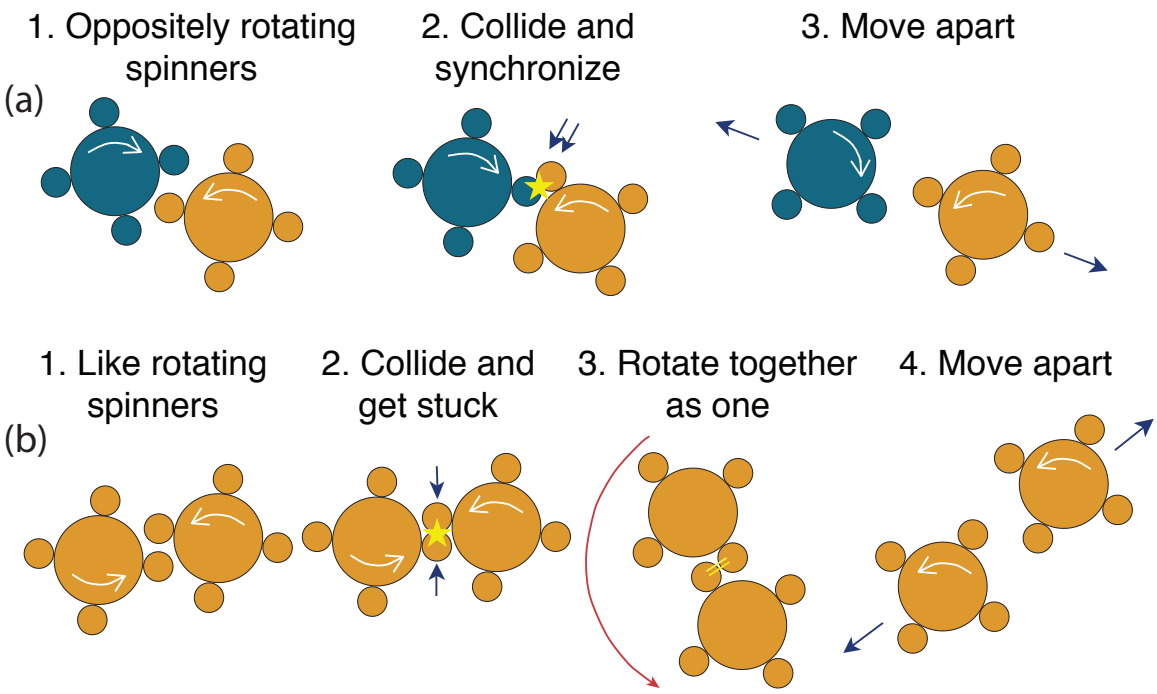

Figure 5.8 Typical interaction of two opposite spinners (a) and two like spinners (b). Like spinners tend to "stick" longer during a collision than opposite spinners, leading to an effective attraction between them.

Here, g_{BB} and g_{BA} are type-specific radial distribution functions. The definition guarantees that in the absence of external torque, $U_{\mathrm{ED}}(r) = 0$. In the presence of external torque we find an attractive well in $U_{\mathrm{ED}}(r)$ of several kT [1] that deepens with increasing density, Fig. **??**(d). At the critical density $\phi_c = 0.35$, the well depth is about $2kT$. We note that this value of interaction strength is comparable to the critical attraction strength for the vapor-liquid transition of 2D Lennard-Jones liquids [140] and to the critical reduced interaction in the 2D Ising model, $2.269kT$ [141].

The microscopic origin of the effective interaction can be understood by comparing pairs of neighboring spinners. Consider the interaction of two opposite spinners, Fig. 5.8(a). The "teeth" of the gear-like spinners move together for part of the cycle, synchronizing their rotation when in contact due to steric restriction, and then move apart. Now consider the interaction between two spinners rotating in the same direction, Fig. 5.8(b). Since the

[1] The temperature T appearing in the ED potential is not related to the noise T^*.

tangential velocities at contact are in opposite directions, the spinners momentarily "stick" sterically. They cannot spin about their individual axes and instead transfer their angular momentum momentarily to the pair and rotate together for part of the cycle before moving apart. The consequence is a longer contact time for like spinners compared to opposite spinners, breaking the symmetry between otherwise identical particles and resulting in an emergent, effective attraction (repulsion) between like (unlike) neighboring spinners.

5.5 Collective dynamics at interfaces and transport

5.5.1 Heterogeneous dynamics

As spinners phase separate, they form interfaces separating regions of opposite rotation. The short-time diffusion $\Delta\vec{x}(t) = \vec{x}(t) - \vec{x}(0)$ is visualized for a density where phase separation, Fig. 5.9, and also crystallization, Fig. 5.10, occur. We observe that the translational dynamics of the spinners is heterogeneous and cooperative, in particular at the interfaces. While diffusion is Brownian in the bulk, spinners move linearly along the interface in a super-diffusive manner with MSD $\propto t^2$.

As phase separation progresses, the total length of the interfaces decreases, reducing the number of super-diffusive spinners. Interestingly, we find that both the translational and rotational kinetic energies are uniform across the demixed fluid (Appendix B). This means spinners at interfaces do not move faster, but instead move farther in a given time window. Such dynamical behavior is reminiscent of the string-like dynamical heterogeneity in supercooled liquids and dense colloids [142, 143].

5.5.2 Interfacial transport

To investigate the possibility of extracting useful work from the active motion of the spinners, we add inactive test particles to the system. An inactive particle has the same shape, size,

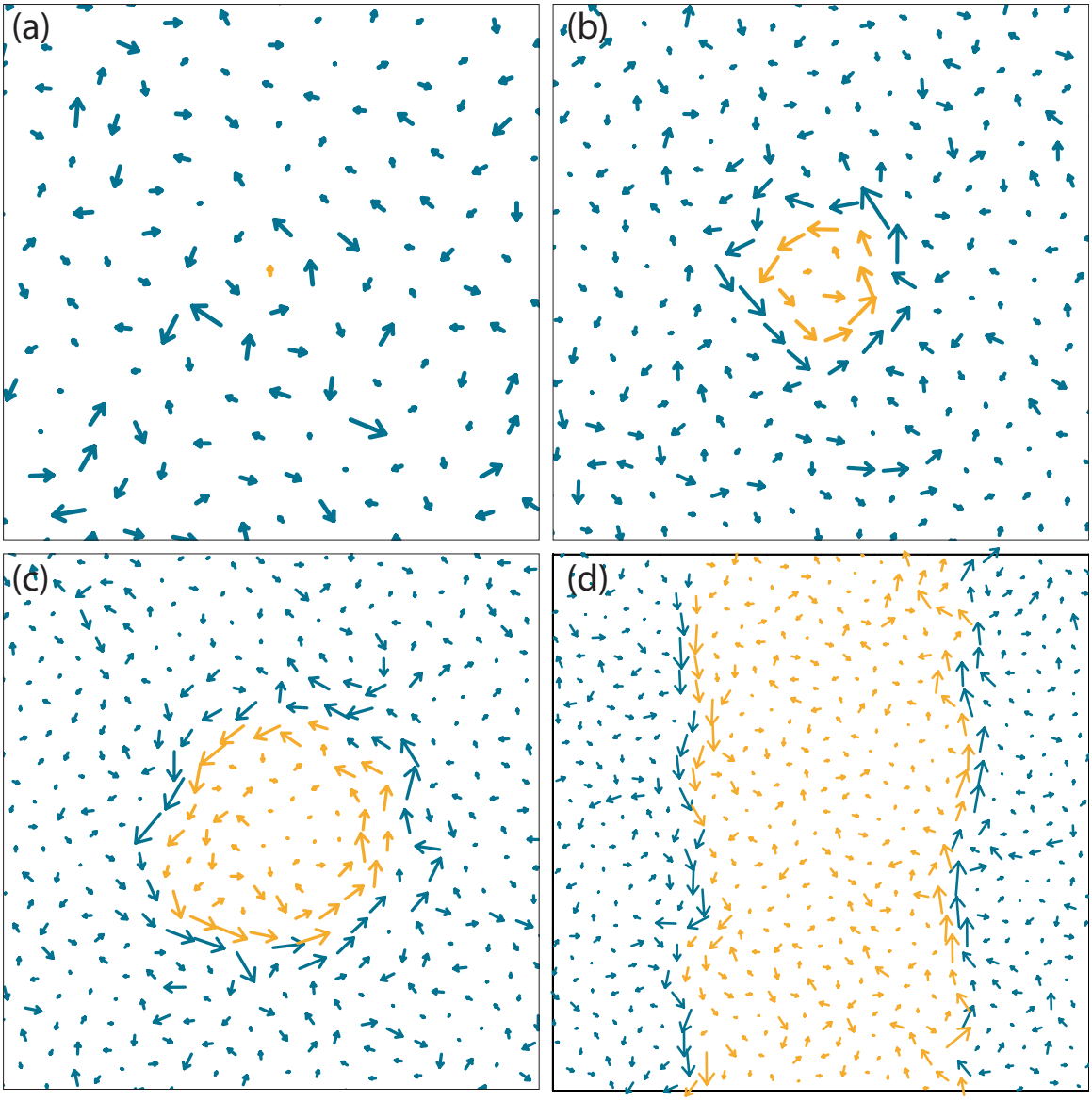

Figure 5.9 (a)-(d) Vector plots show the short-time diffusion $\Delta\vec{x}(t)$ in systems of $N = 576$ spinners with different numbers of intruders: (a) one, (b) 2%, (c) 10% and (d) 50%. The snapshots (a)-(c) are zoomed in. We use $\omega_0 = 1$ and densities of 0.5. The observation time windows are $10t_0$.